DESIGN, MODELING AND PERFORMANCE OPTIMIZATION OF A NOVEL ROTARY PIEZOELECTRIC MOTOR

Khanh A. Duong
Ephrahim Garcia

December, 1997 NAG-1-1484

(Under the sponsorship of NASA Langley Research Center)
Adaptive Structures and Devices for Space Applications

Final Technical Report 12/1/92 - 2/29/9
Vanderbilt University
512 Kirkland
Nashville, TN 37240

This final report is based on the unaltered thesis of Khanh A. Duong submitted to the Department of Mechanical Engineering in partial fulfillment of the requirements for the degree of Doctor of Philosophy at Vanderbilt University. This contract supports chapter one through chapter five.

TABLE OF CONTENTS

LIST OF FIGURES

LIST OF TABLES

CHAPTER I

INTRODUCTION

Piezoelectric motors have become more popular nowadays due to their many advantages. Piezoelectric motors have high resolution and high force capability. Apart from direct electro-mechanical conversion, piezoelectric motors provide mechanical reduction without using any reduction gear. Additional advantages of piezoelectric motors are the a very low noise emission and the absence of magnetic field. They can be found in many commercial applications such as photocopiers, autofocus lenses, and high resolution ink-jet printers. There are many types of piezoelectric motors developed up to date. Each of these types have its own unique application with advantages and disadvantages. These motors utilize the piezoelectric effect of piezoceramic to provide displacement for their operation. The properties of piezoelectrics can be found in various books written about piezoelectricity [1]. The principle and construction of each of these types will be discussed in the next chapter.

Although many piezoelectric motor have been built and refined, the ultrasonic motors are the most researched type. The quasi-static inchworm types are less researched but they have many important application such as micro/macro positioning both in the longitudinal and rotary directions [2-4]. The rotary inchworm motors receive even less attention in the research community. This fact is owed largely to the piezoelectric phenomenon. Since piezoceramic produces strain under the influence of an electrical field, most linear inchworm motors utilize this linear expansion by the principal piezoelectric effect to provide motion for their motors. It is more difficult to apply the linear motion provided by piezoceramic to achieve a rotary motion. There are attempts to obliquely polarize piezoceramic to achieve rotary motion from piezoceramic for use in rotary inchworm motors. However, the force provides by this d_{15} piezoelectric effect are small

compared to the commonly use principal strain d_{33} because piezoceramic are weak in shear. Rotary inchworm motors are equally important in applications required accurate aiming beside positioning. There is a need to study and design a better rotary inchworm motor.

The research in this thesis concentrates on studying and understanding the working principle of the rotary inchworm motor. From this knowledge, new way to operate the motor can be devised and implemented to improve the performance of the motor. A novel rotary piezoelectric inchworm motor was designed and built for this purpose. The motor studied here utilizes the principal piezolectric effect d_{33} of piezo stacks to provide motion for the components. Special flexure devices are used to convert linear motion to rotary motion. Flexures are used throughout the motor design to provide amplification of the displacement of piezoelectric stacks. The use of d_{33} piezoelectric effect provides the motor with larger displacement/speed and force output. The motor design has proved that a rotary inchworm motor can successfully be built using piezoelectric stacks. The motor as an inchworm type can provide large torque and speed. This motor can also be use as a clutch/brake mechanism. The prototype motor served as a test bed for studying the behavior of the inchworm motor in general and also allowed the implementation of new ideas to improve its performance. A comprehensive study of the motor was carried out to understand the working principle of the motor along with its strategies and pitfalls for future design purpose. Based on careful study of the motor's behavior, an optimum, non traditional driving method was derived and successfully improved the performance of the motor. This method can be applied to any inchworm motors in general to improve their performance without any adjustment to the hardware themselves.

This thesis consists of several chapters. An introduction to piezoelectric motors is presented to provide broad understanding about different types of piezoelectric motor available in the literature today. The detail designs of these motors and their principles of operation is provided and explained. The characteristic and behavior of the prototype motor is presented and discussed. Simulation of the prototype motor using MATLAB

SIMULINK is also included. The optimization of the performance of the using waveform optimization is presented. Verification experiment to compare the performance of the motor with traditional driving method and the optimum method found in this dissertation is provided. Conclusions and special insights to critical issues of the motor operation are discussed and future works are proposed.

CHAPTER I

INTRODUCTION

Piezoelectric motors have become more popular nowadays due to their many advantages. Piezoelectric motors have high resolution and high force capability. Apart from direct electro-mechanical conversion, piezoelectric motors provide mechanical reduction without using any reduction gear. Additional advantages of piezoelectric motors are the a very low noise emission and the absence of magnetic field. They can be found in many commercial applications such as photocopiers, autofocus lenses, and high resolution ink-jet printers. There are many types of piezoelectric motors developed up to date. Each of these types have its own unique application with advantages and disadvantages. These motors utilize the piezoelectric effect of piezoceramic to provide displacement for their operation. The properties of piezoelectrics can be found in various books written about piezoelectricity [1]. The principle and construction of each of these types will be discussed in the next chapter.

Although many piezoelectric motor have been built and refined, the ultrasonic motors are the most researched type. The quasi-static inchworm types are less researched but they have many important application such as micro/macro positioning both in the longitudinal and rotary directions [2-4]. The rotary inchworm motors receive even less attention in the research community. This fact is owed largely to the piezoelectric phenomenon. Since piezoceramic produces strain under the influence of an electrical field, most linear inchworm motors utilize this linear expansion by the principal piezoelectric effect to provide motion for their motors. It is more difficult to apply the linear motion provided by piezoceramic to achieve a rotary motion. There are attempts to obliquely polarize piezoceramic to achieve rotary motion from piezoceramic for use in rotary inchworm motors. However, the force provides by this d_{15} piezoelectric effect are small

CHAPTER II

AN INTRODUCTION TO PIEZOELECTRIC MOTORS

Introduction to piezoelectric materials

The word "piezoelectricity", consists of *piezo* which derives from the Greek, meaning "to press" and *electric* which simply means electricity, is used to describe the coupling effect between electric and elastic phenomena. This piezoelectric phenomenon occurs when pressure is applied to a material it causes an electric field to build up in that material. Therefore, the word piezoelectric is used to describe this phenomenon. It was originally discovered by Pierre and Jacque Curie in 1880 [5]. They found that, in certain materials such as cane sugar, topaz and quartz, mechanical stress were accompanied by the production of electric surface charges. However, it is not pressure that generates the electric field. It is the mechanical strain of the material under pressure that produces the field. This ability of piezoelectric to produce an electric field under strain makes them an attractive material to use in strain or force sensors. Nowadays, piezoelectric materials can be widely found in load cells and accelerometers.

A year after the Curie bothers discovered the piezoelectric phenomenon, Lippmann predicted the converse effect from thermodynamic considerations. An imposed voltage produces mechanical deformation. This "converse" piezoelectric effect allows the material to also be used as an actuator. In fact, this "converse" effect is used in more applications than the "direct" piezoelectric effect and makes piezoelectric materials more popular.

Piezoelectric materials are sometimes also called piezoceramics because they are glass/ceramic material. The most common type of piezoceramic used is PZT (Lead Zirconium Titanate). The maximum mechanical strain of PZT is on the order of 0.1%. PZT has low tensile and shear strength. PZT actuators are commercially available as bender elements, single wafers, or stack actuators. Another popular type of piezoceramic

is electrostrictive material or PMN. The physical properties of PMN (Lead Magnesium Niobate) ceramic type is mostly similar to PZT. PMN differs than PZT in which it has a more nonlinear, second order strain response to the applied electric field. For PZT, the strain is almost proportional to the applied voltage or charge. Another characteristic of PMN is that it also produces positive strain when the applied field is reverse (negative). Figure 2.1 show the typical response of PZT and PMN materials.

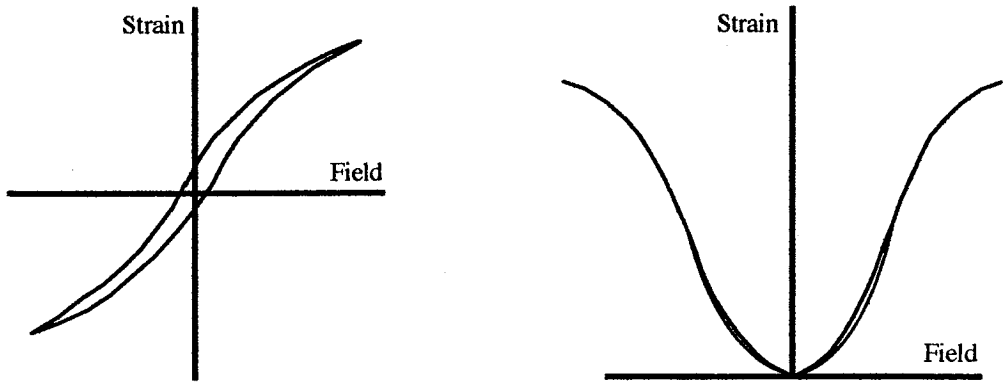

Typical response of PZT Typical response of PMN

Figure 2.1. Typical response of PZT and PMN materials.

The electromechanical coupling for PMN is slightly higher than that for PZT, typical strain is on the order of 0.15%. PMN also exhibits less hysteretic behavior than PZT. PMN is often use with a DC bias of the input voltage to move the operating point to the linear region of its response curve as shown in Figure 2.1.

To make the material piezoelectric, the material itself has to go through a polarizing procedure to expose it to a very strong electrical field. Piezoceramics can be consider as a mass of minute crystallites, each having its electric dipole. Under a strong electrical field, these dipoles become oriented in the direction of the field. When the field is removed, the dipoles become locked roughly in alignment thus giving the material a remanent polarization and a permanent deformation.

Introduction to solid state motor

Piezoelectric motors have been around for about 30 years. However, recent advances in active material technology which provides better electro-mechanical coupling materials have created a research and development surge in this field of piezoelectric applications. Numerous designs have been researched and developed. Many different kinds of motor with different shapes, sizes and potential applications were studied. Research effort have been spent to improve the efficiency, speed and force output of these motors.

Solid state motors can be defined as those rely on the direct coupling between electrical field and mechanical motion through mechanical strain. Therefore, piezoelectric motors can be considered solid state motor since they use piezoelectric material to convert electrical power to mechanical power. The majority of solid state motors depend on the force of friction to convert micro strain of piezoelectric actuators into final macro motion output. This method of achieving motion output is rather different than the method use in conventional electromagnetic motors.

Solid state motor has been proved to have numerous advantages over conventional electromagnetic motors. Solid state motors have large power density. They can provide a large holding force without power input. Solid state motors are relatively quiet and can reduce the output speed down to zero without using reduction gears. The output motion can be reduced down to zero by controlling the input frequency and voltage. Since solid state motors do not rely on electromagnetic coupling, they do not generate magnetic field which is very useful in application where magnetic field is undesirable. This advantage can be readily seen in the Scanning Tunneling Microscope sample holder where a magnetic field would interfere with the focusing electron beam. Piezoelectric motor can also be very efficient and have large power density because they operate by directly convert electrical power to mechanical power. The efficiency of energy conversion in piezoelectric materials

is typically greater than 90%. The only loss is cause by heating of the dielectric material. Kumada in 1985 reported of achieving 80% efficiency with his mode conversion ultrasonic motor [6]. His motor also achieve a power density of 80 W/kg which is much higher than the typical 30 W/kg in conventional electromagnetic motors. The force per active area of solid state motors is also greater than electromagnetic motors. Schöner (1992) has shown that the force per active area of piezoelectric motors is about 3.5-10 N/m^2 compared to the 0.1-0.15 N/m^2 range of electromagnetic motor [4]. Piezoelectric motor can also have a very fast response time due to the fast response of the piezoelectrics. Sugihara et al (1989) have shown the response time of a traveling wave ultrasonic motor can be less than 1 msec [7].

There are hundred of applications using piezoelectric motors and many potential application have not yet been investigated yet. Piezoelectric motors are mostly use for applications required high precision positioning capability. For example, piezoelectric motors are used for lithography in semi-conducting industry, microsurgery, scanning tunneling microscopes, scanning electron microscope, satellites [8]. Piezoelectric motors have also found their way into consumer product application such as printers, window winder, paper feeders, card sending devices, personal cassette players, and recently inkjet printer. Ultrasonic motor can be widely seen in autofocus video camera. Recently, Canon and Nikon also use ultrasonic motors in their autofocus lenses for still photography camera. The new type of autofocus lenses provide faster focusing speed, extremely silent and consume much less power from the battery compared to the regular focusing motor. Schaaf (1995) have written a report about important piezoelectric motor designs in the research community [9]. Piezoelectric motors are also commercially directly available. Burleigh Instruments markets their linear Inchworm motor for high precision positioning application. This motor is capable of delivering 2 mm/sec. speed over a range of 25 cm (Burleigh, 1986). Shinsei Ind. Co. Ltd. also has its ultrasonic motors commercially available. This motor can deliver 3.8 kg-cm of torque and speed of 100 rpm..

Piezomotor classification

A wide range of piezoelectric motors have been researched and developed up to date. These motors, vary in shapes and sizes, employ different methods of converting microstrain into macro motion. Attempts have been made to classify piezoelectric motors according to their method of energy conversion. Hagwood (Hagwood 1994) was one of the first to extensively categorize piezoelectric motors [10]. A comprehensive classification of solid state motor is shown in Figure 2.2.

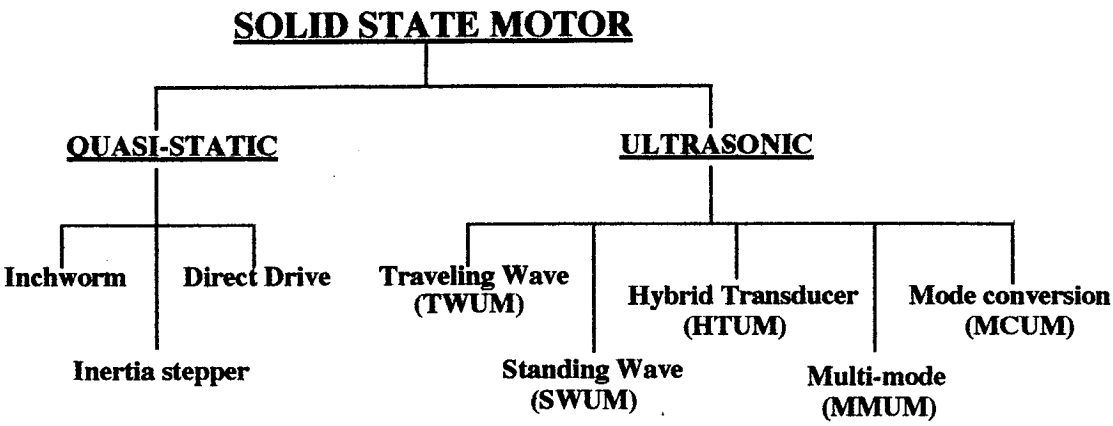

Figure 2.2. Classification of solid state motors.

From the figure, solid state motor can be divided into two classes by their operating frequency. Ultrasonic motors operate at high frequency usually above 20 kHz. Quasi-static motor operate at below resonance frequencies of the motor system usually at very low frequencies. The classification presents in this thesis will include the operational principle of each type of motor along with their illustrations. The state of the art of motors from different researchers and their performance will also be mentioned.

Ultrasonic Motors

The largest class of solid state motors are ultrasonic motors. They are defined as "devices that transform vibrations and wave motions of solid into progressive or rotational motions by means of contact frictional forces" [11]. Ultrasonic motors operate at very high frequency above the audible range of human ears and hence the name ultrasonic applied. This class of motors take advantage of mechanical resonance to increase the microscopic strain in order to achieve higher speeds and loads. The construction of these motor are very simple. The motor consist of a stator and a rotor. An elliptic motion is generated in the stator. This elliptic motion is generated ultrasonically by the mechanical strain of the piezoelectric materials. The rotor, which is pressed to the stator, only contacts the stator intermittently because of its time constant is much larger than that of the elliptical motion. During this contact interval, the rotor is driven by the tangential component of the elliptical motion. The normal component of the elliptic motion along with the preload control the magnitude of the friction force between the stator and the rotor. The operating principle of ultrasonic motors is shown in Figure 2.3.

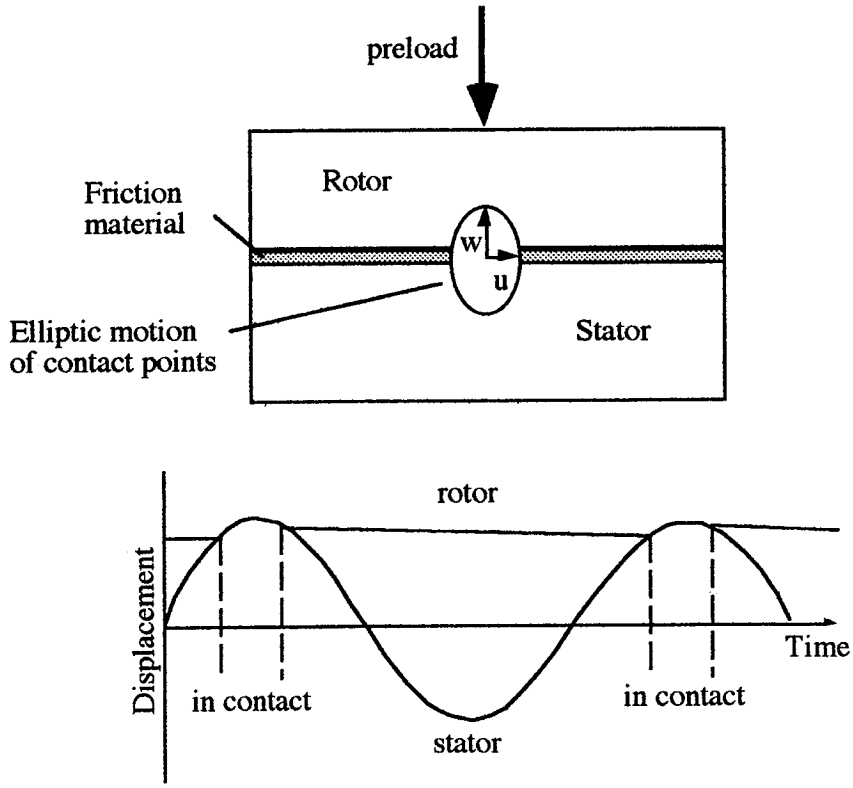

Figure 2.3. Operating principle of ultrasonic motors (Ueha, 1989) [12].

Since friction is involved in converting the tangential component of the elliptical motion into macroscopic motion, the contact material between the rotor and stator is very critical in the operation of the ultrasonic motors. A soft contact material will not break the contact during the cycle and a hard contact material will result in slippage during force transmission. Endo (1986) have shown that the velocity of an ultrasonic motor is proportional to the square root of the coefficient of friction [13]. The preload of the rotor onto the stator also dictates the performance of the motor and been studied by Endo. The operating frequencies of the ultrasonic motor is also limited by the response time of the piezoelectric actuators. Therefore, the decrease in size of the ultrasonic motor is limited by the increasing in resonance frequency [14].

The principles of how to generate the elliptical motion in the stator are different between types of ultrasonic motors. These motors can also be further classified according

to their principles of operation. Briot (Briot, 1993) divides ultrasonic motors into three categories: traveling wave, multi mode and mode conversion [15]. The most comprehensive classification of ultrasonic motors divides them into five different types. Schöner (1992), Ueha (1989, 1988), and Tomikawa (1987) have reported about the classification of ultrasonic motors in literature [4, 12, 16, 17]. Each of these types of ultrasonic motors will be examined and discussed.

Traveling Wave Ultrasonic Motors (TWUM)

The traveling wave motor is by far the most developed of the ultrasonic motors be cause of its simplicity. In this motor, a traveling wave is excited in an elastic stator by exciting two standing wave of the same vibrational mode with temporally 90 degrees and spatially 1/4 wave length out of phase. The combination of these two standing waves results in a traveling wave. This traveling wave generates the elliptic motion of every point in the elastic stator. The rotor, which is in contact with the stator, is driven by the transverse component of this elliptical motion. The operating principle of a traveling wave motor is shown in figure 2.4.

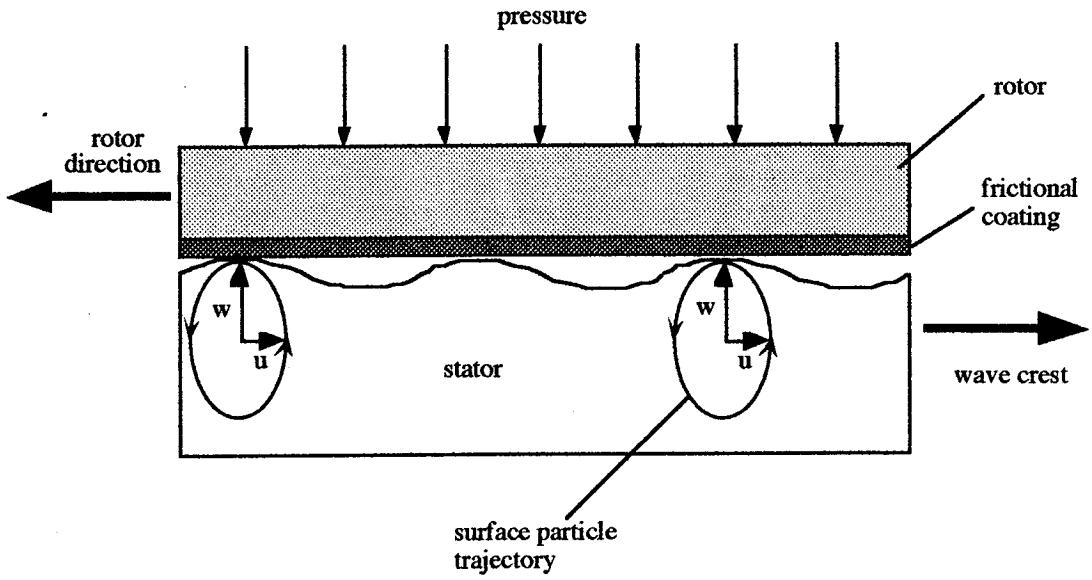

Figure 2.4. Traveling wave ultrasonic motor (TWUM).

Traveling wave motor can be configured to provide either rotary or linear motion output. For rotary type, the traveling wave is excited inside an elastic circular stators. For linear motor, a straight elastic stator is used. However, matched impedance waveguide must be used at either end of the stator to impose the traveling wave [17].

Tremendous efforts have been spent to research and develop the traveling wave ultrasonic motors. The performance of these motors up to date are very impressive. Takano (Takano, 1991) developed his traveling wave motor using two degenerate bending modes to excite a circular stator [18]. This motor can achieve a maximum speed of 15 rpm and torque of 400 grf-cm with an efficiency of 13%. Shinsei Ind. Co., Ltd. markets their TWUM commercially with impressive performance. This motor is rated at 3.8 kg-cm and 100 rpm. Kamano et al. (1988, 1989) extensively investigated the characteristics of this motor [19, 20]. Control schemes have been devised to improve the response, speed and precision of these motors. Hatsuzawa et al (1986) and Aoyagi et al, (1992) have subjected the motor response with different input parameters such as frequency, voltage and phase

[21, 22]. Their studies have shown that for ultrasonic motor, speed is most sensitive to the operating frequency. The speed can also be easily controlled by the phase shift between the two input waveforms, which is responsible for the transverse component of the elliptical motion. Kurosawa et al. (1989) has constructed a TWUM using the first bending mode of a small cylinder [23]. The bending mode is excited with two sinusoidal voltages 90 degrees out of phase temporally and spatially which forms a traveling wave of the end of the cylinder. This motor can attain speed of 300 rpm under no load condition and generate 1.5 kg-cm torque output.

The traveling wave motors are also extensively modeled by researchers using mathematical models and finite element tools. Mathematical equations for the excitation of traveling waves are devised. The frictional contact between the rotor and stator are also investigated using finite elements analysis. Mathematical and finite element models can be found in ref. [10, 24-30].

Standing Wave Ultrasonic Motors (SWUM)

As the name suggested, the standing wave ultrasonic motors operate by imposing a standing wave in the elastic stator. Figure 2.5 shows the operating principle of this type of motor. A standing wave is excited in the stator with nodes and anti-nodes as shown in Fig. 2.5a. By allowing the rotor to contact particular sections of the standing wave in the stator, motion can be achieved. Figure 2.5b shows the region in the standing wave that generate the motion in the shown direction. Motion in the either directions can be achieved by strategically placing contact ribs in the region that produce the desired motion in that direction as shown in Fig. 2.5c and 2.5d. This type of motor is therefore limited to operate in one direction.

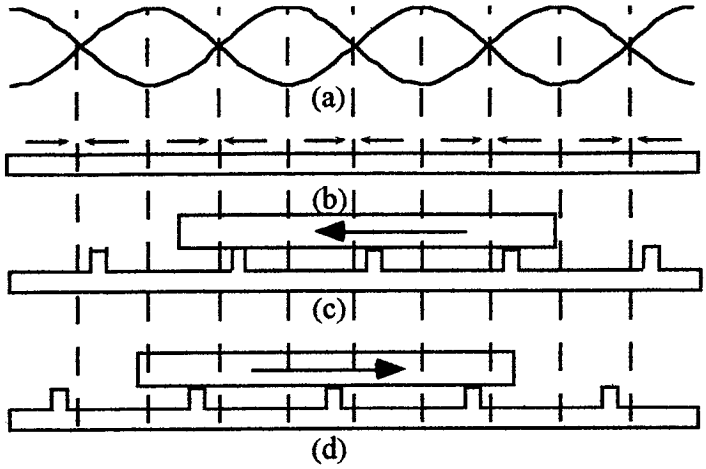

Figure 2.5. Operating principle of a standing wave ultrasonic motor (SWUM) (Iijima, 1987) [31].

Iijima et al. (1987) have developed a standing wave motor using flexural vibrations of a ring with 50 mm OD and 5 mm thick [31]. Maximum torque of 2 kg-cm and speed of 80 rpm were obtained with this prototype motor. The standing wave motor are simple to construct and operate. However, there are very examples of this type of motor due to the limited performance and one direction of output motion.

Hybrid Transducer Ultrasonic Motors (HTUM)

The hybrid transducer motors operate by breaking down the elliptical motion into two separate orthogonal components. The component in parallel with the direction of motion, U, provides the output and the component perpendicular to the direction of motion, W, provides the clamping force. The hybrid transducer type motors can be configured to provide either linear or rotary outputs. The schematic the linear type motor is shown in Figure 2.6. The rotary motor type is shown in Figure 2.7. They can be configured to provide either linear or rotary output motion. The construction of the hybrid transducer

type is some what similar to the construction of the inchworm motor. However, they are operated at much higher frequencies.

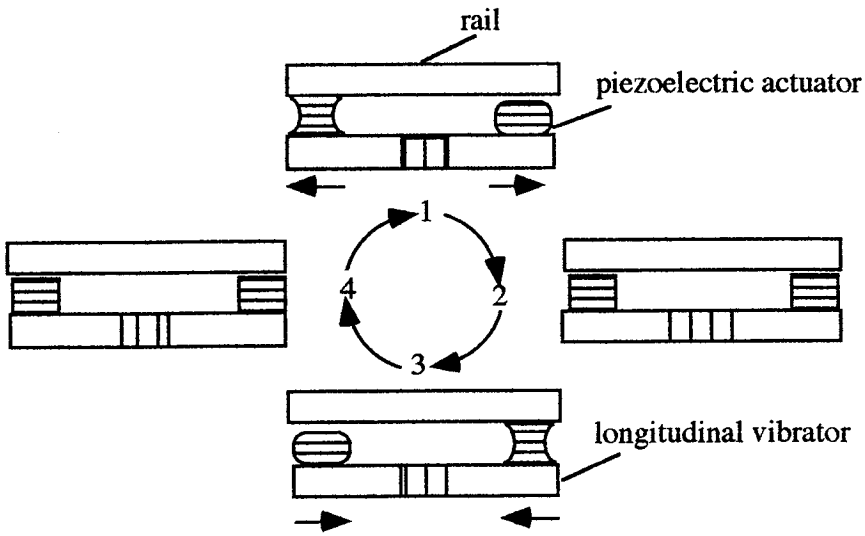

Figure 2.6. Linear Hybrid Transducer Ultrasonic Motor (Kurosawa, 1989)

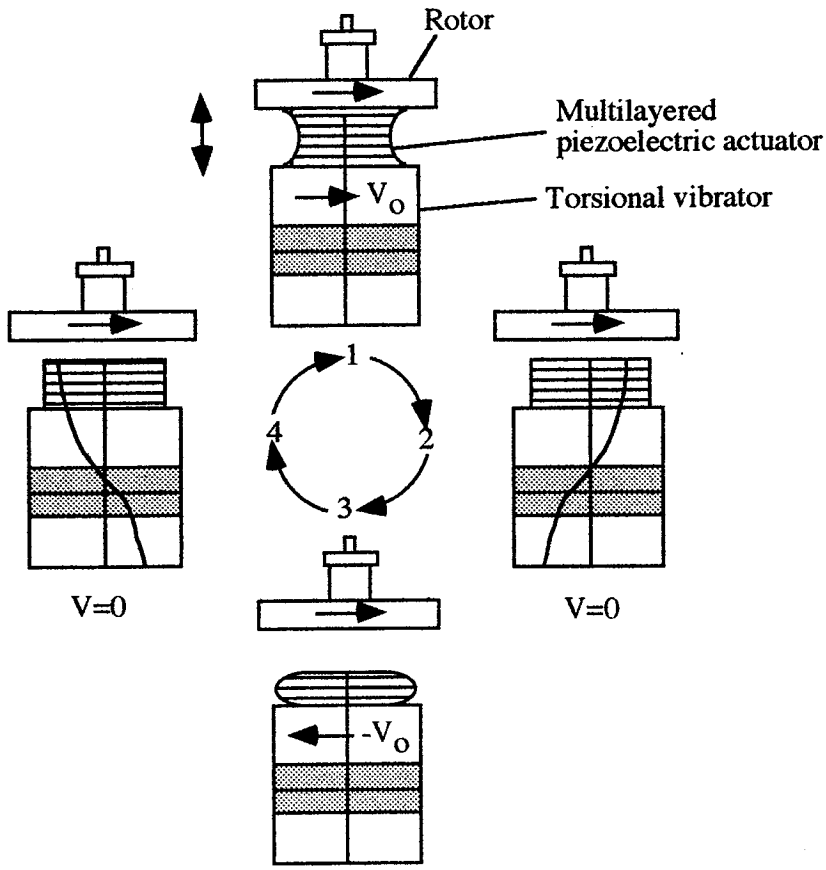

Figure 2.7. Rotary hybrid transducer ultrasonic motor (Nakamura et al., 1989).

By breaking down the actuating motion into two separate components, the hybrid transducer type allows flexibility in motor design. The hybrid transducer motors are usually operated at the resonance frequency of the parallel component to maximize the output motion. The orthogonal components (clamping) are then operated at the same frequency of the parallel components. However, this operating frequency can also be the resonance frequency of the orthogonal component by design. The phase relation between these two components are usually 90 degrees to generate the desired elliptic motion. The hybrid transducer motors can be used for both micro and macro positioning. However, very low speed macroscopic motion can not be achieve by reducing the operating frequency since they usually operate at the resonance frequency of the parallel component. Low

speed can be achieved by varying the phase between the two orthogonal components, thus changing the magnitude of the parallel component.

The hybrid transducer motors have been developed by many researchers. Kurosawa (Kurosawa, 1988) originally developed the hybrid transducer motor which was shown in Fig. 2.6 [32]. His motor was able to attain the speed of 50 cm/s and 500 g of force output. The motor efficiency is high at 36%. The clamping actuator was later modified as flexural vibrators instead of longitudinal vibrator in a later version of the motor [33]. Kurosawa also built a rotary motor based on the same principle [34]. This motor operates at the resonance frequency of the torsional actuator. The motor had a maximum speed of 100 rpm, output torque of 7 kg-cm, and efficiency of 33%. Ohnishi (1989) developed a rotary motor which has the two orthogonal actuator both operate at resonance frequency [35]. This motor has a maximum speed of 100 rpm with a dynamic torque output of 3 kg-cm. An efficiency of 40% was also record with this motor. Uchino (1988) built his linear motor in a fashion similar to the inchworm motor [36]. This motor consists of a longitudinal actuator with two legs attached at both ends. The bending motion of the two legs, which is the results of the excitation of the linear actuator, forms the elliptical motion at the end of the two legs. The motor has a maximum force of 100 gf, maximum speed of 30 cm/s and an efficiency of 10%. The design issues involving the construction of the hybrid transducer motors were studied and reported by Nakamura et al. (1991,1993) [37, 38]. Mori et al. (1989) use a linear hybrid transducer motor for his precision X-Y stage [39]. This motor is capable of achieving maximum speed of 10 cm/sec with ability to micro position over a range of 3 μm and resolution of 16 nm.

Multi-Mode Ultrasonic Motors (MMUM)

The multi-mode ultrasonic motors are the most widely researched currently. This type of motors form the elliptical motion by simultaneously imposing two vibrational modes in the stator as illustrated in Figure 2.8. From the figure, the vibration of the two

modes forms the elliptical motion at the end of the stator. A rotor is pressed to the end of the stator. The rotor is driven by the tangential component of the elliptical motion. The direction the multi-mode can be changed by reversing the relative phase of the two driving signals.

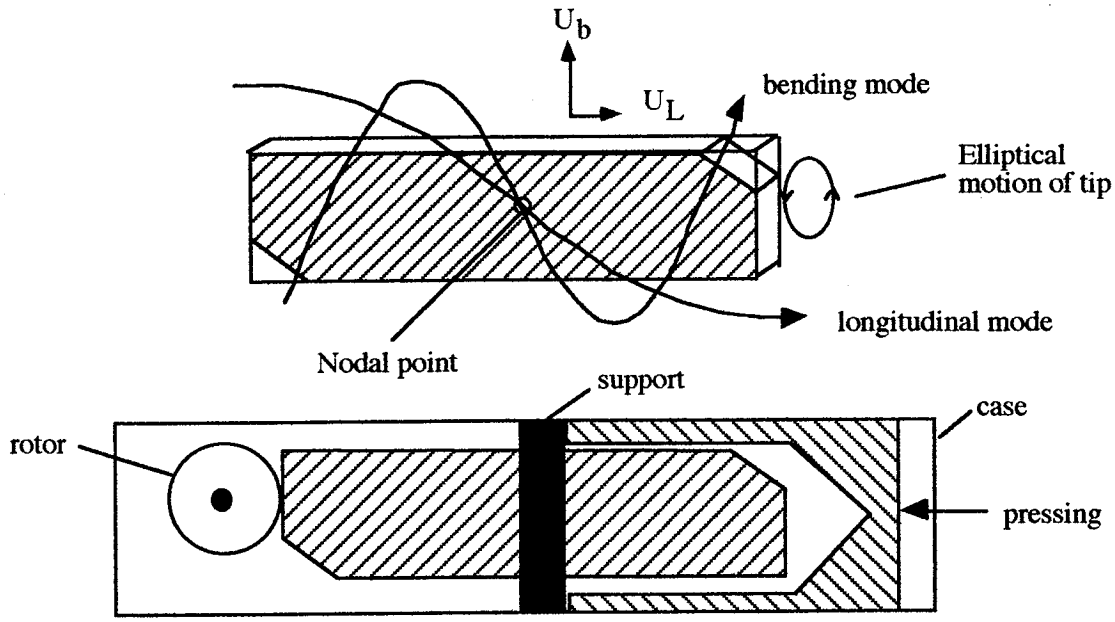

Figure 2.8. Multi-mode ultrasonic motor (Aoyagi, 1993) [40].

Fleischer (1989, 1990, 1989) constructed his multi-mode motor by exciting the longitudinal and bending modes in a bar [41-43]. The frequency ratio of the longitudinal and bending in this motor is 1:2 to avoid coupling between the two modes. The motor achieved a speed of 150 rpm. The maximum torque is 0.3 kg-cm and efficiency is 5%. Snitka (1993) developed a multi-mode motor using the longitudinal mode for the driving force and the flexural mode for the clamping force [44]. This motor achieved a speed of 120 mm/s with resolution of 0.01 μm. Aoyagi (1992) built a multi-mode motor with the two vibration modes coupled together [22]. By coupling the two modes, a single actuator can be used for excitation. The motor has an efficiency of 12.6 % with maximum torque of

30 gf-cm and speed of 10.5 rps. Takano (1988) built his motor using the first longitudinal and 4th bending modes of a thin rectangular plate [45]. The motor has a maximum speed of 17 cm/s and efficiency of 20%. Kosawada (1992) developed a motor for card sending device using the first longitudinal and eighth bending modes [46]. The speed of this motor is reported at 70 cm/s with a low efficiency of 3.5%. Ohnishi (1989) fabricated a rotary motor using the longitudinal and torsional modes [35]. The frequencies of the two modes are matched by changing the preload between the stator and the rotor. The torsional actuator is an obliquely poled piezoceramic disk. The maximum torque output is 4 kgf-cm and speed is 450 rpm. The rotational direction can be changed by reversing the phase between the two driving signals. Iwao (1990) also constructed a rotary ultrasonic motor using bending and shear modes of a disk resonator [47]. The maximum speed of 18 rpm was attained with the torque output of 1.6 kg-cm and efficiency of 2%. Umeda (1989) created his multi-mode motor using torsional and longitudinal modes [14]. Maximum speed of 93 rpm, torque of 1 kgf-cm and efficiency of 4.3% were achieved. A new version of his motor employed a piezoelectric ring for clamping force. This motor has a rotational speed of 74 rpm and torque of 1 kgf-cm. However, the efficiency of this motor increases tremendously to 24.5%. Iijima et al. (1992) also built a rotary multi-mode motor using longitudinal and flexural vibrations of a flat plate [48]. This motor is capable achieving speed of up to 1500 rpm with no load. The maximum torque output is to 0.1 kg-cm. Mori (1989) developed a linear motor using the longitudinal-longitudinal modes [39]. The motor consists of to piezoelectric actuator orthogonally attached to a block. The elliptical motion of the block is caused by driving the two actuator with 90 degrees out of phase signal. A slider is pressed to the block to obtain output motion. The motor has a maximum linear speed of 100 mm/s while achieving a resolution of 0.016 μm. Tomikawa (1986,1987,1988,1989,1991,1992,1992) has researched extensively into multi-mode motors [3, 16, 49-53]. He has reported his studies on the construction and characteristic of

longitudinal and torsional motors. One of his rotary motor is capable of achieving speed of 350 rpm with 10% efficiency.

Mode Conversion Ultrasonic Motors (MCUM)

The mode conversion motors use one piezoelectric actuator to produce both components of the elliptic motion. Usually, the longitudinal component is generated directly by the piezoelectric actuator. The transverse component is then generated by using mode conversion. The mode conversion motors are usually operated in one direction by cause only a single actuator is used to generate the motion. Figure 2.9 shows a "wood pecker" type mode conversion motor developed by MicroPulse System (1986) [54]. In this motor, the transverse component of the elliptic motion is generated at the tip of the stator by its bending mode. This motor can operate at 150 rpm and produce a torque output of 4.5 g-cm.

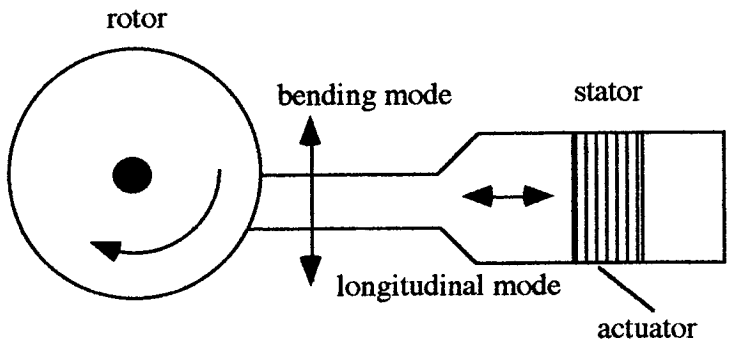

Figure 2.9. Woodpecker type MCUM.

Figure 2.10 also show a different configuration of a rotary mode conversion motor by Kumada (1985) [6]. In this motor, the longitudinal vibration is converted into torsional vibration by the torsional coupler. Kumada's motor can achieved a speed of 90 rpm. The torque output of this motor is 13 kg-cm. His motor is also the most efficient solid state

motor reported up to date. This motor is able to achieve efficiency of 80%. The power density of this motor is also high at 80W/kg

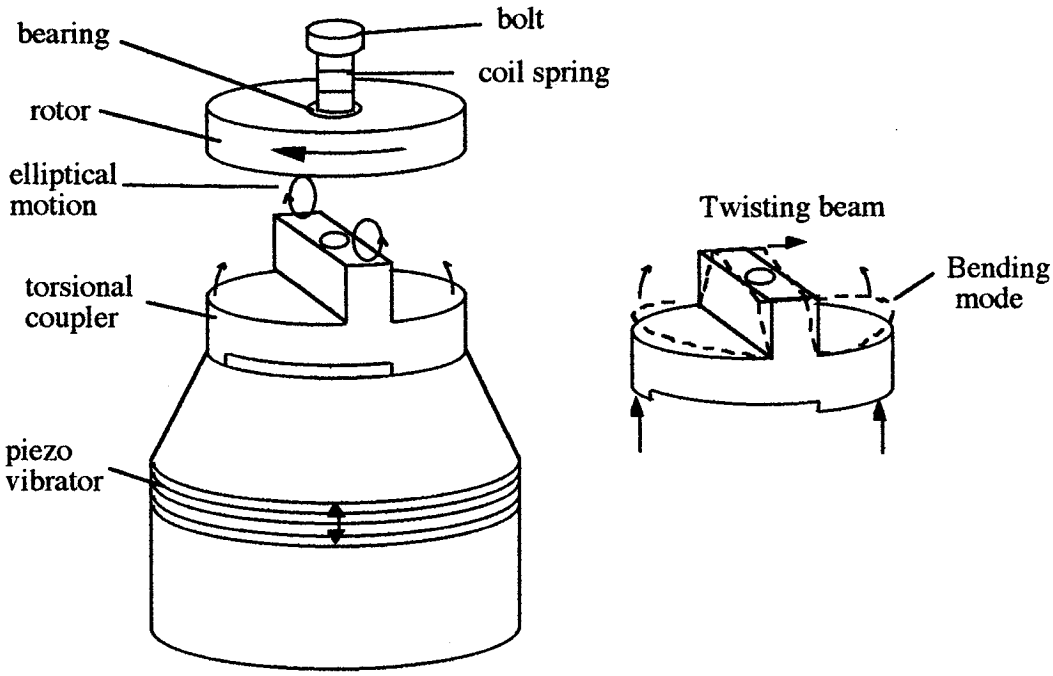

Figure 2.10. Mode conversion ultrasonic motor (MCUM). (Kumada 1985) [6].

Another mode conversion motor was built by Fleischer (1989) [42]. This motor achieves speed of 300 rpm and 2 kg-cm torque. The efficiency of this motor is 35%. He used sputtered TiN and plasma sprayed Al_2O_3 coating at the contact surface between the stator and the rotor to increase the coefficient of friction as well as wear resistance.

Quasi Static Motors

Quasi-static motors, as the name indicated, operate at low frequencies usually below the resonance frequency and therefore do not depend on resonance to achieve motion. Macroscopic motion is achieved by taking numerous microscopic steps. The quasi-static motors are usually used in high precision positioning applications since the

microscopic steps are very small. There are three types of motors in this category of solid state motor.

Inchworm Motors

The word Inchworm is actually a trade mark of Burleigh Instruments. The company was one of the very first to successfully build and market the inchworm motors commercially. Burleigh Instruments also holds numerous patents on Inchworm motor (1975) [55]. The construction of the inchworm motor is illustrated in Figure 2.11.

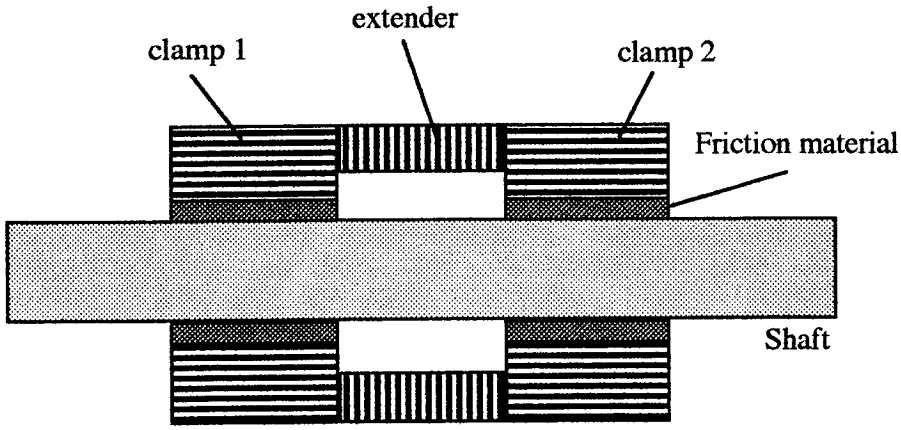

Figure 2.11. Schematic of an inchworm motor.

The configuration of the inchworm motor is similar to the construction of the hybrid transducer. However, the inchworm motors operate at very low frequency and is stable at low speed. The hybrid transducer motor can not operate at low frequency because it depends on the slow response time of the slider/rotor to break or maintain contact..

The operation of the inchworm motor mimics a worm inching away. The operating sequence of the inchworm motor consists of six basic steps.

1) Clamp 1 extends to clamp on to the shaft.

2) Clamp 2 contracts to release the shaft.

3) The extender extends to move clamp 2 further from clamp 1 to provide the step.

4) Clamp 2 extends to clamp on to the shaft at its new position.

5) Clamp 1 contracts to release the shaft.

6) The extender contracts to move clamp 1 to its new position.

Macroscopic motion is achieved by continuously repeating the above sequence. The step size of the motor is dictated by sequence #3 and can be controlled by the voltage applied to the actuator of the extender. The resolution of the inchworm motor thus can be made smaller than the motor's step size and is an advantage of the inchworm motors. This resolution is made possible by clamping with one clamp, releasing the other clamp and varying the voltage signal supplied to the extender to move within the step infinitely. The velocity of the inchworm motor can be controlled by the operating frequency, step size or both. The direction of the motion of the motor depends on the phase of the two clamping sections and therefore can be changed.

In the inchworm motor, the clamping mechanisms must provide the holding force when in contact. This clamping mechanism must also completely break the contact when the holding force is not required during the cycle. Preloading the rotor to the stator is therefore not possible. The tolerance in the rotor must be tight because variation in the dimension of the rotor will lead to variation in the distance the clamping mechanism must travel before making contact. If this distance is greater than the displacement of the clamping mechanisms, contact will not occur hence no holding force.

The inchworm motors are less popular than the ultrasonic motors. Improvements are still being made to increase the performance of the inchworm motors. The motor marketed by Burleigh Instruments as illustrated in Fig. 2.11 has very simple construction. The motor consists of two piezotubes fitting onto a shaft. The inner diameter of the piezotubes decrease when voltage is applied thus generate the clamping forces onto the shaft. Another piezotube, which extended longitudinally when voltage is applied, connects

the two clamping tubes together. This motor has a travel range of 25 cm. The speed of the motors is 2 mm/s with a load capability of 1.5 kg. These inchworm motors have found their ways into many high precision positioning application. However, the performance of these motors are plague by wear between the clamping tubes and the shaft. Since the mechanical strains of these tube under the piezoelectric effects are very small, as the gap between the tubes and the shaft decreases due to wear, the clamping force decrease until it can no longer hold onto the shaft. The tolerance in the shaft is critical to the operation of the motor. The total mileage of this motor is in the range of a few meters. Also due to its construction, the piezoelectric actuators in this motor also directly carry the external load exerted on the motor. Newton (1994) developed a linear motor using the same inchworm principle [2]. A novel clamping mechanism was used in his motor to minimize the shear load on the clamping actuators. The motor has a maximum speed of 12 mm/sec and a static holding force of over 5 kg. Zhang (1994) also developed an inchworm motor utilizing flexure mechanisms [56]. The speed of this motor is 2 mm/s and force is 1.5 kgf. This motor is reported to have a resolution of 4 nm. Ohnishi (1990) developed a rotary inchworm motor using obliquely poled piezoelectric actuator to generate rotary motion [57]. This motor can deliver 18 kg-cm static torque and 2.0 kg-cm dynamic torque with speed of less than 1 rpm. Figure 2.12 shows the schematic of the construction of this motor.

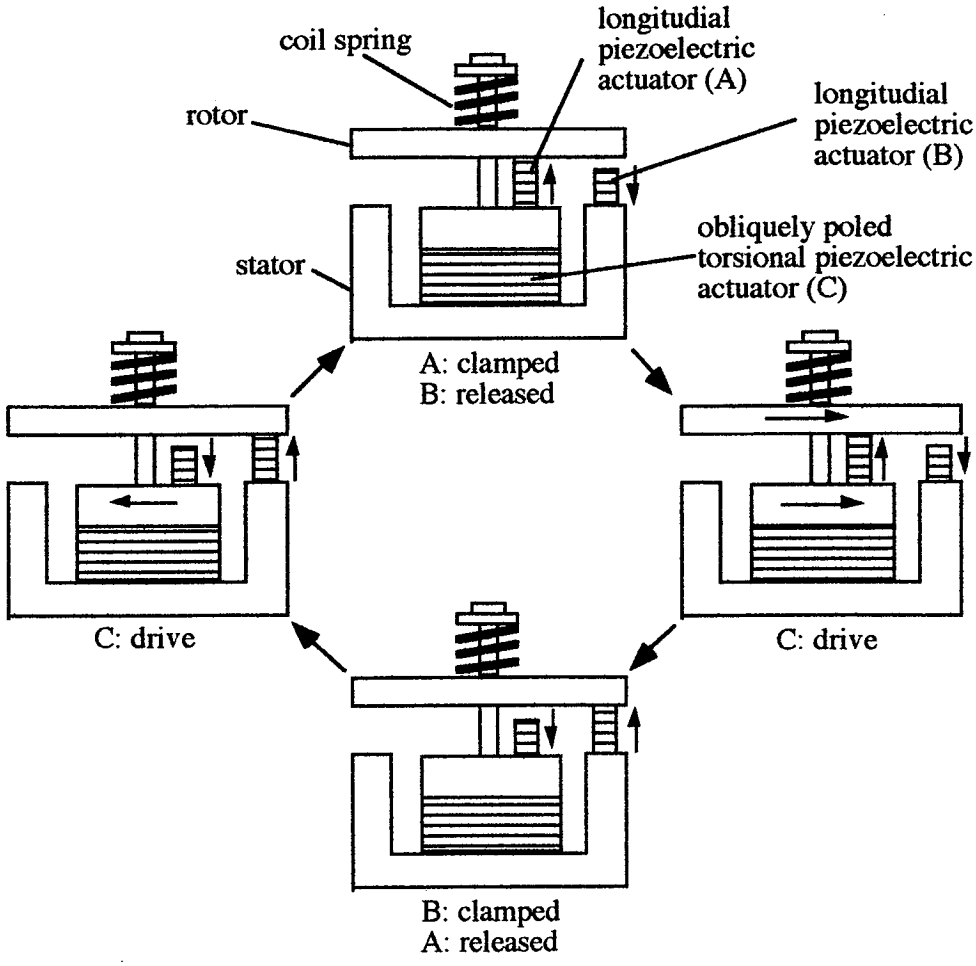

Figure 2.12. Schematic of a rotary inchworm piezoelectric motor (Ohnishi, 1990).

Bexell (1994) also built his rotary inchworm motor using four bimorph elements that can bend and extend [8]. The bimorphs are placed 90 degrees apart from each other. The opposite bimorphs operate together. The two set of bimorphs provide alternate clamping force on the rotor. This motor achieve a rotational speed of 0.7 rad/s with a torque of 16 mN/m. Shimizu (1990) developed his inchworm motor utilizing three set of clamps to provide stability during clamping [58]. The resolution of this motor is 5 nm and the range of travel is 5 mm. Meisner (1994) combines piezoelectric and magnetostrictive actuators to built his inchworm motor [59]. In this motor, the piezoelectric actuators are used to provide the clamping force and the magnetostrictive actuator is used to provide the stepping

motion. This motor provides a maximum holding torque of 115 N and speed of 2.5 cm/s. Because of the nature of the inductance in the magnetostrictive's coil and the capacitance in the piezoelectric actuators, the phase between the driving signals in this motor is said to be much simpler. Pandell (1996) developed a "caterpillar" motor [60]. This motor consists of two extenders and three flexure clamping mechanisms. By having two extenders, the motor can operate in both inchworm mode and caterpillar mode. In the caterpillar mode, the first half of the motor moves to a new position (one extender) then successively followed by the second half. The extra clamping mechanism and the caterpillar operation reduces the glitches in the motor and improves the precision. The motor achieved a maximum speed of 0.25 cm/s with holding force of 0.28 kgf and dynamic force output of 0.17 kgf. Gui (1995) also incorporated electrorheological fluids in the design of his rotary inchworm motor [61]. In this motor, the near solidification of the electrorheological fluids under the applied electrical filed provides the clamping force while a torsional piezoelectric actuator provides the stepping motion. Dong also built a linear inchworm motor which utilized electrorheological fluid for the clamping sections [62]. A micro moving velocity of 1.5 μm/s and 0.25 kgf push force of the piezomotor were obtained.

Inertial Stepper Motors

The operating principle of the inertia motor relies on the stick slip mechanism. The diagram of the motor is shown in Figure 2.13. In this motor, the rotor has a large mass. The stator consists of a piezoelectric actuator large mass is connect to a piezoelectric actuator. The rotor is in contact with the stator by friction. A saw tooth signal is applied to the actuator. During the ramp portion of the signal, the actuator slowly extends the rotor/mass in the direction of travel. Since the acceleration of the mass is small during this cycle, the force of inertia is also small and can not overcome the force of friction. However, when the signal take a steep dive in the saw tooth, the stator quickly moves back. The force of inertia of the mass is now much greater than the force of friction

between the rotor and stator. The base of the stator is now slips back to its original position while the rotor almost stands still, a cycle is completed. This cycle is repeatedly continuously to achieve macroscopic motion. The direction of the motor can be changed by reversing the saw tooth signal. The travel range of this motor is only limited by the length of the rotor.

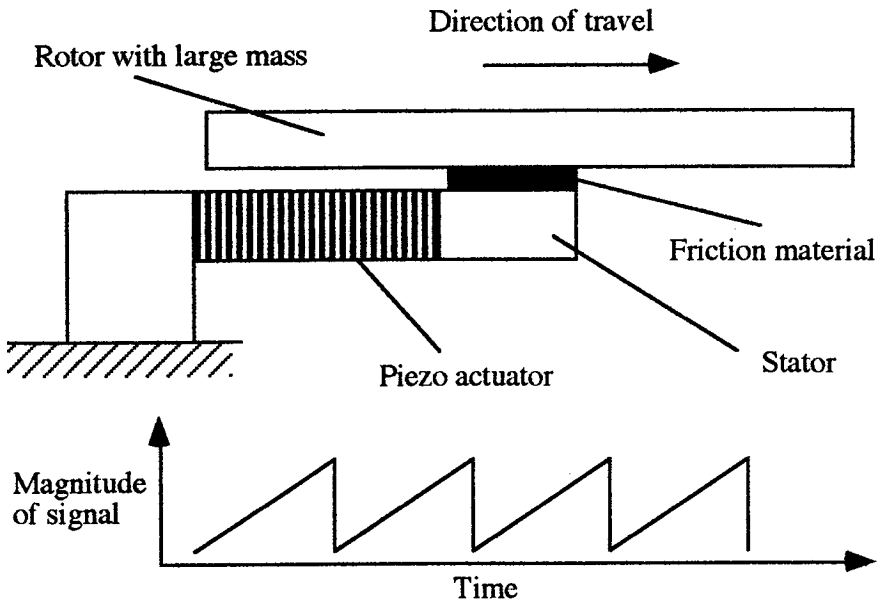

Figure 2.13. Inertial stepper motor.

Due to the stick slip operating nature of the motor, there is a large amount of wear. The inconsistency in the frictional force also effects the precision of the motor step. This type of motor however have the advantage of simple construction and driving circuit. The inertial stepper motors usually produce small force and run at low frequency. The motor will become unstable as the operating frequency approaches the resonance frequency of the motor [63]. The motors are also sensitive to external vibrations [64]. Many examples of the inertial stepper motor can be seen in literature. Neidermann (1988) designed a very compact inertial stepper motor using sawtooth driving signal [65]. Agrait (1992) built an

inertial stepper motor for use in the scanning tunneling microscope [66]. The motor has a speed of 0.5 mm/s in the upward direction, 4 mm/s in the downward direction, and 3 mm/s when travels horizontally. Obviously, gravity plays an important role in the increase in speed in the downward direction. Woodburn (1993) constructed a tubular inertial stepper motor capable of traveling with speed of 0.5 mm/sec and force of 0.1 kgf [63]. He experimented with different driving signals and found that an exponential ramp signal would increase the speed of the motor when operated at higher frequencies. Howald (1992) developed an unusual inertia stepper motor type [64]. He used three actuators to rotate a sphere, creating a three degree of freedom positioner based on the stick slip principle. Judy (1990) developed his inertia stepper motor using a clamp activated by electrostrictive to control the friction force [67]. By adding the active clamping mechanism, this motor can be treated as a hybrid transducer motor when operated at low frequency. This motor begins to resemble a HTUM that operates at low frequency. This motor achieve a maximum speed of 0.48 mm/s with the step size ranging from 0.07 to 1.1 μm and a maximum load of 0.035 kgf.

Direct Drive Motors

The direct drive motor use direct mechanical interface between the actuators and the output motion rather than relies on friction. Hayashi (1992) developed his direct drive cycloid motor which resembles the construction of a harmonic gear assembly [68]. The construction of this motor is shown in Fig. 2.14. In this motor, four piezoelectric actuators are used to create the cycloid motion of the stator. The inner gears of the stator always mesh with the outer gears of the rotor and the rotor is driven. The rotor rotates by an angle equal to the difference in the number of teeth per one circular oscillation of the stator as in a harmonic drive (Hayashi 1992). Hamaguti (1989) also built a similar motor using harmonic gears system [69]. He employed flexure lever arms to amplify the motion of the piezoelectric actuators so that they are greater than the gear height. This motor achieved a

maximum rotational speed of 16 rpm and a maximum torque of 0.14 kg-cm. The harmonic motor has the potential to be very efficient since they are directly driven by piezoelectric actuators in stead of the friction drive. The efficiency in energy conversion between a pair of gears of high accuracy is approximately 98%. This type of motor has potential to be very efficient. King and Xu also built similar direct drive motor around a harmonic gear assembly [70]. Their harmonic piezomotor uses a radial spokes wave generator in which the rotational wave on the flexsline is generated by the appropriate movement of the spokes. The motor was reported to achieve a maximum speed of 32 rpm.

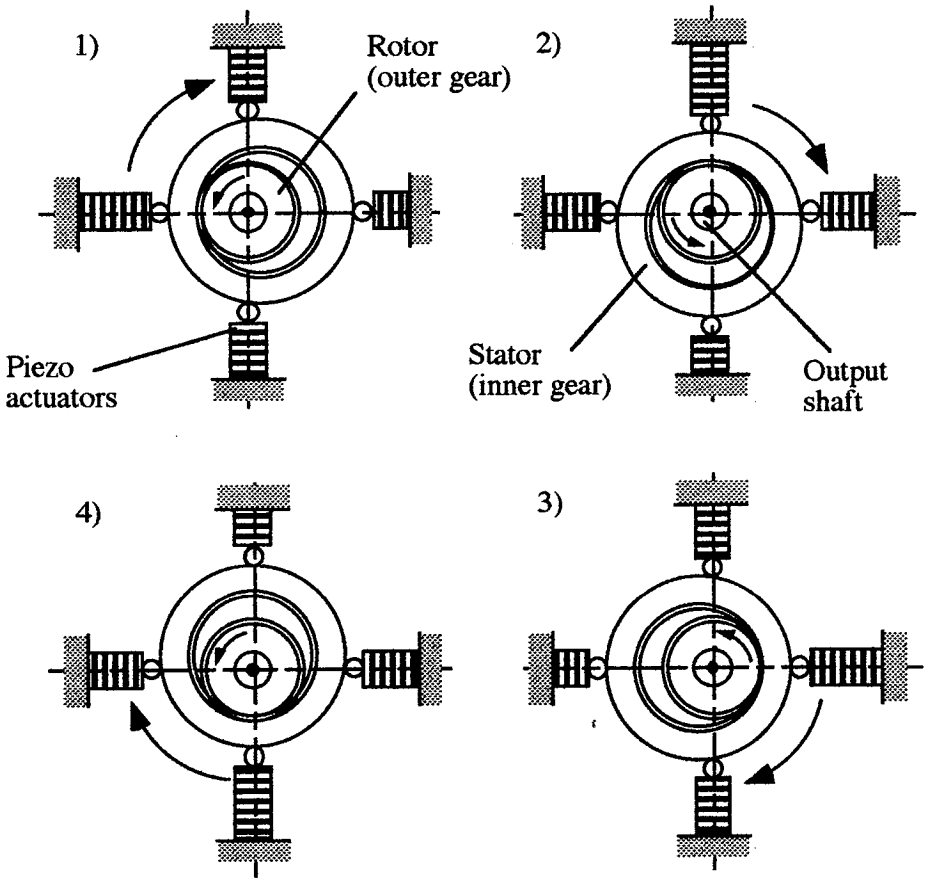

Figure 2.14. Direct drive motor - cycloid motor (Hayashi 1992).

High frequency band motor

This type of motor is fairly new to the research community and is not yet categorized as in Figure 2.1. Recently, Kurosawa (1996) built a surface acoustic wave motor that operated beyond the ultrasonic range [71]. The operating frequency of this motor is in the HF frequency band (3 MHz to 30 MHz). The motion of the Rayleigh wave in an elastic medium is used for this motor. In this motion, a surface point in the medium moves along an elliptical locus similar to a flexural wave in ultrasonic motor. However, the wave motion is attenuated in the thickness direction so that points in the back of the substrate become rigid. This type of motor is suitable for micro actuator in the MEMS (Micro Electro Mechanical Systems) domain because stator transducer is very small so that the wavelength become short and the driving frequency rises.

CHAPTER III

MOTOR DESIGN CONFIGURATION AND OPERATING PRINCIPLE

This chapter covers the details design of the motor and its components. The prototype motor was designed to explore the use of piezoelectric stack in rotary inchworm motor. The motor utilizes the principal electromechanical coupling, d_{33}, for it motion. Similar motor concept using piezoelectric stacks for rotary inchworm motor has been studied by Tojo and Sugihara in their piezoelectric-driven turntable [72, 73]. Their turntable design is capable of achieving high level of positioning resolution and durability. However, the angle of rotation of this turntable is limited to 90° due to their two half-disks design. It is impossible to realize continuous rotation with their motor. The motor design in this dissertation is capable of delivering high torque, speed and unlimited angle of rotation relative to other inchworm motor seen to date. The designed motor also served as a testbed to study new concepts that provide better understanding of the principles and mechanics of the motor. The operating principle of the motor is also presented.

Motor Design Configuration

The motor assembly consists of 4 main parts: one rotor (shell), two clamping mechanisms, and a swinger/extender to provide angular motion. The rotor's role is to convert the cyclic motion of the swinger/extender into continuous motion. The clamping mechanisms alternately grip the rotor to provide the necessary clamping action for force transmission. The swinger/extender mechanism provides a controlled angular displacement between the two clamping mechanisms and is responsible for the output motion of the rotor. To generate the inchworm-like motion, one of the clamping mechanisms is made stationary along with one side of the swinger/extender mechanism. The other clamping mechanism is bolted to the swinger/extender arm which is driven by the piezoelectric

actuator in the swinger/extender mechanism. The alternating clamping action of this mechanism onto the rotor (or housing) during the forward stroke of the swinger/extender results in the small angular step of the rotor. The constructions of the clamping mechanisms and the swinger/extender are monolithic. The flexure hinges are integral part of the components' structure. Stainless steel was chosen as the material choice for the components which could give the flexure hinges infinite fatigue life. These components were fabricated using the Electro Discharge Machining (EDM) process. The EDM process provides high precision and machinability of the components compared to regular machining methods. Figure 3.1 shows the schematic of the assembly of the motor.

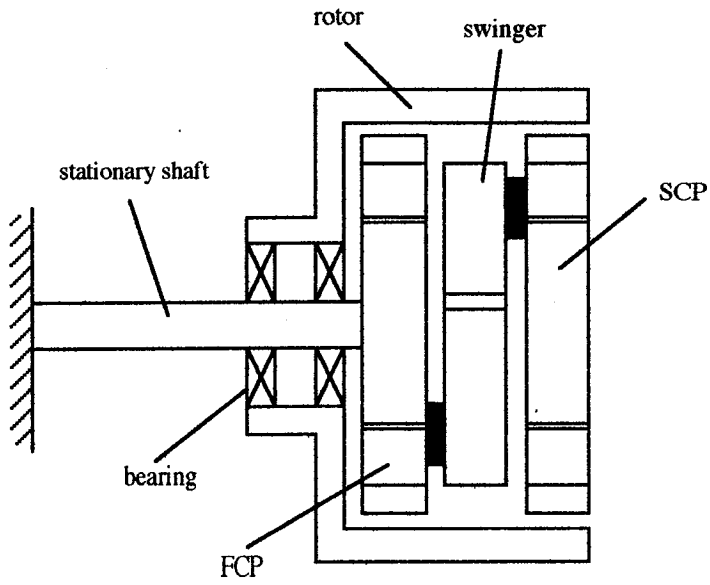

Figure 3.1. Schematic of motor assembly.

Clamping Mechanism

The role's of the clamping mechanism is to provide the clamping force onto the rotor. They supply the necessary friction force to hold or propel the rotor. Each clamping device is driven by two multilayer piezoelectric stack actuators. Since the displacement of the piezoelectric actuator is very small, the motion of the actuator must be amplified to overcome the variation in the rotor diameter from machining tolerance as well as variation

in the rotor surface roughness. This motion is amplified twice through two sets of lever arms. Depending on the relative position of the stack actuator to the hinges, the lever arms provide an amplification factor of about 12 to 15. The amplification factor is set at 12 for the motor. The flexure mechanisms are designed so that all flexure hinges are in compression rather than tension. The end of each flexure mechanism is connected to a contact shoe. The clamping mechanisms, along with the rotor, serve as a "drum brake". When the actuator extends, the contact shoes make contact and exert normal force onto the rotor. Due to the design, the motor itself can serve as a brake/clutch mechanism. Incorporated into the design of the flexure mechanism are the fine-thread adjusting screws (80 threads/inch). These screws allow fine pre-adjustment of the gap between the contact shoe and the rotor. These screws proved to be very critical in operating the motor. The pre-adjustment narrows the gap between the contact shoes and the rotor thus increases the normal force exerted on the rotor by the contact shoes. A stress relief device which consists of steel ball and seats configuration is placed at the interface between the piezo-stack actuator and the flexure lever arm. The configuration is shown in Fig. 3.2. The flat surface of the seat eliminates any stress concentration on the fragile piezoceramic and prevents any bending moment to exert on the piezoceramics actuator themselves.

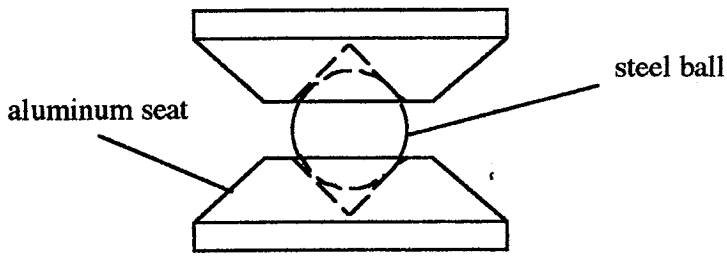

Figure 3.2. Stress relief device.

The actuator is also prestressed to achieve optimum displacement. The prestress allows the PZT stack to work only in varying degrees of compression, thus providing a mechanical

bias that helps avoid failure due to the low tensile strength of the piezoceramic stack actuators. The prestress spring also provides the return force for the lever arms. Figure 3.3 is a photograph of the clamping mechanism, which was fabricated using the EDM process. Detail technical drawings of the clamping mechanism can be seen in Appendix A.

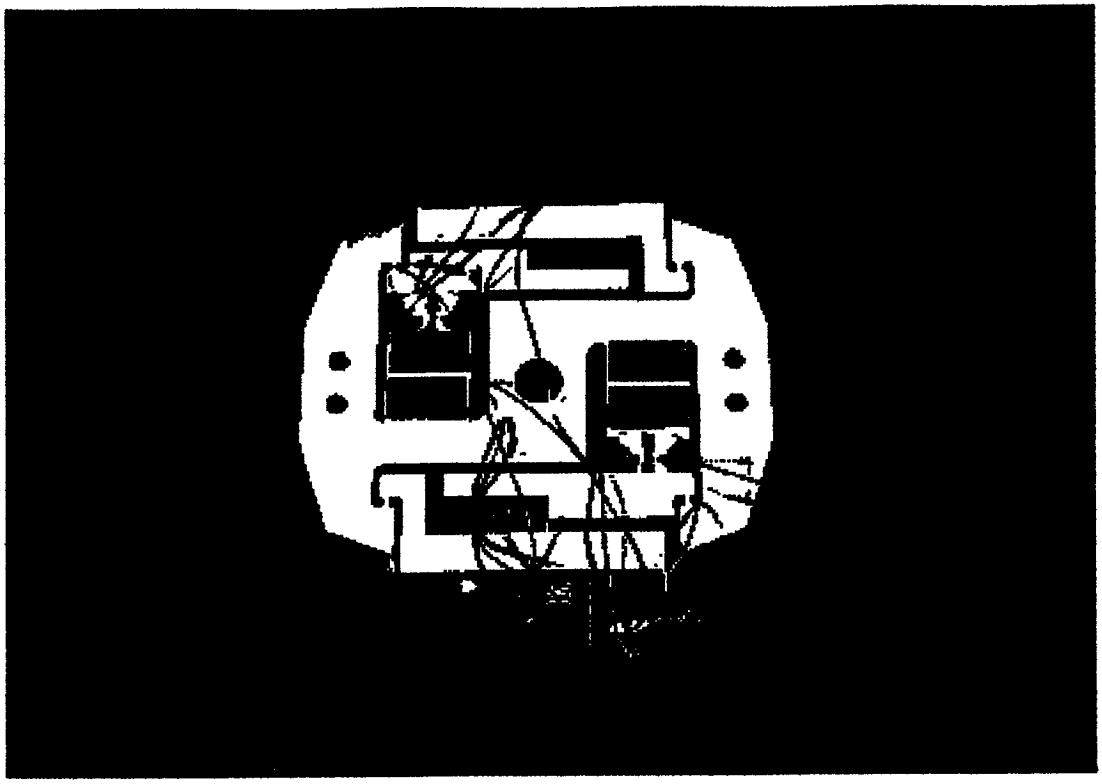

Figure 3.3. Clamping mechanism.

Swinger/extender Device

The swinger/extender provides the cyclic angular motion of the rotating clamping mechanism. By synchronizing the clamping force during one direction of motion of the swinger/extender, the rotor can achieve macroscopic motion in that direction. The swinger/extender consists of one multilayer piezoelectric stack actuator and a flexure mechanism which generates rotation about the center of the motor. The lever arm of the swinger/extender pivots about the flexure hinge to provide arc-like movement at the end of

the pivoting arm. This flexure hinge is strategically located at the center of the motor which is also the center of rotation of the rotor. The base of the swinger/extender is bolted to the stationary clamping mechanism described above. This stationary clamp is referred to as the first clamping mechanism (FCM). Both the base of the swinger/extender and this clamp are stationary. The end of the swinger's arm is bolted to the rotating clamping mechanism and is referred to as the second clamping mechanism (SCM). The arc-like movement of the swinger's arm rotates the SCM. Therefore, as the actuator in the swinger/extender extends and contracts, the second clamping piece will rotate back and forth. The steel ball and seat configuration in Fig. 3.2 also serves as the interface between the actuator and the mechanism in this component. Figure 3.4 shows the photograph of the swinger/extender. Technical drawing of the device can be seen in Appendix A.

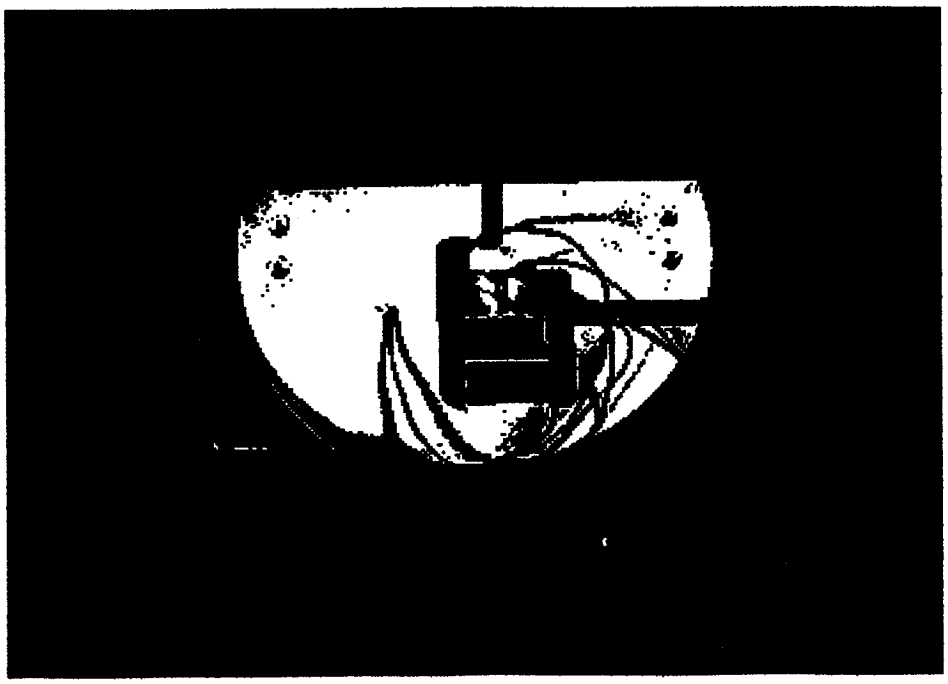

Figure 3.4. Swinger/extender mechanism.

Rotor

The rotor combines successive microscopic step-like motion of the swinger/extender into continuos macroscopic motion. Centering of the rotor with respect to the assembly is achieved by radial bearings. With a more complicated clamping mechanism, e.g., one with a large number of contact shoes, the use of this bearing could be eliminated. The inner race of the bearing is connected to the first clamping device and the base of the swinger/extender through a stationary shaft. The shaft also serves as the mounting/handling piece of the motor. The outer race of the bearing is press-fitted to the rotor and is free to rotate with the rotor. The rotor is a cylindrical shell about 104.14 mm (4.1 inches) in inside diameter, 50.8 mm (2 inches) tall and 4.76 mm (3/16 inch) thick. Figure 3.5 illustrates the construction of the rotor.

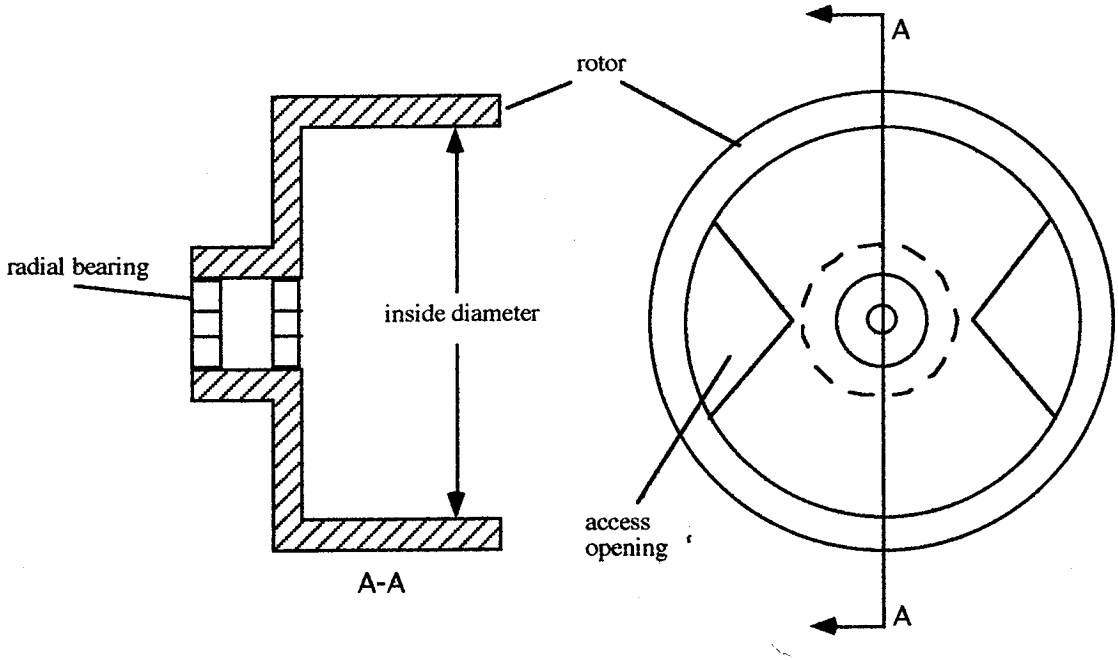

Figure 3.5. Construction of rotor.

The tolerance of the inside diameter of the rotor was measured and is recorded with a variation of less than 18 μm for any points on the rotor. This tolerance is quite impressive by machining standard. But when compared to the maximum displacement of 20 μm of the actuator, the tolerance is quite large. This variation is also affected by the freeplay in the radial bearings. When the motor is oriented horizontally, the force of gravity exerts a moment on the bearing and tilt the rotor which results in slightly off center rotation. A pair of high precision thrust bearings would eliminate this problem. The swinger/extender and clamping mechanisms assembly are fitted inside the rotor. Figure 3.6 shows the actual photograph of the motor assembly.

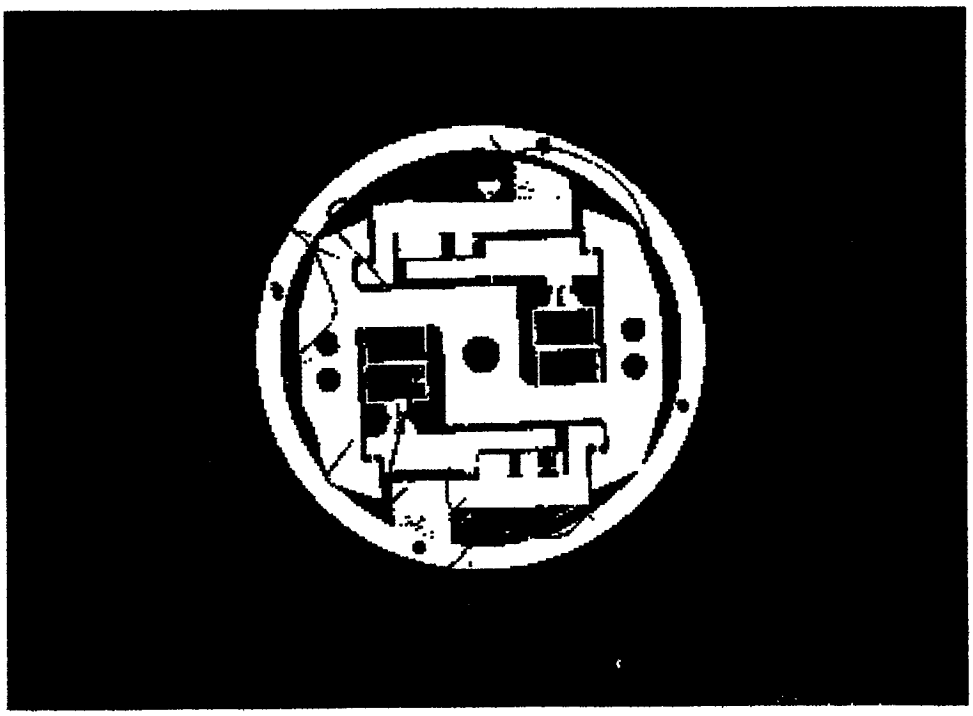

Figure 3.6. Actual photograph of motor assembly.

Multilayer actuators

The multilayer stack actuators were procured from Morgan Matroc Inc. These are PZT-5H type (soft PZT) stacks with the electromechanical coupling coefficient d_{33} of $550x10^{12}$ m/V. Each stack is 20 mm high, 16.5 mm by 16.5 mm square cross section and has approximately 150 layers. The capacitance of each stack is about 5.8 μF. With an input of 250 volts, the stack gives a free displacement of approximately 20 μm. Although these soft PZT stacks have a higher loss factor which could result in heating during operation, they will allow a proof-of-concept for the motor design.

Operating Principle

The motor is operated based on the inchworm principle. The operating cycle of the motor consists of seven successive steps, as shown in Fig. 3.7. The sequence of the steps are as follows:

1) The contact shoes in the SCM extend and clamp onto the rotor.

2) The arm of the swinger/extender rotates the SCM and the rotor.

3) The contact shoes in the stationary FCM extend and clamp onto the rotor (the rotor now is being held by both clamping pieces)

4) The contact shoes in the SCM contract and release the rotor (the rotor is still being clamped in place by the first clamping piece).

5) The swinger/extender arm rotates the SCM to its original position.

6) The contact shoes in the SCM extend and clamp onto the rotor.

7) The contact shoes in the FCM contract and release the rotor.

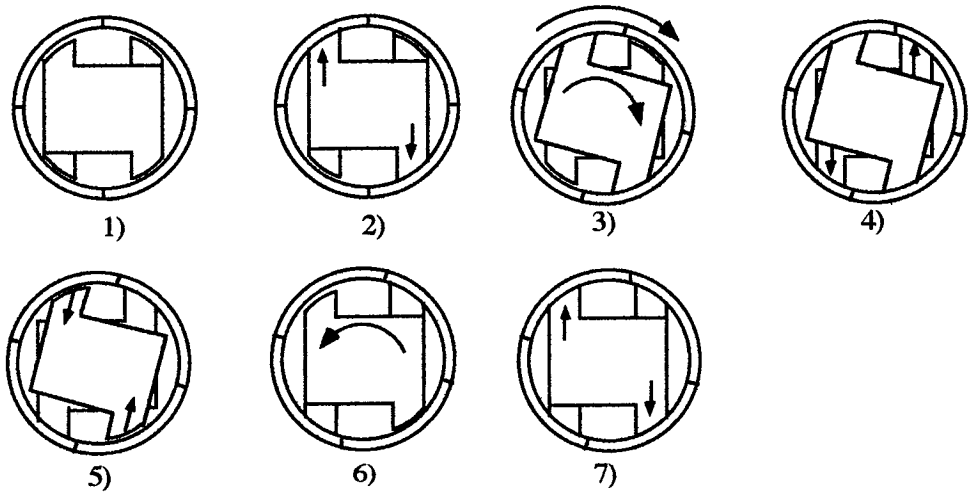

Figure 3.7. Motor operating sequence.

Continuous motion of the motor is achieved through repetition of the above sequence. There are two ways to control the velocity of the motor. One method is to control the step size of the swinger/extender by controlling the voltage across its actuator. The second method is to control the frequency of occurring of these steps. The faster the repetition of the cycle, the higher the speed of the motor. This, of course, assumes that all substructure dynamic phenomena of the motor is quasi-static in nature. Friction converts the motion of the swinger/extender to the motion of the rotor. Friction also provides the holding torque of the motor. The common driving signal for the motor is to use three ramp signals 90° out of phase with each other. The phase of the FCM and SCM is 180° apart while the phase of the swinger/extender is 90° relative to both of them. Square waves are also commonly used but they are mechanically adverse for the piezoceramic actuators and decrease their useful life. The large capacitance of the actuators make it difficult for the amplifiers to drive them at higher frequencies. The square waves also have the disadvantages of high acoustic noise and stack wear. Sinusoidal signals are also common to drive inchworm type motor because they are easily generated.

CHAPTER IV

MOTOR CHARACTERISTICS

Clamping mechanism

The role of the clamping mechanism is to provide the clamping action to the rotor. The clamping mechanism was first tested for its force output by the contact shoe. A load cell was placed above the contact shoe to measure the normal force output of the shoe itself. The force output was tested using a 20 Hz sinusoidal input at different voltages. The force output was also measured against the initial gap between the contact shoe and the load cell to duplicate the gap between the rotor and the contact shoe in operation. Figure 4.1 shows the clamping force versus the contact gap at different input voltages.

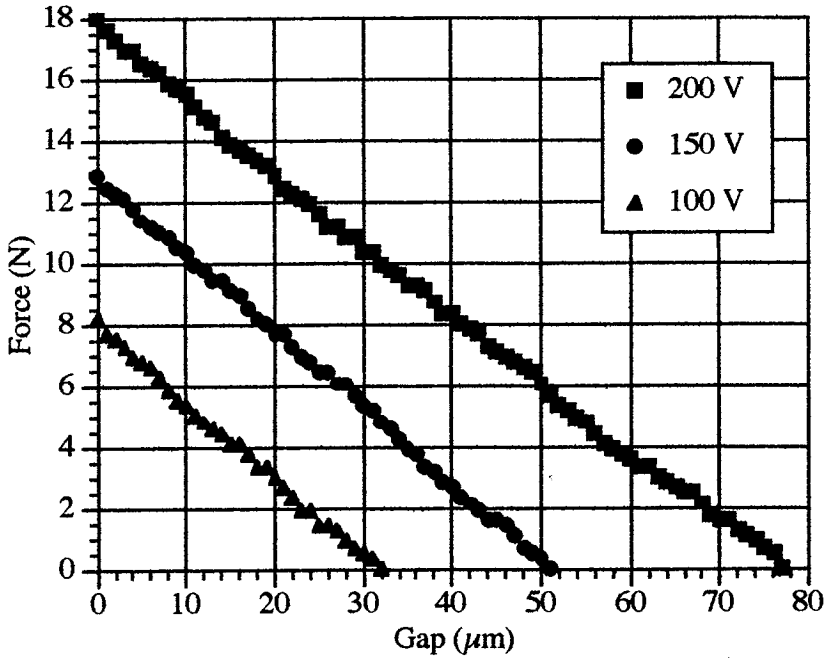

Figure 4.1. Clamping force of contact shoe versus contact gap.

From the figure, the clamping force is proportional to the input voltage into the piezoelectric actuator. For each voltage input, the clamping force decreases linearly as the gap increases. The clamping force is zero as the gap exceeds the strain of the actuator. Although PZT stacks are said to have a high output block force, in reality these stacks can not produce high force while providing large displacement. The high force usually published in piezoelectric actuator brochures is somewhat misleading and inaccurate. In some cases, the force published is calculated using the strain of the actuator and its Young's modulus. Figure 4.2 shows the actual clamping force profile produced by the contact shoe with zero gap when driven by a sinusoidal signal.

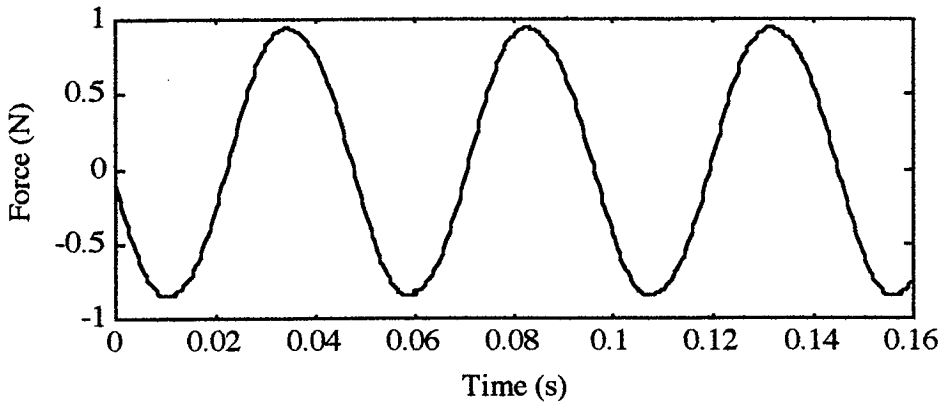

Figure 4.2. Clamping force of contact shoe versus time without gap.

The force produced by the same input condition but with an initial gap is shown in Fig. 4.3. In this figure, the magnitude of the force decreases and the shape of the output force curve is also changed.

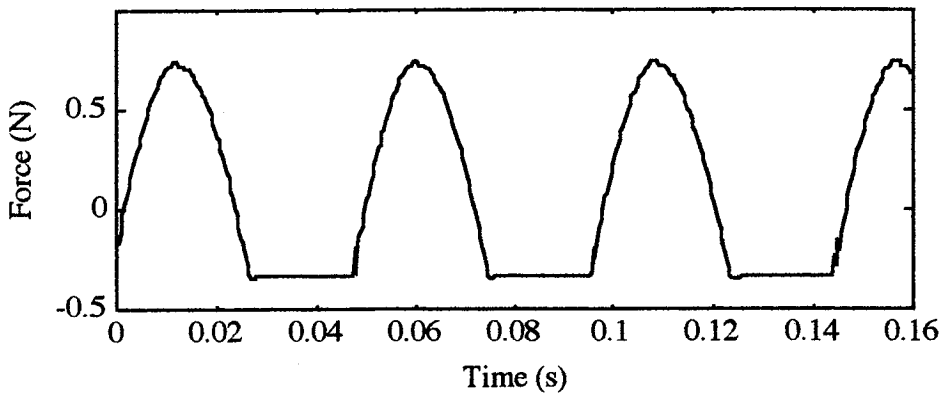

Figure 4.3. Clamping force of contact shoe versus time with initial gap.

The flat portion at the bottom force curve is the result of the gap between the contact shoe and the rotor. During this time, the shoe is not physically in contact with the rotor, thus no clamping force is exerted. The clamping force profile is very crucial to the performance of the motor.

To conceptualize this, consider Figures 4.4a, 4.4b, and 4.4c which show the force output of the three segments of the motor with and without initial gaps when driven with sinusoidal signals. As shown in Fig. 4.4b, the overlapping area between the first and second clamping force curve decrease and disappear as the gap increases. The disappearance of the overlapping area in Figure 4.4c results in the release of the motor by one clamping mechanism before the other clamping mechanism can clamp on. Under loading, this early release will result in rotating in the reverse direction of the motor since the rotor is not clamped during this brief period. The decrease or disappearance of the overlapping area means lower total clamping force during the transition period between the FCM and SCM. If the load is higher than this total clamping force, the motor will rotate in the reverse direction due to slippage from inadequate clamping force. Slippage will cause wear of the contact shoes and the rotor. Slippage will also deteriorate the open loop resolution of the motor. However, this phenomenon will not affect motor rotation under

the no load condition since there is no load to cause slippage (unless it is generated by the inertia force of the rotor).

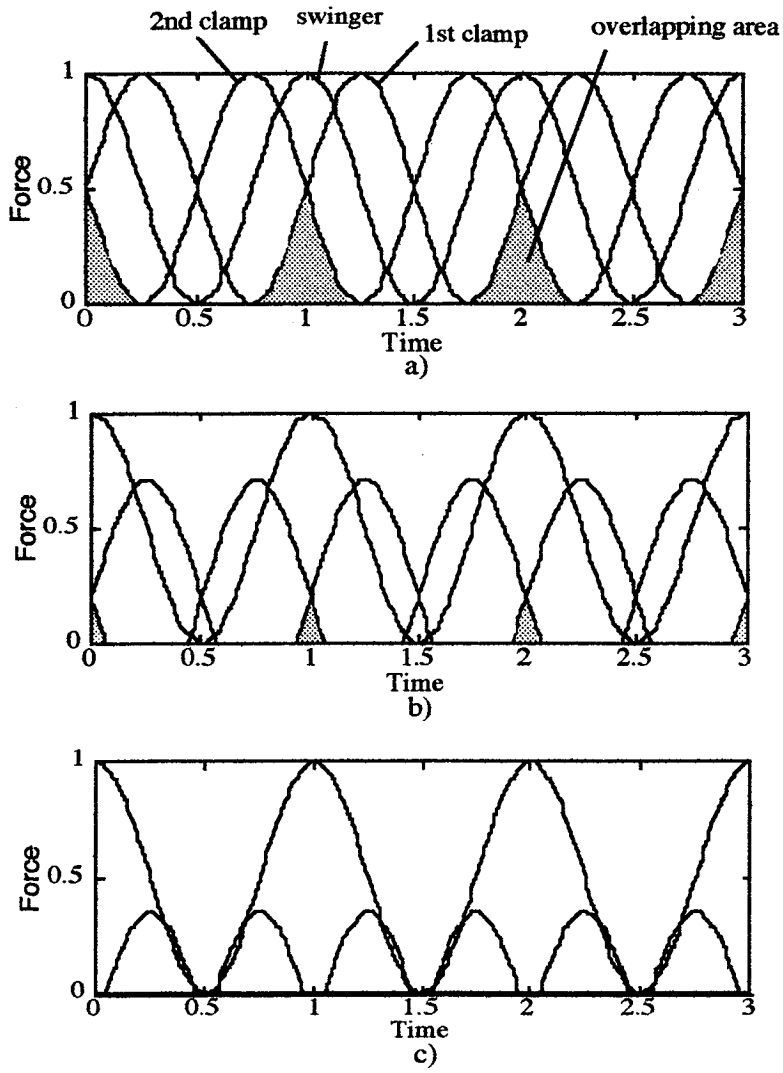

Figure 4.4. a) Force output form of three parts of motor without gap,
b) With small gap, c) With large gap.

Transfer functions for the clamping mechanism were performed using a Tektronix 2642A Fourier Analyzer and noncontact displacement transducer from Lion precision. Figure 4.5 show the transfer function of the contact shoe (clamping arm). The first natural frequency of the clamping arm is at about 360 Hz.

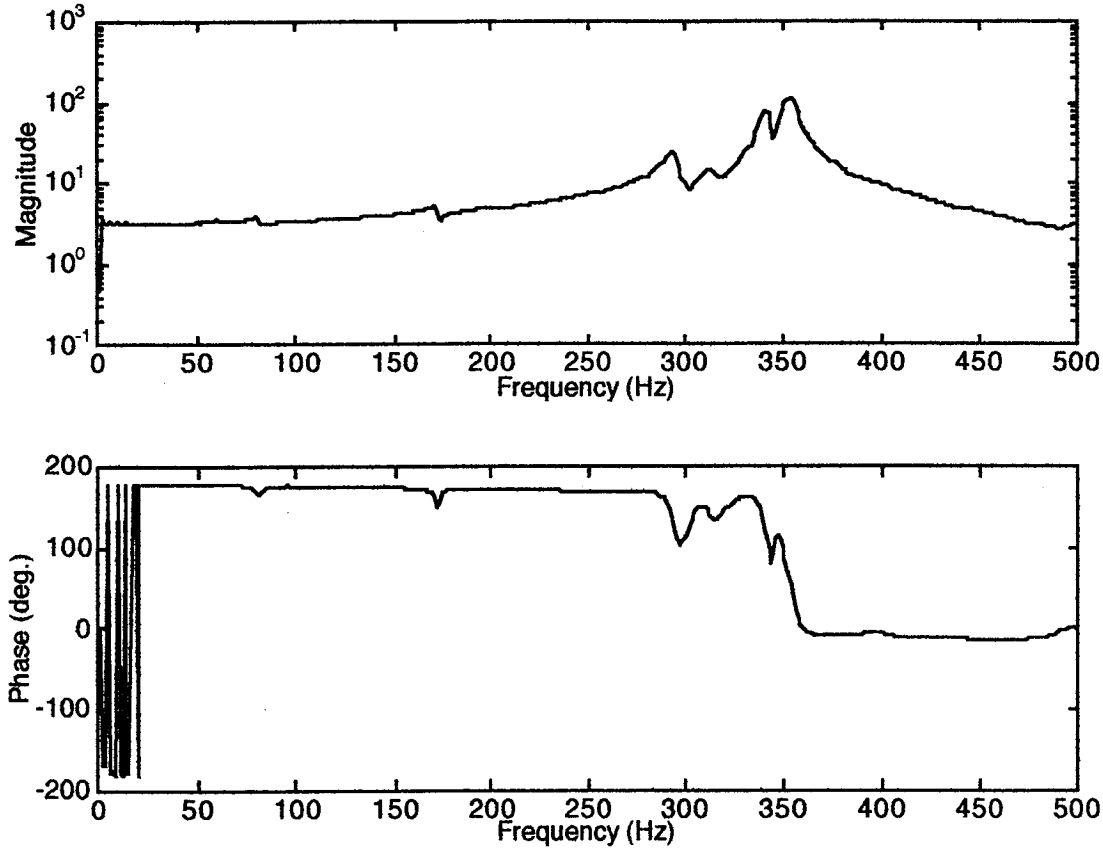

Figure 4.5. Experimental transfer function of clamping arm.

Swinger/extender

The performance of the swinger/extender was also studied for its torque output. A load cell was placed at the end of the swinger/extender arm to measure the torque output of the swinger/extender mechanism. Again using a 20 Hz sinusoidal input, the torque output of the swinger arm is 0.450 Nm at 100 V peak-to- peak; 0.70 Nm at 150 V and 1.01 Nm at 200 V. As in the case of the clamping mechanism, the torque output of the swinger/extender increases linearly with increase in input voltage.

The transfer function between the input signal and the swinger/extender arm as bolted to the second clamping mechanism was taken with and without the clamping

mechanism clamped onto the rotor. The first column of Figure 4.6 shows the transfer function of the swinger/extender arm without coupling with the rotor.

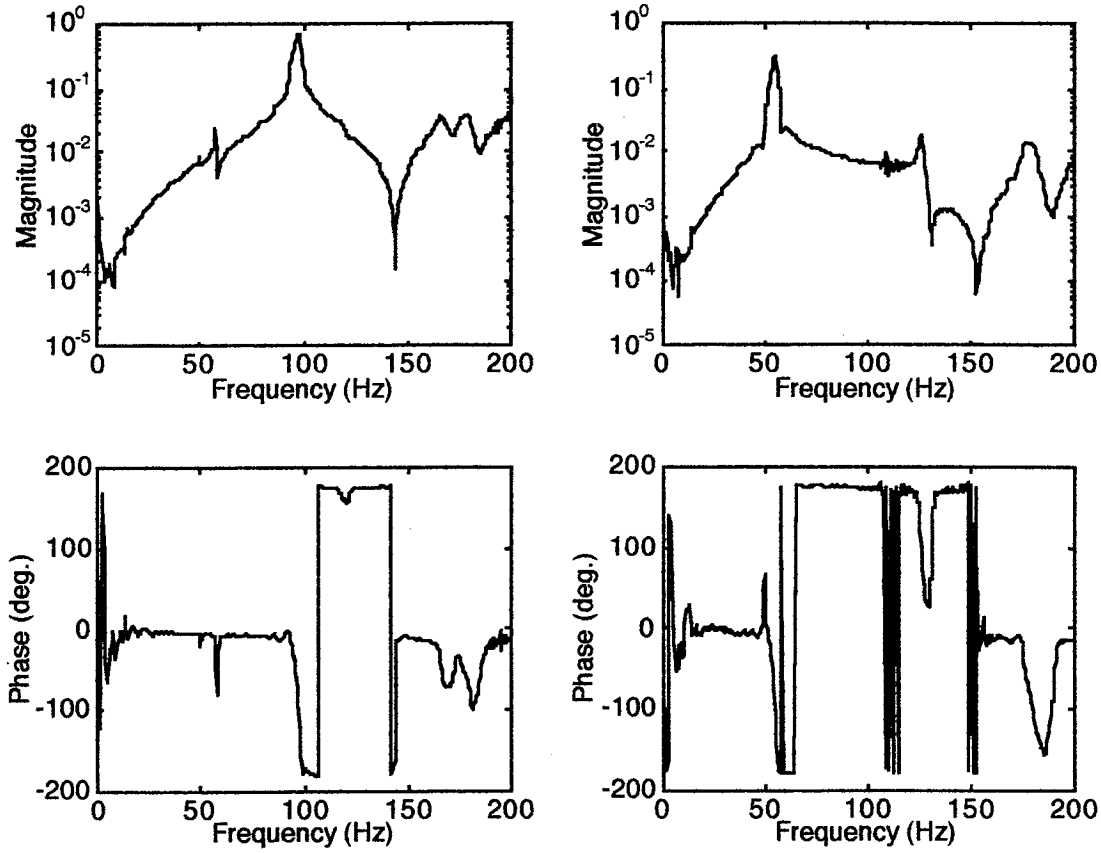

Figure 4.6. Transfer function of motor.

The first in plane mode of the swinger/extender arm without coupling with the rotor is at 98 Hz. The second column in Fig. 4.6 shows the transfer function of the swinger/extender when the second clamping piece is coupled with the rotor. With the added inertia of the rotor, the first natural frequency decreases to 57 Hz. In operation, the motor is coupled with the rotor during the first half cycle and is uncoupled with the rotor in the second half of the moving cycle. Since the inertia properties of the motor change with time, the system

exhibits nonlinear behavior. External loading is also expected to reduce the frequency of the coupling mode because more inertia is added to the system.

Motor preliminary performance

The motor was tested for its performance such as speed, dynamic and holding torque. The efficiency of the motor in converting electrical power to mechanical power was also calculated. Motor torque was tested by hanging different weights with a string attached to the cylindrical portion of the motor cover. The moment arm is 19.05 mm (0.75 inch) from the center to the cylindrical surface. The schematic of the set up is shown in Fig. 4.7. For the static holding torque test, 200 volts DC were applied to the stationary clamping mechanism and a maximum hanging weight of 111.25 N was recorded before slippage occurred. Therefore, if the motor is to be used as a brake, a braking torque of 21.2 Nm would be achieved.

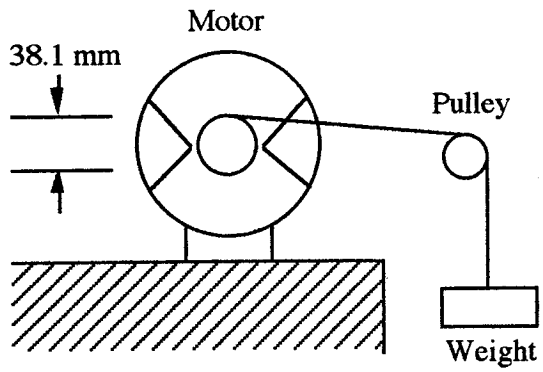

Figure 4.7. Motor test setup.

Speed vs. voltage

For the speed versus input voltage test, the amplitude of the voltage input into the swinger/extender section varied while the amplitude of the voltage input into the clamping mechanisms remained unchanged at 200 volts. The test was performed at a 60 Hz input

signal at which maximum speed is attained within the frequency range tested for any given input voltage. The motor speed increased linearly with input voltage into the swinger section as shown in Fig. 4.8.

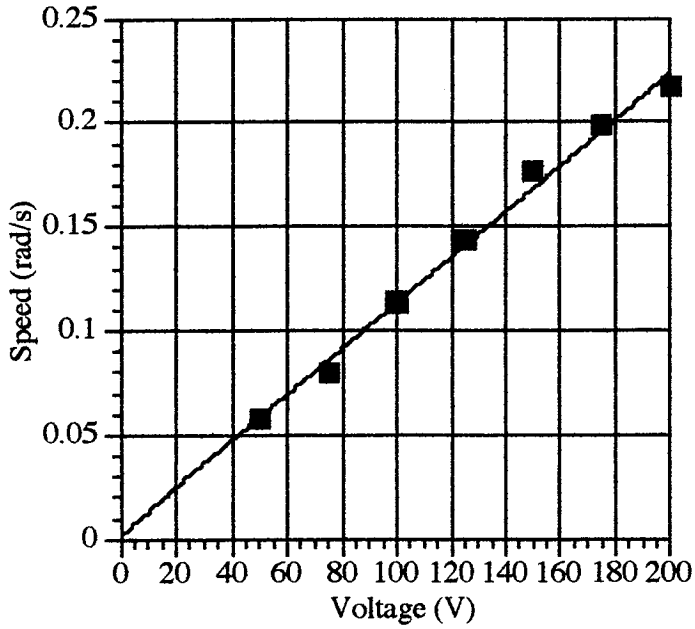

Figure 4.8. Motor speed vs. input voltage into swinger/extender.

Speed vs. frequency

In this test, the voltage input into the swinger/extender is 160 volts while the voltage input into the clamping mechanism is at 200 volts. Figure 4.9 shows the motor speed versus input frequency under no load condition. The frequency at stalling is at 65 Hz experimentally. The stalling frequency is in the 57-98 Hz range, which is between the first natural frequencies of the swinger/extender when coupled and uncoupled with the rotor. This frequency is suspected to be the resonant frequency of the system. At this resonance frequency, the swinger arm experiences a phase change due to a local resonance in the swinger arm.

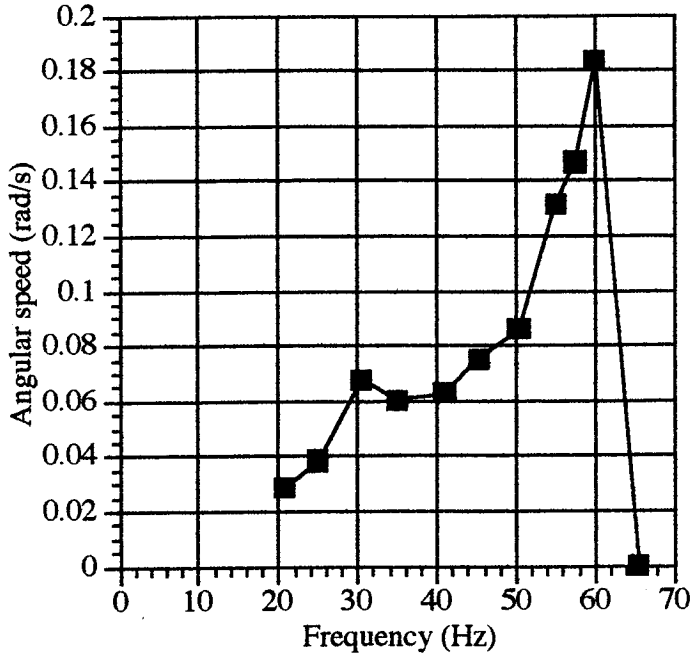

Figure 4.9. Motor speed versus input frequencies without load.

The peak in speed at 60 Hz is the results of operating near the torsional resonance frequency where the swinger/extender arm has a larger amplitude and the phase of the two clamping mechanisms are still within the phase difference limit with respect to the swinger/extender. The speed of the motor was also measured under different torque loads (0.085 Nm-0.509 Nm). The results are plotted in Figure 4.10. From the figure, the speed decreases as the weight loading increase. The speed is highest at 60 Hz and stall occurs at 70 Hz under higher loading (0.170 Nm-0.509 Nm).

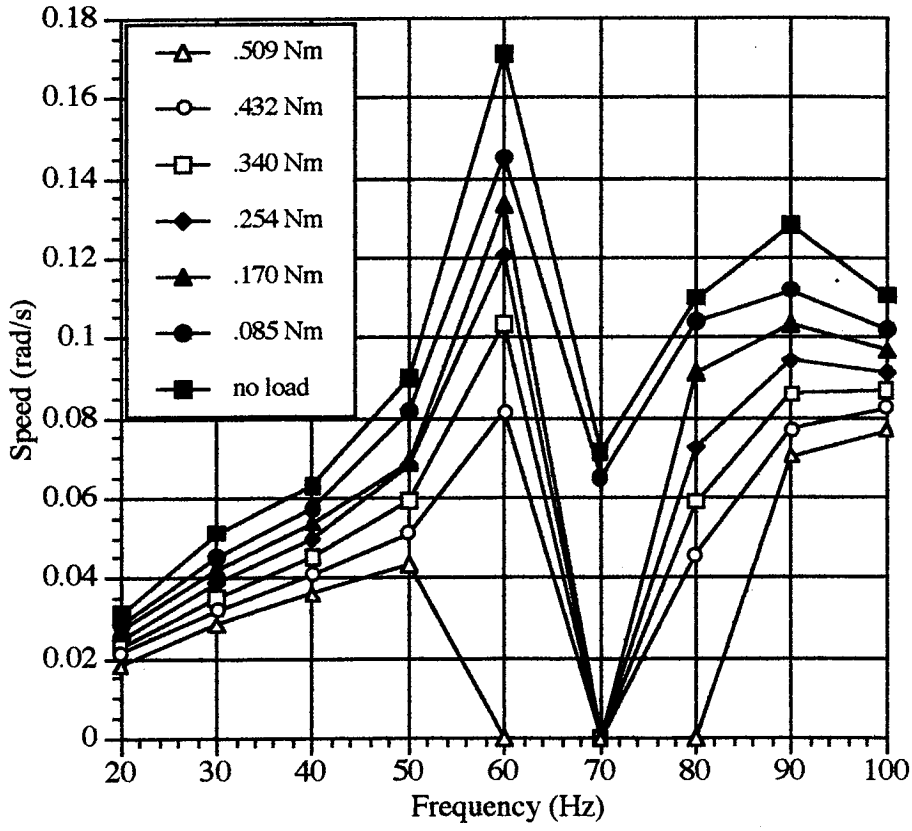

Figure 4.10. Motor speed versus frequency at different torque loads.

The decrease in speed is caused by the reduction in step size and largely by the slippage of the clamping actions as shown experimentally in Fig. 4.11. The reduction in the inchworm step cycle is caused by the decrease in the forward step but largely caused by the slippage of the rotor under load .

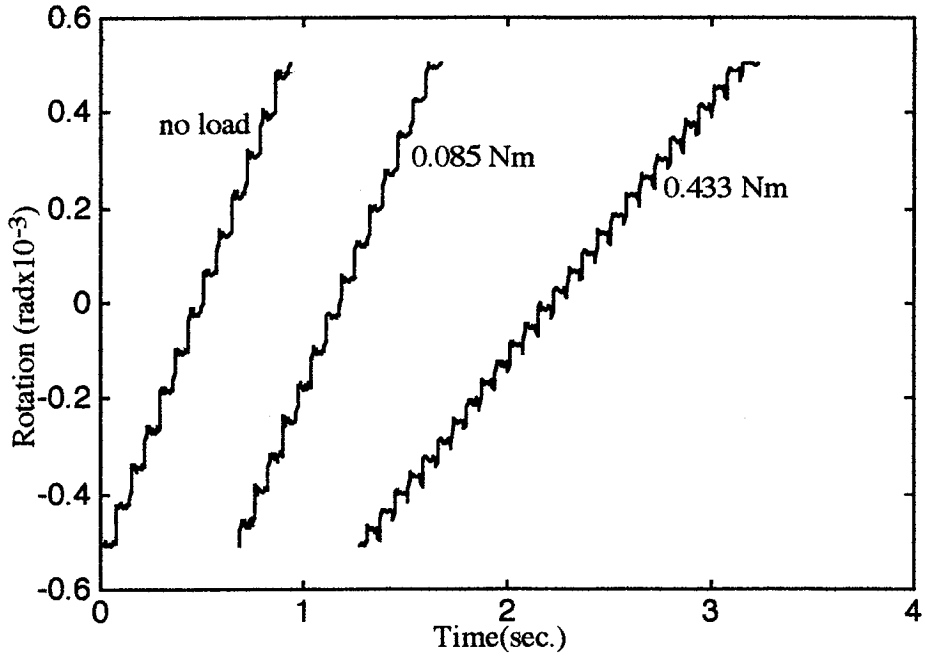

Figure 4.11. Motor steps taken experimentally.

Figure 4.12 shows the detailed simulated step of the rotor. In region A, the rotor moves forward as the second clamping mechanism clamps onto the rotor and rotates forward by the swinger. Region B shows the backward (slippage) movement of the rotor. This slippage is a result of a small or negligible overlapping clamping force between the two clamping mechanisms as discussed above. Region C shows the stationary position of the rotor as it is held on by the first clamping mechanism. The rotor can also slip backward in this region if the load is higher than the clamping force, as shown in this case. Region D represents another slippage situation as the transition between the two clamping mechanisms occurs. The slippage in region B is less than in region D because of the forward momentum of the rotor. If the total slippage in region B and D is higher than the displacement in region A, the motor will rotate in the reverse direction. The slippage indicated that the torque output of the motor depends on the dynamic holding torque of the clamping mechanisms, rather than the torque produced by the swinger/extender. This

slippage was also observed in the rotation of the rotary inchworm piezoelectric motor using torsional elements, developed by Ohnishi [57].

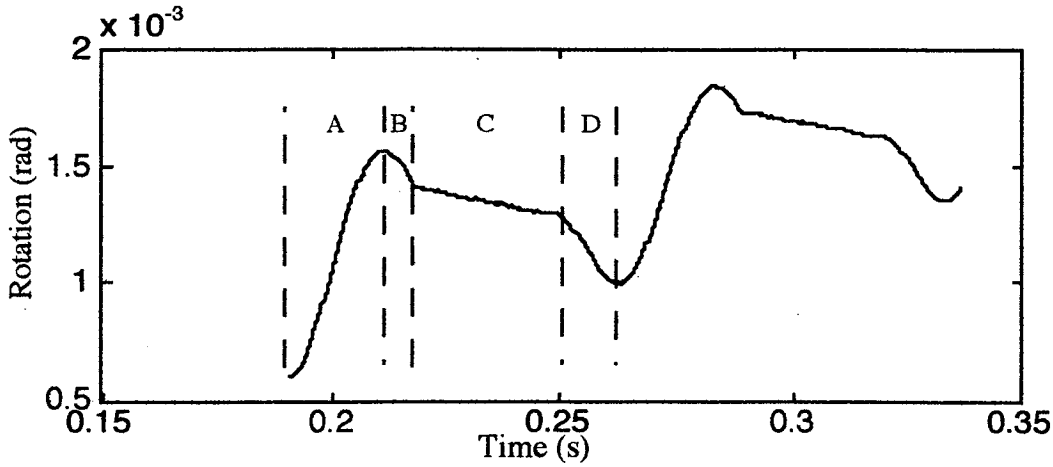

Figure 4.12. Detail step of motor.

Motor speed versus bias voltage

To simulate the effect of the gap tolerance, a negative bias voltage was put into the clamping mechanisms in addition to the 0-200 volts sinusoidal signal. This negative bias voltage will flatten the bottom portion of the sinusoidal shape of the clamping force curve as discussed previously (Fig. 4.3). The negative bias voltage creates the same effect as the gap between the contact shoe and the rotor. The motor speed at different loads is plotted against the bias voltage in Fig. 4.13. The input frequency in this case is 60 Hz.

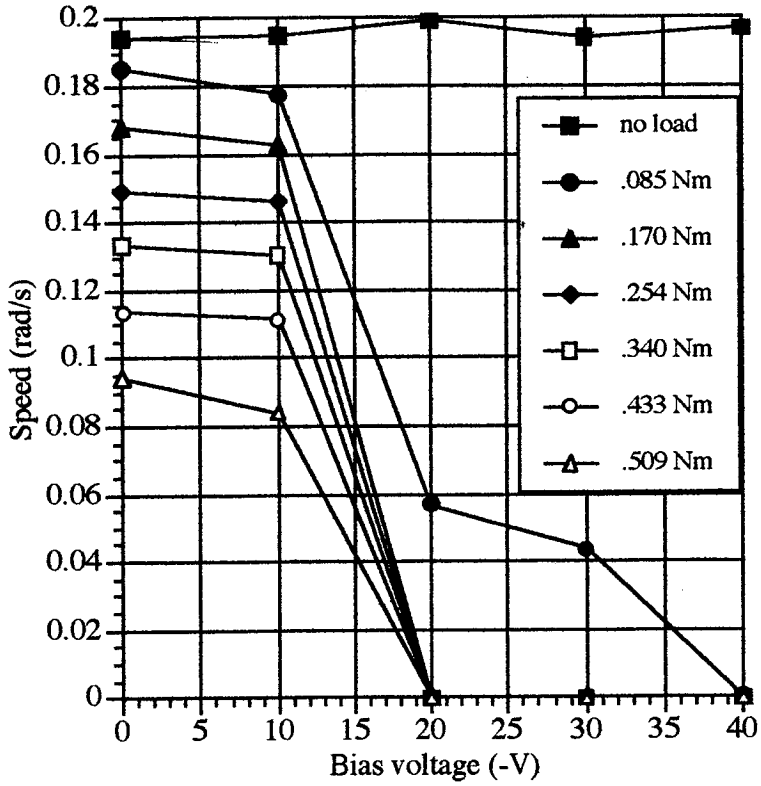

Figure 4.13. Motor speed versus bias voltage at different loads.

From Fig. 4.13, for a small bias voltage of 20 volts, the motor stalls under very small torque load. The speed is unaffected by the negative bias for the no load condition, as expected. This result confirms the important role of the gap tolerance between the contact shoes and the rotor.

Motor efficiency

The efficiency of the motor was calculated using conservative approach. The efficiency of the motor is defined as the ratio of the external mechanical power produced by the motor and the power consumption of the motor

$$\eta = \frac{P_o}{P_i} \tag{4.1}$$

where P_o is the external mechanical power output produced by the motor in lifting weight per unit time. P_i is the power input into the motor in this case is the power consumption of all the piezoelectric stacks. The power consumption of all the stacks in the motor can be easily estimated [74, 75]:

$$P_i = 2\pi f C V^2 \tan\delta \tag{4.2}$$

where C is the capacitive loading, V is the rms of the input voltage and tanδ is the loss tangent of the PZT. The external mechanical power output produced by the motor is the work performed per unit time

$$P_O = mgh/t \tag{4.3}$$

in which m is the mass of the hanging weight and h is the height that the weight is lifted. The total capacitance of all the stacks in the two clamping mechanisms is 17.3 μF. The capacitance of the stacks in the swinger/extender is 5.7 μF. The power consumption of the motor was calculated by adding the total power consumption of the stacks in the swinger/extender and of all the stacks in the clamping mechanisms. The motor efficiency at different loads is plotted against the input frequency in Fig. 4.14. From the figure, the motor efficiency generally increases as the load increases even with the decrease in speed shown previously in Fig. 4.10 due to the increase in load. The piezoelectric stack in the swinger/extender is not only providing the force output but also provides displacement, which is regulated by the voltage input.

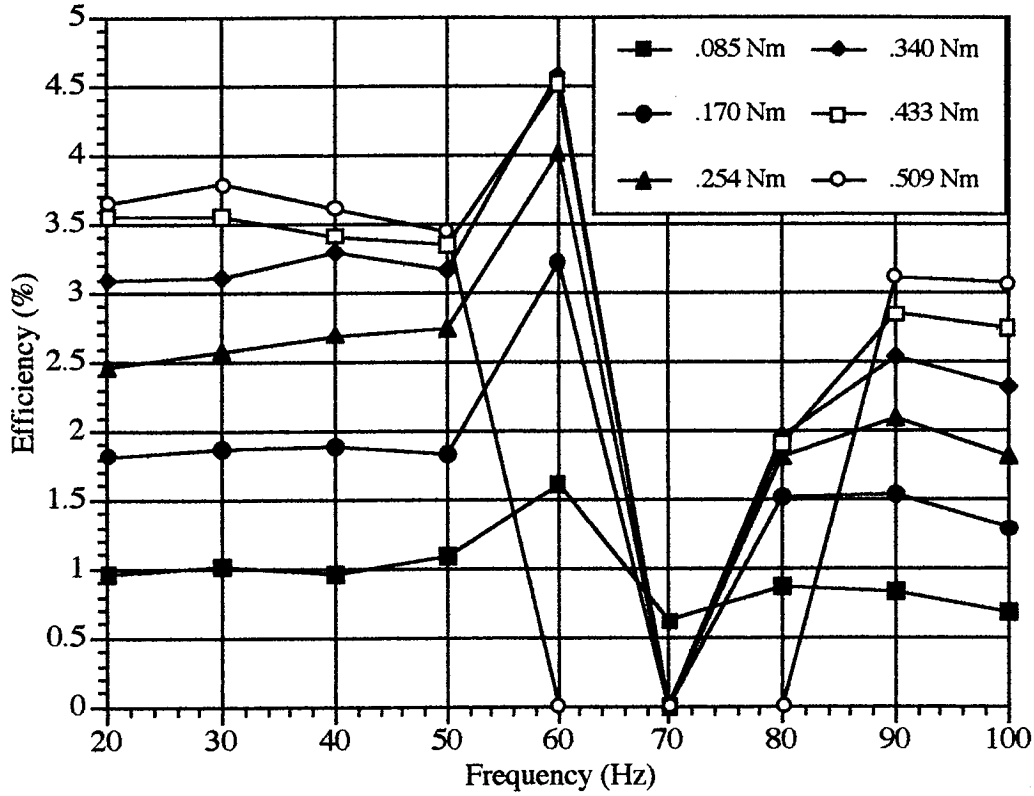

Figure 4.14. Motor efficiency versus frequency at different torque loads.

The external power output of the motor is calculated by the amount of time it takes to lift the hanging weight against gravity a distance of 3 cm. The power output is therefore simply the weight times the velocity. From examination of the stair-case steps from Fig. 4.11, it is observed that the forward step of Region A in Fig. 4.12 is the only portion that positively contributes to the mechanical work output of the motor (provides forward displacement). The horizontal step (clamping portion) does not contributes to the output displacement of the motor. A reduction of 20% in forward step size of Region A (from 7.1×10^{-4} rad to 5.7×10^{-4} rad) is observed when the external load of 0.085 Nm increases five times to 0.433 Nm. This reduction in step size results in slower speed of the motor. However, a 20% reduction in step size does not translate to a 20% reduction in the motor speed. The motor speed at 60 Hz as shown in Fig. 4.11 reduces from 0.1452 rad/s to

0.0814 rad/s; a 44% reduction for the same weight increase. The higher reduction in motor speed is caused by slippage of the motor (Region D in Fig. 4.12) due to inadequate clamping force. This slippage causes the motor to rotate backward which results in lower net rotation in the forward direction for every inchworm cycle. The reduction in motor speed translates into lower power output since there is less work done per unit of time. As for the case of 0.085 Nm load (4.444 N weight), the power output is 0.01229 W and for the 0.433 Nm load (22.22 N weight), the power output is 0.03448 W. The power input to the motor for this case is 0.76377 W. If the slippage in Region D of Fig. 4.12 can be prevented by better clamping action, the speed of the motor at 0.433 Nm load will only decrease by 20% due to the reduction in the step size since there is no slipping backward. The speed is estimated to reduced by 20% to 0.11616 rad/s. The work output will be 0.04917 W and the efficiency of 6.4% can be realized. This might explain why the efficiency increases with the increase in load until the clamping forces (slippage) becomes a deciding factor. Although the clamping action does not directly contribute to the forward stepping of the motor, it is crucial to the inchworm operation. For each load, the efficiency stays nearly constant from 20-50 Hz. In this frequency range, the structures behave quasi-statically. Speed and power consumption increase proportionally with increases in frequency, therefore the efficiency remains constant. The efficiency of the motor peaks out at 60 Hz corresponding to the maximum speed. The efficiency is zero at 70 Hz since there is no work done due to motor stalling. From 80-100 Hz, the efficiency decreases despite the increase in speed as shown previously in Fig. 4.10. At this higher frequency, the force of inertia of the vibrating mass is now much greater than the clamping force, resulting in more slippage and therefore a reduction in efficiency.

CHAPTER V

MODELING OF MOTOR

A dynamic model of the motor and its components was built to better understand its behavior. This dynamic model was also used for the optimization of motor performance. Different driving conditions can be used in the optimization process to drive the motor model without the expense of an actual experiment. From this model, the simulated output performance of the motor can be observed under different input conditions such as waveform and frequencies. The dynamic model of the motor is built using MATLAB SIMULINK. The SIMULINK package in MATLAB is a graphically based tool for modeling dynamic system.

The dynamical governing equations of the motor model will include the modeling of its subcomponents: the clamping mechanisms, the extender/swinger mechanism and the rotor. The motor model is then realized by integration these subcomponents.

Dynamic modeling of the clamping mechanism

The clamping mechanism is a system which consisted of rotating inertias, the lever arms, and elastic hinges, the flexures. In this model, the lever arms are treated as rigid bodies with rotational inertias. The flexure hinges are treated as pure pivot points. The stiffness of the flexures is included in the overall spring constant of the amplification mechanism. A schematic lumped mass representation of the clamping mechanism is illustrated in Fig. 5.1.

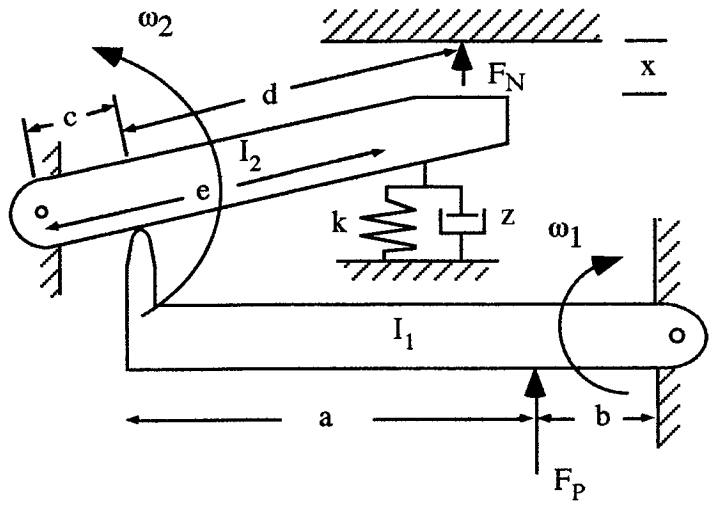

Figure 5.1. Dynamic model of clamping mechanism.

In this figure, F_p is the force exerted by the piezo stack actuator. The constants I_1 and I_2 are the rotational inertias of the first and second lever arms with respect to their points of rotation. K is the spring constant and z is the damping coefficient of the system. The normal force, F_N, is exerted by the contact shoe onto the rotor. The gap, x, is between the contact shoe and the rotor. The angular velocities of the two inertias are ω_1 and ω_2 respectively.

The dynamics of the clamping mechanism can be described with two separate dynamic systems: when in contact and when not in contact. When the contact shoe is not in contact, the dynamic model of the clamping mechanism can be expressed in bond-graph notation as shown in Fig. 5.2.

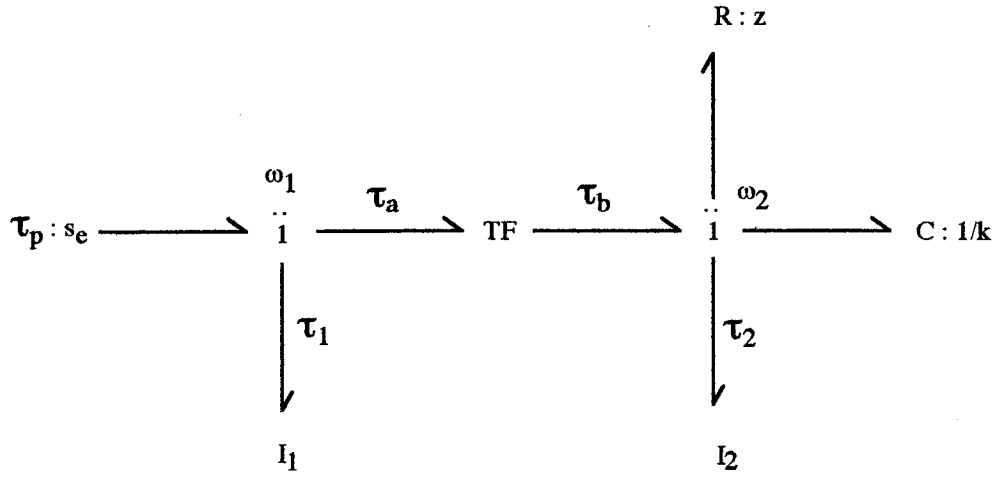

Figure 5.2. Bond diagram of clamping mechanism.

The state variables of the system can be written as

$$X = \begin{bmatrix} \theta_1 \\ \omega_1 \\ \theta_2 \\ \omega_2 \end{bmatrix} \tag{5.1}$$

The input to the system is the torque generated by the stack actuator and is represented by τ_p.

The differential equations for the bond graph are

$$\frac{d\theta_1}{dt} = \omega_1 \qquad \frac{d\theta_2}{dt} = \omega_2; \tag{5.2}$$

$$\frac{d\omega_1}{dt} = \frac{\tau_1}{I_1} \qquad \frac{d\omega_2}{dt} = \frac{\tau_2}{I_2} \tag{5.3}$$

The equation for each junction of the bond-graph is

$$1\ (\omega_1): \tau_p = \tau_A + \tau_i = F_p b \tag{5.4}$$

$$1\ (\omega_2): \tau_B = \tau_2 + \tau_k + \tau_z \tag{5.5}$$

$$C\ (\frac{1}{k}): \tau_k = k\theta_2 e^2 \tag{5.6}$$

$$R\ (y): \tau_z = z\omega_2 \text{ where z is the damping coefficient} \tag{5.7}$$

The equation for the transfer functions in the bondgraph is

$$\tau_A = \left(\frac{a+b}{c}\right)\tau_B \tag{5.8}$$

$$\omega_2 = \omega_1\left(\frac{a+b}{c}\right) \tag{5.9}$$

$$\dot{\omega}_2 = \dot{\omega}_1\left(\frac{a+b}{c}\right) \tag{5.10}$$

The equation of motion for inertia I_1 is

$$\dot{\omega}_1 = \frac{\tau_1}{I_1} = \frac{1}{I_1}(\tau_p - \tau_z) \tag{5.11}$$

The equation of motion for inertia I_2 can be written as

$$\dot{\omega}_2 = \frac{\tau_2}{I_2} = \frac{1}{I_2}(\tau_B - \tau_k - \tau_z) \tag{5.12}$$

$$\dot{\omega}_2 = \frac{1}{I_2}[(\frac{c}{a+b})(\tau_p - \tau_1) - \tau_k - \tau_z] \tag{5.13}$$

$$\dot{\omega}_2 = \frac{1}{I_2}[(\frac{c}{a+b})(F_p b - I_1(\frac{c}{a+b})\dot{\omega}_2) - \tau_k - \tau_z] \tag{5.14}$$

$$\dot{\omega}_2 = \frac{-z\omega_2}{\left[I_2 + I_1\left(\frac{c}{a+b}\right)^2\right]} - \frac{k\theta_2 e^2}{\left[I_2 + I_1\left(\frac{c}{a+b}\right)^2\right]} + \frac{b\left(\frac{c}{a+b}\right)F_p}{\left[I_2 + I_1\left(\frac{c}{a+b}\right)^2\right]} \quad (5.15)$$

The equation of motion for I_2 can be described as a second order equation:

$$\ddot{\theta}_2 + \frac{z}{\left[I_2 + I_1\left(\frac{c}{a+b}\right)^2\right]}\dot{\theta}_2 + \frac{ke^2}{\left[I_2 + I_1\left(\frac{c}{a+b}\right)^2\right]}\theta_2 = \frac{b\left(\frac{c}{a+b}\right)F_p}{\left[I_2 + I_1\left(\frac{c}{a+b}\right)^2\right]} \quad (5.16)$$

The parameters for Equation 5.16 are in Table. 5. 1

Table 5.1. Parameters for equation of motion of clamping mechanism.

Parameter name	Values
a	1.496 in.
b	0.315 in.
c	0.512 in
d	1.3 in.
e	1.3 in.

When the contact shoe of the clamping mechanism extends and starts making contact with the rotor, the motion of the two inertia comes to a sudden stop. Contact is defined when the distance traveled by the contact shoe is equal to the gap G, $\theta_2(c+d) = G$. When in contact, the system dynamics change considerably. Contact is assumed to stop the motion of the two inertia quickly and can be modeled by

$$\ddot{\theta}_2 + 2\pi 10000\dot{\theta}_2 + 500^2\theta_2 = 0 \tag{5.17}$$

These parameters change the equation to a highly damp system to quickly bring the inertia to a stop, thus simulated the sudden stop of the contact shoe. Immediately after contact, the shoes start to exert normal force onto the rotor. The free body diagram of the two lever arms when in contact with the rotor is shown in Fig. 5.3

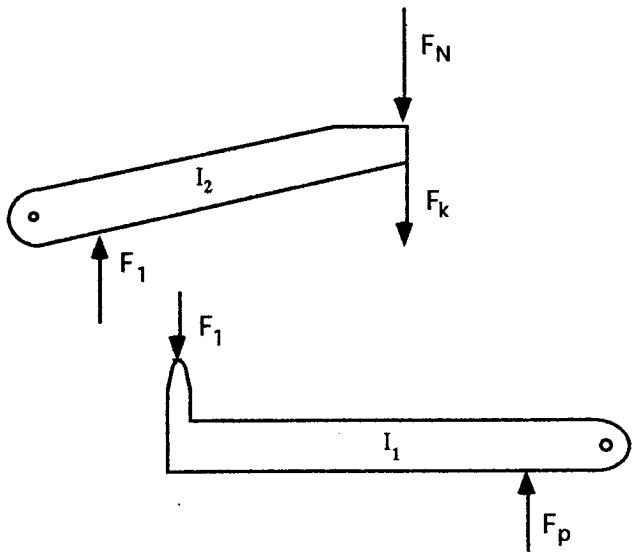

Figure 5.3. Free-body diagram of clamping mechanism components when in contact.

In this figure, F_p is the force exerted by the stack actuator, F_k is the return force of the spring, F_1 is the reaction force between the first and second lever arm and F_N is the normal force between the contact shoe and the rotor. By balancing the moments about each pivot in the free-body diagram, the following equations for the system can be obtained.

$$F_k = kx \tag{5.18}$$

$$F_N(c+d) + F_k e = F_1 c \tag{5.19}$$

$$F_1(a+b) = F_p a \tag{5.20}$$

$$F_n(c+d) = F_1 c - F_k e = F_1 - kxe \tag{5.21}$$

The normal force resulted by the contact of the shoe and the rotor can be described by the follow equation

$$F_N = \frac{bcF_p}{(a+b)(c+d)} - \frac{ke^2\theta_2}{(c+d)} \tag{5.22}$$

Let G be the initial gap between the contact shoe and the rotor. When there is no contact $\{\theta_2(c+d) < G\}$, the force exerted by the actuator is equal to the return force of the spring which results in zero normal force. When there is contact (the displacement of the contact shoe $\{\theta_2(c+d) \geq G\}$, the normal force is the net force between the force exerted by the actuator and the spring returning force.

Review of Coulombic friction force

The block diagram in Figure 5.4 shows the force interaction between the two masses due to the friction forces which exist between the two blocks.

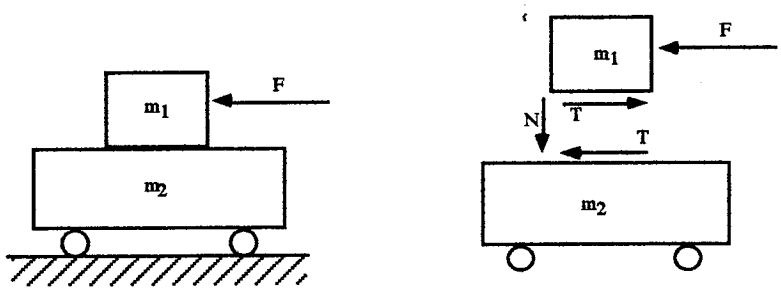

Figure 5.4. Block diagram of Coulombic friction force between two masses.

Let μ_σ be the coefficient of static friction and μ_d be the dynamic coefficient of friction between the two blocks in the diagram. The force F, is the external force acting on the two-block system. The Coulombic friction force, T, acts between the two masses due to the normal force N. This Coulombic friction force is changing according to the condition between the two blocks. If the external force, F, acting on the system is less than $\mu_s N$ then T is equal to F. If the force, F. is greater than $\mu_s N$ then T is equal to $\mu_d N$. In other words, if there is no sliding between the two block, the reaction force T is equal to the external applied force F. If there is slippage between the two blocks, the Coulombic friction force is now equal to the product of the normal force N and the coefficient of dynamic friction μ_d.

Dynamic modeling of the swinger/extender

As in the case of the clamping mechanism, the swinger/extender system consists of rotating inertia, torsional spring and damper. The rotating inertia is treated as rigid body. The flexure hinge of the swinger/extender is treated as pure pivot point. The diagram of the swinger/extender system can be described in Fig. 5.5

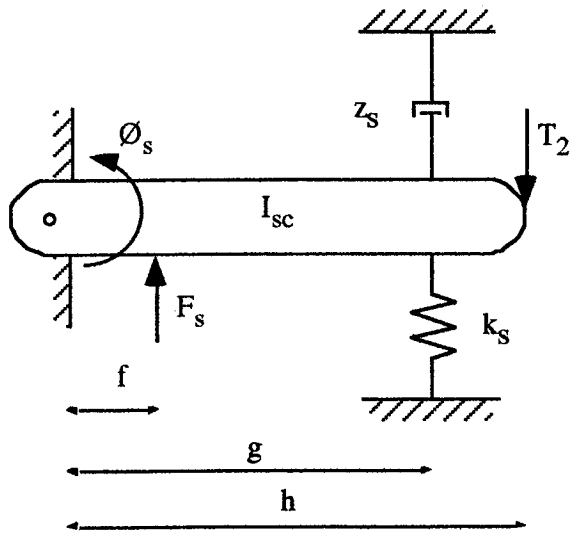

Figure 5.5. Block diagram model of the extender/swinger.

In this figure, I_{sc} is the combined inertia of the extender/swinger arm and the rotating clamping mechanism. The Coulombic friction force, T_2, results from the normal force between the contact shoe of the rotating clamping mechanism and the rotor, as described previously. This reaction is changing depending on the condition between the contact shoes of the rotating mechanism and the rotor. The force, F_s, is exerted by the stack actuator in the swinger/extender mechanism. The parameters, k_s and z_s are the spring constant and damping coefficient of the system respectively.

The values for the moment arm shown in Figure 5.5 are measured as

$f = 0.2$ in

$g = 1.1$ in

$h = 2.05$ in

From Newton's law, the differential equations for the inertia, I_{sc}, are

$$\frac{d\theta_s}{dt} = \omega_s \tag{5.23}$$

$$\frac{d\omega_s}{dt} = \frac{\tau_s}{I_{sc}} \tag{5.24}$$

The torque τ_s can be obtained by balancing the moments

$$\tau_s = \tau_{F_s} - \tau_k - \tau_z - \tau_{T_2} \tag{5.25}$$

$$\tau_{T_2} = T_2 h \tag{5.26}$$

$$\tau_z = zg^2\dot{\theta}_s \tag{5.27}$$

$$\tau_k = kg^2\theta_s \tag{5.28}$$

$$\tau_{F_s} = F_s f \tag{5.29}$$

$$\frac{d\omega_s}{dt} = \frac{1}{I_{sc}}\left[F_s f - kg^2\theta_s - zg^2\dot{\theta}_s - T_2 h\right] \tag{5.30}$$

The equation of motion for the swinger can be written in state space form as

$$\frac{d}{dt}\begin{bmatrix}\theta_s \\ \omega_s\end{bmatrix} = \begin{bmatrix} 0 & 1 \\ -\frac{kg^2}{I_{sc}} & -\frac{zg^2}{I_{sc}}\end{bmatrix}\begin{bmatrix}\theta_s \\ \omega_s\end{bmatrix} + \begin{bmatrix} 0 \\ \frac{F_s f - T_2 h}{I_{sc}}\end{bmatrix} \tag{5.31}$$

Since T_2 is the friction force resulted from the normal force between the contact shoe and the rotor, T_2 varies depending on the relative motion between the swinger/extender and the rotor. If there is slippage between the rotor and the rotating clamping mechanism, $\left|\dot{\theta}_s - \dot{\theta}_r\right| > 0$, then

$$T_2 = -\operatorname{sign}\left(\dot{\theta}_r - \dot{\theta}_s\right)\mu N_2 \tag{5.32}$$

If there is no slippage, $\left|\dot{\theta}_s - \dot{\theta}_r\right| = 0$

$$T_2 = \frac{I_r \ddot{\theta}_s}{h} + L + T_1 \tag{5.33}$$

In Eq.(5.33), L is the external load on the rotor. The condition for the case of no slippage has the same effect as adding the rotor inertia into the equation of motion of the swinger/extender when the rotor is locked together with the extender/swinger mechanism.

$$(I_r + I_{sc})\ddot{\theta}_r + zg^2\dot{\theta}_r + kg^2\theta_r = F_s \cdot f - Lh - T_1 h \tag{5.34}$$

Modeling of rotor

The rotor is modeled as a rotating inertia. The diagram of the rotor and the forces acting on it is shown in Figure 5.6

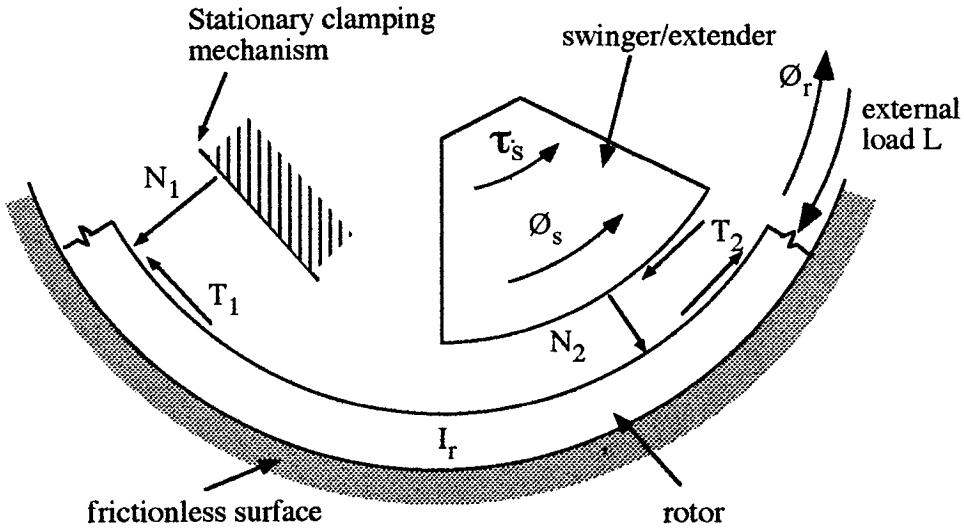

Figure 5.6. Rotor dynamic model.

In Fig. 5.6, I_r is the rotational inertia of the rotor. The forces, T_1 and T_2, are the Coulombic friction forces which result from the normal forces, N_1 and N_2. They are generated by the stationary clamping mechanism and the rotating clamping mechanism. The equation of motion for the rotor is

$$I_r\ddot{\theta}_r + c_r\dot{\theta}_r = \tau_{T_2} - \tau_{T_1} - \tau_L \tag{5.35}$$

with $\tau_{T_1} = T_1 h$, $\tau_{T_2} = T_2 h$ and c_r is the rotational damping coefficient of the rotor.

As mentioned before, the values of the reaction forces T_1 and T_2 vary depending on the conditions between the rotating clamping mechanism and the rotor. T_1 is the friction force between the stationary clamp (ground) and the rotor I_r and varies accordingly:

- If the rotor is moving, the total net force acting on the rotor is greater than the maximum allowable friction force, then

$$T_1 = -\text{sign}(\dot{\theta}_r)\mu N_1 \tag{5.36}$$

- If the total net force acting on the rotor is less than the maximum friction force, then T_1 is equal to the net force acting on the rotor.

$$T_1 = -T_2 + L \tag{5.37}$$

In other words

- If there is slippage between the stationary clamp and the rotor, $|\dot{\theta}_r| > 0$, then

$$T_1 = -\text{sign}(\dot{\theta}_r)\mu N_1 \quad \text{or} \quad \tau_{T_1} = -h \cdot \text{sign}(\dot{\theta}_r)\mu N_1 \tag{5.38}$$

- If there is no slippage, ($\dot{\theta}_r = 0$), then T_1 is equal to the combined remaining forces acting on I_r

$$T_1 = -T_2 + L \qquad \text{or} \qquad \tau_{T_1} = -\tau_{T_2} + L \cdot h \tag{5.39}$$

T_2 is the frictional force between the rotating clamping mechanism, I_{sc}, and the rotor, I_r. This friction force, T_2, is the same as in the swinger/extender section but is opposite in direction.

Model verification

Using the above equations for each segment of the motor, the motor model was built using MATLAB SIMULINK to simulate the dynamic response of the motor. The SIMULINK model of the motor can be seen in Appendix B. The response of the dynamic model was compared to the actual response of the motor for verification. Shows in Figures 5.7-5.9a & b are the comparisons of the simulated inchworm step outputs of the motor model at selected frequencies for the no-load cases with experimental data output from the motor. From these figures, the speeds of the motor at three different frequencies (30 Hz, 60 Hz, and 75 Hz) produced by the model closely match the experimentally measured speed. The step profiles of the motor are also matched by the model. At 30 Hz, the staircase steps profile produced by the model exhibits no slippage just like the actual profile. At 60 and 75 Hz, the model produced the inchworm steps with slippage that are seen in the actual measurements. Figures 5.10-5.12a & b compare the simulated step profiles of the model with the actual step profiles of the motor under load. The speeds under load at different frequencies are matched by the model. The apparent slippage of the motor under load at 60 Hz is also produced by the model. The only differences between the simulated step and the actual step are the noise and fluctuation in the actual data. The

different is caused by noise in the measurement and mostly by the variations in the rotor's tolerance. The variation in tolerance creates "bad spot" in the rotor which effects the step profile. This effect can be seen in Fig. 5.11b. Although less apparent, the influence by this "bad spot" on the step profile can also be seen at other different frequencies.

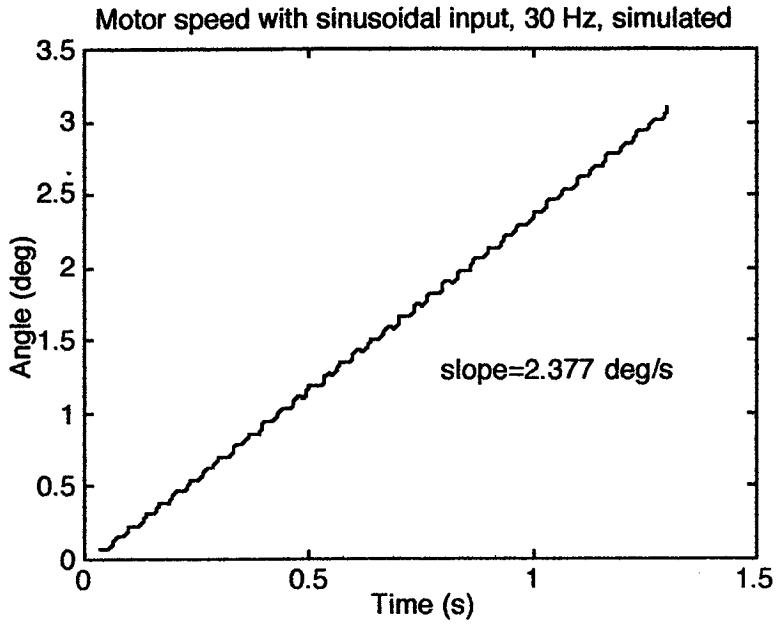

a) Simulated.

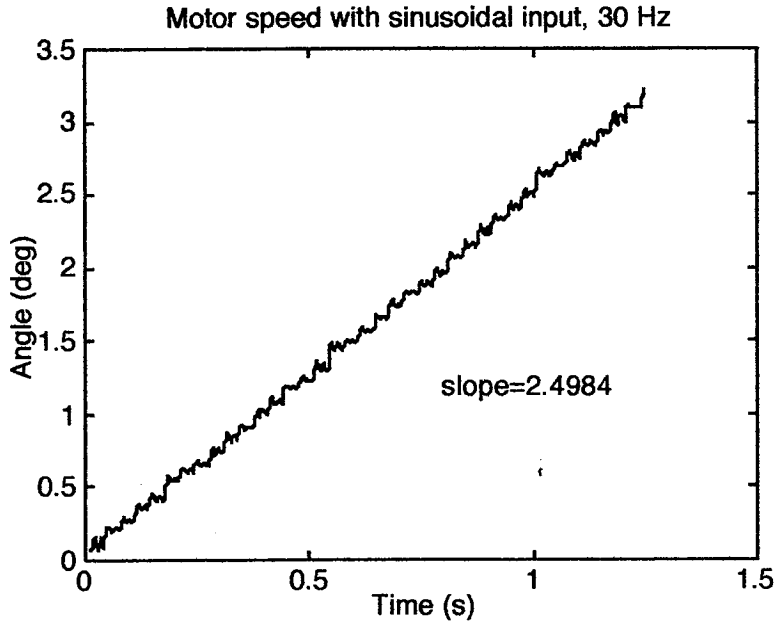

b) Actual.

Figure 5.7. Motor step profile at 30 Hz frequency.

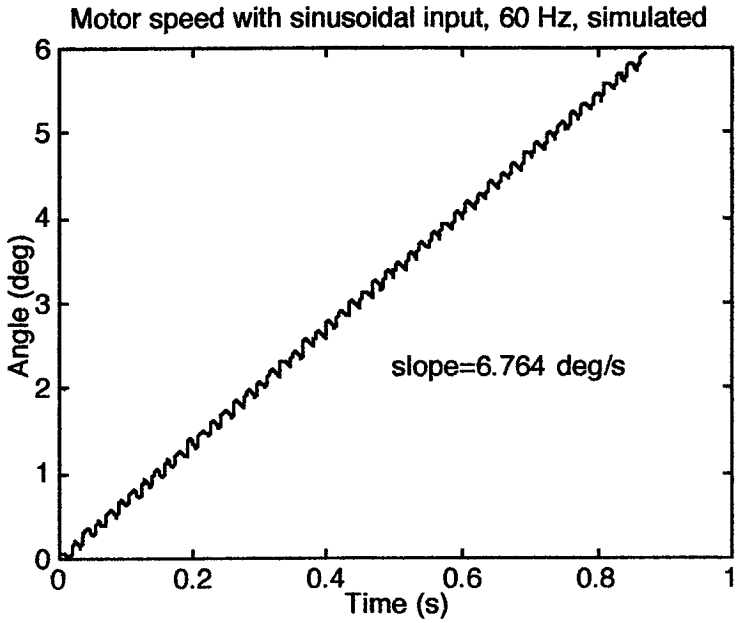

a) Simulated.

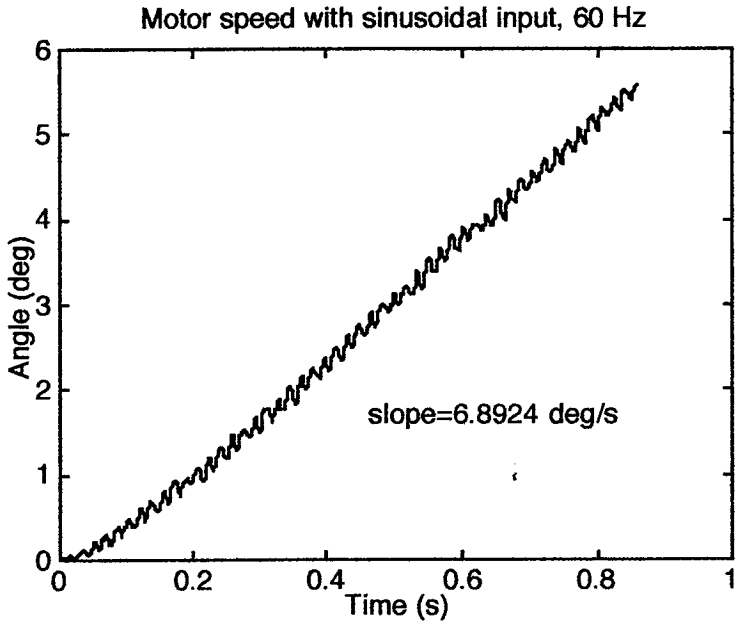

b) Actual.

Figure 5.8. Motor step profile at 60 Hz frequency.

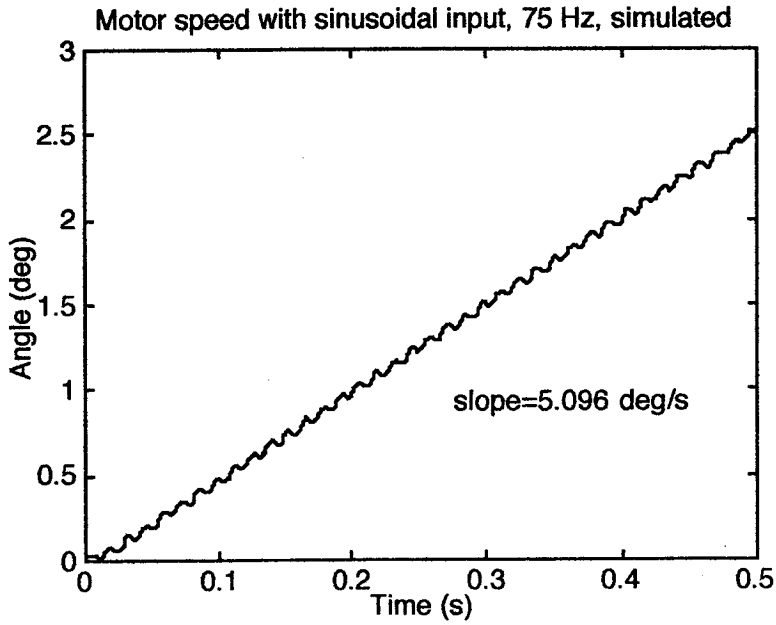

a) Simulated.

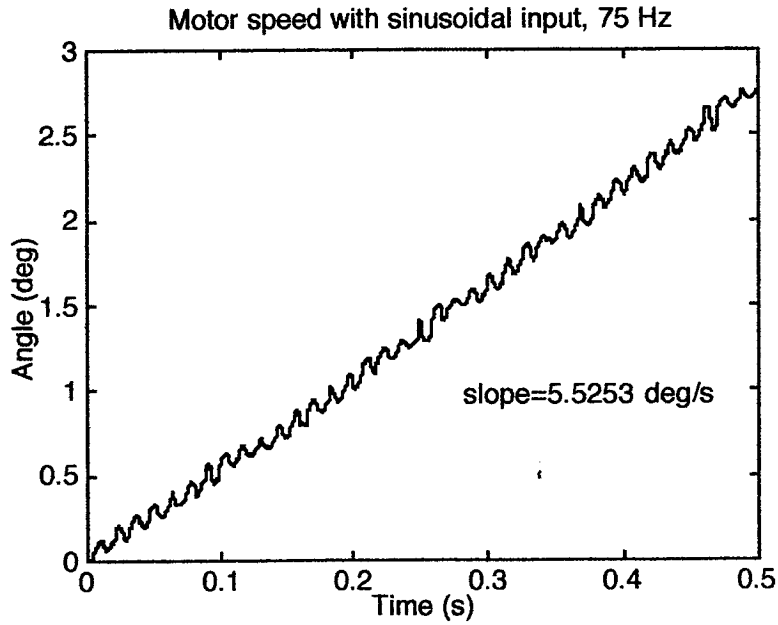

b) Actual

Figure 5.9. Motor step profile at 75 Hz frequency.

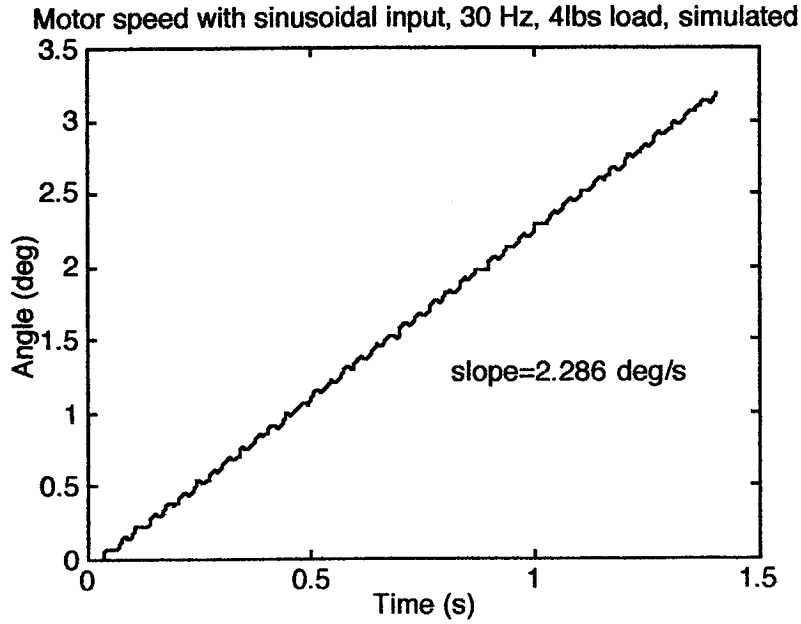

a) Simulated.

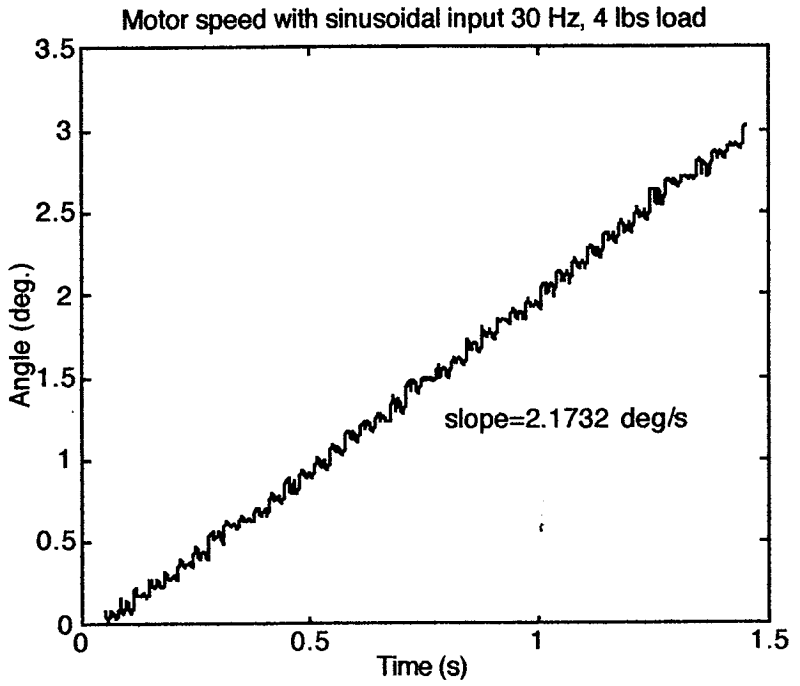

b) Actual.

Figure 5.10. Motor step profile under load at 30 Hz frequency.

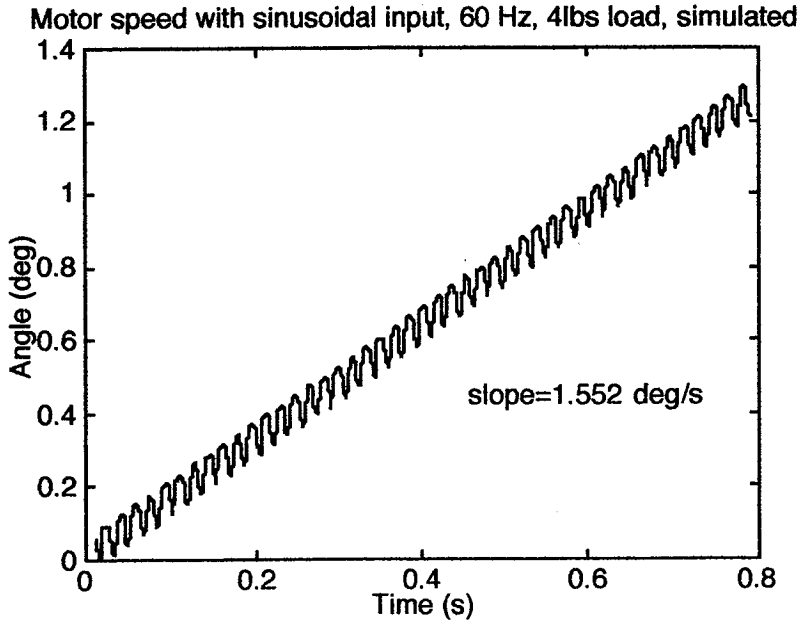

a) Simulated

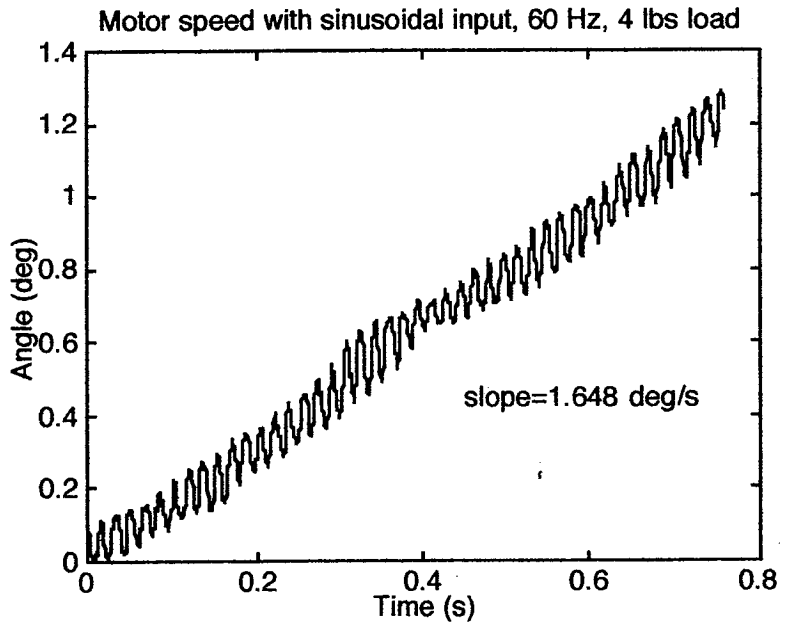

b) Actual.

Figure 5.11. Motor step profile under load at 60 Hz frequency

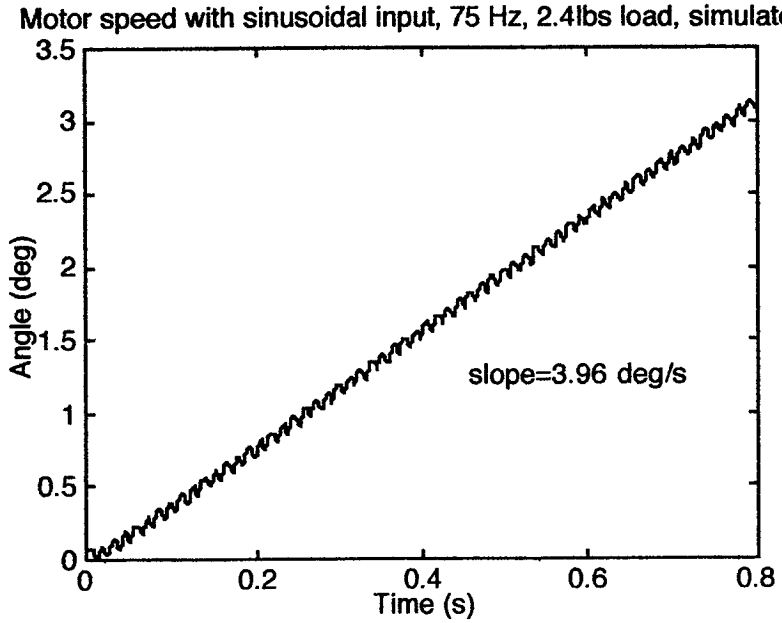

a) Simulated.

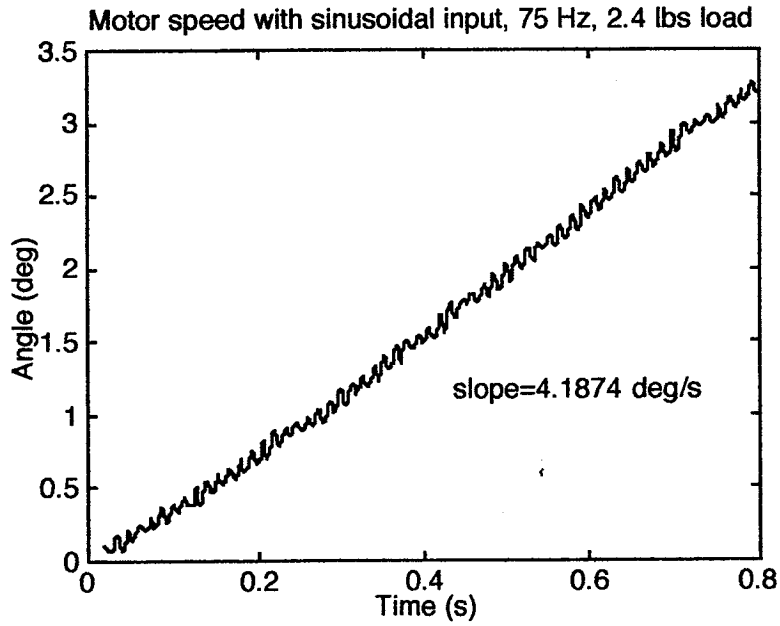

b) Actual.

Figure 5.12. Motor step profile under load at 75 Hz frequency.

CHAPTER VI

OPTIMIZATION OF MOTOR PERFORMANCE

Motivation

For most if not all of the inchworm motors built to date, three signals are used to drive the motors. The desired driving signal is to use three 90° out of phase square waves. Most people use three 90° out of phase sinusoidal signals instead of square waves to drive their motors because sine waves are easier to generate. Square waves are hard to implement because of their higher harmonic frequencies. These higher harmonics require tremendous power and high bandwidth from the amplifiers especially when high capacitive actuators are used. The driving signal for the inchworm motor as commonly seen in the Burleigh Patent and various other inchworm motors is to use two square waves 180° out of phase with each other and a triangular wave with 90° out of phase with the clamping signal as shown in Fig. 6.1 [55, 72, 73, 76, 77]. Other commonly used driving signals are to use three sine waves or triangular waves with 90° out of phase relative to each other also shown in Fig. 6.1 [57, 78].

By using these waveforms, the phase relations of the clamping actuators and the displacement of the extender/swinger are assumed to be the same as the phase differences of the driving signals. The researchers, in turn, neglect the dynamics of the motor actuators and sub-structures. The exact operating sequence of each motor component might not have a 90° phase difference; therefore the performance of the motor is affected. This is dramatic if the motor is operated beyond the quasi-static range.

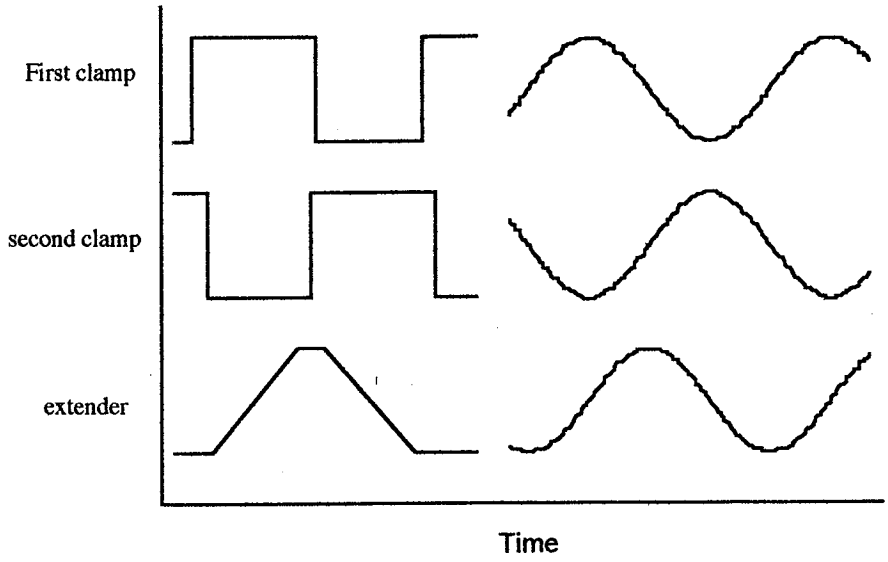

Figure 6.1. Typical driving signals for inchworm motor

Most inchworm motors seen in literature exhibit the same displacement profile as shown previously in Fig. 5.11. The stair-case steps of the displacement in this figure are typically produced by an inchworm motor using symmetric driving signals. These displacement profiles can be seen from other motor designs such as Goto et al., Ohnishi et al., Tojo et al., and Pandell [57, 60, 72, 73, 79]. A close examination of the displacement profile shows reduction in step size as expected when the load increases. However, slippage is the main cause for the reduction in speed in addition to the reduction in step size. This slippage happens when the motor operates at higher frequencies or when under heavy load. At higher operating frequencies, the inertia becomes larger and slippage also occurs just like in an inertia stepper motor but with negative effect. This slippage is referred to as "glitch" in the Burleigh motor and it is an undesirable effect in high resolution positioning applications. Duong and Garcia (1996) were the first to give a detailed explanation of the displacement profile. The detail of the motor step is shown in Fig. 4.12 and is repeated here in Fig. 6.2 for convenience.

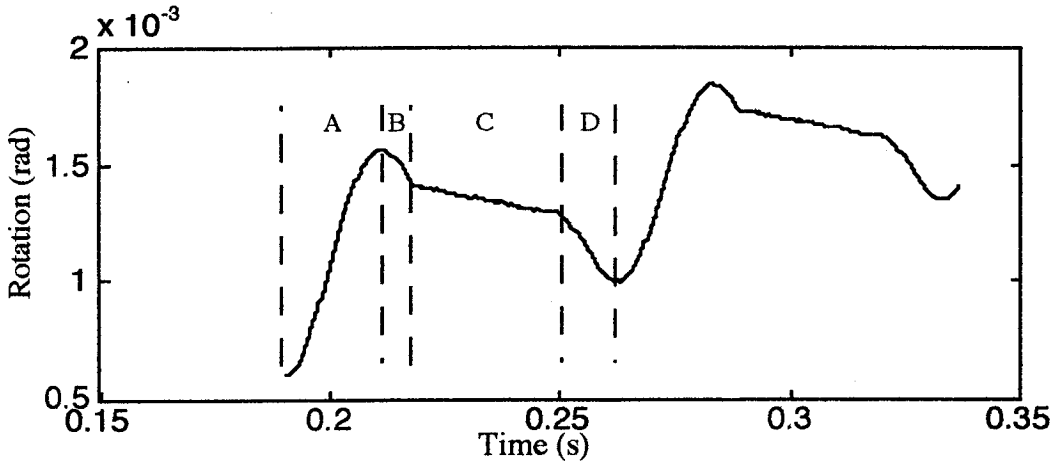

Figure 6.2. Detail step of motor.

It is observed that the forward step of Region A in Fig. 6.3 is the only portion that positively contributes to the mechanical work output of the motor, i.e. it provides the forward displacement. The horizontal step occuring in Region B and C (clamping portion) does not contribute to the output displacement of the motor. The slippage in these two regions shown here is the extreme case where slippage happens during the clamping portion, otherwise region B and C are flat. Commonly, the slippage of the motor (Region D in Fig. 6.3) is the main cause for the reduction in speed of the motor when there is no slippage in Region B or C. This slippage causes the motor to rotate backward which results in lower net forward rotation for every inchworm cycle. Therefore, this reduces the speed of the motor. The reduction in motor speed also translates into lower motor efficiency as analyzed in Chapter IV.

The input waveform and phase relation between driving signals is suspected to be responsible for the slippage. As seen from the step, slippage does not occur on the forward step (Region A) which carries the largest load (the external load itself and the inertia due to acceleration) but rather occurs during the holding step, Region B and C. This indicates that the motor is capable of pushing the external load but is deficient in holding it. Most driving signals utilize three input waveforms 90° out of phase with respect to each

other while neglecting the dynamic interaction of the motor itself. The actual phase relation between the clamping force and the extender might not be 90° which leads to slippage since the motor is now operating out of sequence. In addition, the change in inertia from the forward stroke to the returning stroke also contributes to time varying loads during the cycle which can increase dynamic uncertainty.

The goal of this investigation is to find the optimum driving waveform for each section of the motor that will lead to significant improvement in the speed of the motor. The optimization will also find the optimum waveforms to increase the speed of the motor under load. This will inturn, increase the dynamic torque output and power of the motor. As a baseline for comparison, the commonly used waveforms, sinusoidal and square waves, will also be used to drive the motor. The improvement in motor's performance can be realized by simply changing the input waveform with the optimized one without adding any additional hardware or complexity into the device. Precision may also improve since slippage may be reduced or eliminated.

The performance of the motor testbed will be experimentally assessed once the optimum waveforms are determined and compared to the performance when driving with sinusoidal waveforms.

Optimization

Many methods of performing optimization have been extensively studied. For some problems, the optimization can be solved analytically using a calculus approach. In this method, a local optima is found by solving a set of zero-gradient equations of the cost function. Using this method, the derivative of the cost function must exist and the search is limited to those points whose slope is zero in all directions. The zero-order methods are the simplest optimization algorithm. These methods require only function values in searching for the optimum (Vanderplaats,1984) [80]. One of the most powerful zero-order methods is the exhaustive search in which the design space is completely searched. The cost

function is evaluated with all possible variable combinations and the best solution is seeked out. Surface mapping is a form of this method. However, if a large design space is to be evaluated, the number of function evaluation grow exponentially. The problem becomes computational intensive and might be impossible to complete. This method is inefficient and only suitable for a small number of variables. Random search is also the most inefficient method. In this method, a set of variables is selected randomly throughout the design space. The function is evaluated and compared to the previous value and the best solution is kept. This method is easy to implement and requires little computer storage. Powell's method is the most popular of the zero-order method. This method is based on the concept of conjugate directions. The basic concept is first to search in n orthogonal direction. A new search direction is created by connecting the first and last design points. The principle behind this concept is that, if a quadratic function is given, this function will be minimized in n or fewer conjugate search direction. There are some drawbacks with Powell's method. The search directions tend to become parallel because of numerical imprecision or because of the nonquadratic nature of the cost function. If the search direction gains no improvement, the subsequent search direction will not be conjugate.

There are many other zero-order search methods similar to Powell's method in which new search direction is based on information on previous search directions. The first-order methods utilize gradient information and are more efficient than zero-order method. Gradient information must be supplied analytically or by finite-difference computations. The three basic first-order approaches are: steepest-descent, conjugate-directions, and variable-metric methods. For steepest descent method, the search direction is taken as the negative of the gradient of the objective function. The convergence rate of this method is very poor because it does not utilize information from previous iterations. The conjugate-direction (Fletcher-Reeves) method is a modified steepest descent algorithm which improves the convergence rate. The initial search is accomplished using the steepest descent direction. On subsequent iterations, the search direction is conjugate based on

information of previous iterations similar to Powell's method except each search direction is conjugate.

The variable metric method also utilizes information on previous iterations but stores them in an n dimension array instead of a single scalar in Fletcher-Reeves method. The variable metric methods are efficient and reliable. The two most popular variable metric methods are the Broydon-Fletcher-Goldfarb-Shanno (BFGS) and the Davidon-Fletcher-Powell (DFP) methods (Vanderplaats, 1984). The second-order methods are the most efficient methods. Newton's method begins with the second-order Taylor series expansion of the cost function. The method utilizes not only the function values and gradient information but the second-derivative matrix as well. If the function being minimized is a true quadratic in the design variables, the search direction will provide the solution in only one iteration. Newton's method is always the preferred approach if the matrix of second derivative can be calculated. There are also other heuristic methods in optimization such as genetic algorithm, simulated annealing, and neural network.

Motor optimization

The routine used for the waveform optimization is from the MATLAB Optimization Toolbox [81]. The MATLAB function CONSTR was used. This MATLAB function uses Sequential Quadratic Programming (SQP) method. In this method, a Quadratic Programming subproblem is solved at each iteration using an active set strategy similar to that described by Gill, Murray and Wright (1981)[82]. It finds an initial feasible solution by first solving a linear programming problem. An estimate of the Hessian of the Lagrangian is updated at each iteration using the Broydon-Fletcher-Goldfarb-Shanno formula. A line search is performed using a merit function similar to that proposed by Han (1977) and Powell (1978,1978)[83-85]. The MATLAB function, CONSTR, finds the constrained minima of a function of several variables, starting at an initial estimate and is

generally referred to as constrained non-linear optimization. The problem can be mathematically stated as follow:

$$\text{minimize } f(\mathbf{X}) \qquad \text{subject to : } \mathbf{G}(\mathbf{X}) \leq 0$$

Most optimization problems benefit from good starting guesses at the solution. This initial starting location improves the execution efficiency and helps locate the global minimum instead of being stuck at local minimum.

The waveform optimization problem was solved using an evolutionary approach. In this approach, a problem with a smaller number of variables is solved first. The solution from this lower order is then used as starting location for a higher order problem.

The objective function used for the waveform optimization is the motor model implemented in MATLAB SIMULINK. Using this model, a set of waveforms is used to drive the model and the motor step displacement is produced. Therefore, the waveform are the variables in the design space for the optimization. The objective of the optimization is to obtain a set of waveforms that produce the best output performance (e.g. speed and torque). The motor speed evaluated by the motor model is the value to be optimized.

The waveform optimization was carried out at three selected frequencies: 30, 60 and 75 Hertz. From the preliminary performance assessment of the motor in Chapter IV, the 60 Hz frequency is the resonance frequency of the motor. This frequency was chosen first because at resonance frequency, the motor operation is mostly influenced by the dynamics of its sub-structures. The waveform optimization at this frequency may compensate for the dynamic interaction within the motor sub-structures and improve its performance. The 30 Hz operating frequency is in the quasi-static range. This frequency was chosen to see if the waveform optimization can also improve the performance of the motor even when operated quasi-statically (i.e. less dynamic interaction involved). The 75 Hz operating frequency is beyond the resonance frequency. Although operated at higher frequency, the speed of the

motor at 75 Hz in the preliminary assessment is slower than at 60 Hz. This reduction in performance is believed to be caused by the change in phase relation of the sub-structures of the motor (beyond the resonance frequency) when compared to the phase relation of the input signals. The waveform optimization may compensate for this phase change and improve the performance at this particular frequency.

The motor requires a set of three different input waveforms to operate. In the waveform optimization at the selected frequency, each waveform period is divided into many partitions. The magnitude of the waveform in each partition may varies. The waveform is obtained by connecting the value in each partition as shown in Figure 6.3.

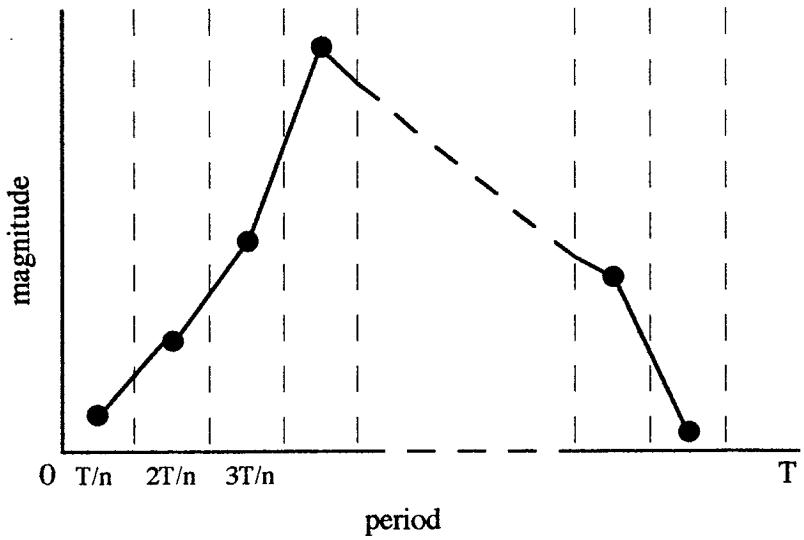

Figure 6.3. Partitioning of waveform.

The waveform can have any shape which depends on the magnitude in each partition within the waveform period. By dividing the period of the waveform into several partitions, each partition of the waveform becomes a variable. The number of variable increases as the number of partitions increases and the waveform becomes smoother. This is the same as the sampling rate in capturing a waveform. However, by increasing the number partitions, the number of variables also increases. This can become a burden because the number of

function evaluation can increase tremendously as the number of variable increases in optimization. With three different waveforms, the total number of variable is three times the number of partition.

The constraints imposed on the variables is represented by the physical limitation of the piezoelectric actuators. The piezoelectric actuators used in the motor can only withstand an electrical input from -45 V to 200 V. In driving the motor, an input range of 0-200 V is used to drive the actuators. This operating range will be used as constraints to the variables so that their values will always stay in this range.

The optimization was run on a Silicon Graphic Indigo^2 xZ work station with a CPU clock speed of 160 MHz. All the MATLAB programs including the motor model in SIMULINK were translated into C programming language before execution to increase the computing speed. Executing time for each function evaluation of the motor model is approximately one to four minutes depending on the waveform frequency (length of running time required to produce enough number of motor displacement step). The MATLAB function CONSTR was modified so that the value of the objective function and the variables can be obtained and monitored after each iteration. Two MATLAB M-files are used in conjunction with CONSTR. A separate M-file states the initial conditions, tolerance and convergence criteria. A second M-file calls and evaluates the objective function (motor model) and imposes constraints on the variables. This file uses the variable values supplied by the optimization routine CONSTR, calls the MATLAB SIMULINK motor model, evaluates the model, and returns the output value. These codes is given in Appendix B.

The optimization was initially performed using five partitions for each waveform. With the evolutionary approach, the number of partitions is then increased to nine. The result from the five partitions per waveform optimization is used as the new starting location. The values of the starting location for the case of nine partitions are obtained by interpolating the results of the five partitions. The result of the nine variable optimization is

then interpolated and use as a starting location for optimization with seventeen partitions for each waveform. The total number of variables to be optimized in this case is fifty one. By using the evolutionary approach, the optimization with lower number of variable will quickly put the objective function in the vicinity of minimum in the search space. The increase in the number of variable will refine the search to achieve the minimum.

The results from the five variables optimization can be seen in Figure 6.4 a, b, c, d. Figure 6.4a shows the starting waveform. The legends in Figure 6.4a are: M clamp (moving clamping mechanism), S clamp (stationary clamping mechanism), and extender (swinger). This starting location (waveform) for the five partitions (fifteen variables for a set of three waveforms) optimization is chosen by dividing a sinusoidal signal into five partitions. The value in each partition is used as the starting location. The waveform did converge and a minimum is found. The optimized waveform set is shown in Figure 6.4b. The optimization progress is shown in Figure 6.4c. In this figure, the value of the objective function (cost function) is plotted against the number of iterations. It took about 830 iterations for the optimization to converge to this minimum. The executing time is approximately 17 hours for this particular run. The motor performance before and after optimization is shown in Figure 6.4d. As shown from the figure, the optimization indeed produces a set of input waveform that improves the speed of the motor. The optimized waveforms exhibit non-symmetrical shape when compared with the starting waveforms. This non-symmetrical shape is to accommodate the time variance in the dynamic of the system. The waveform for the clamping mechanism has a longer holding period at maximum voltage to prevent slippage.

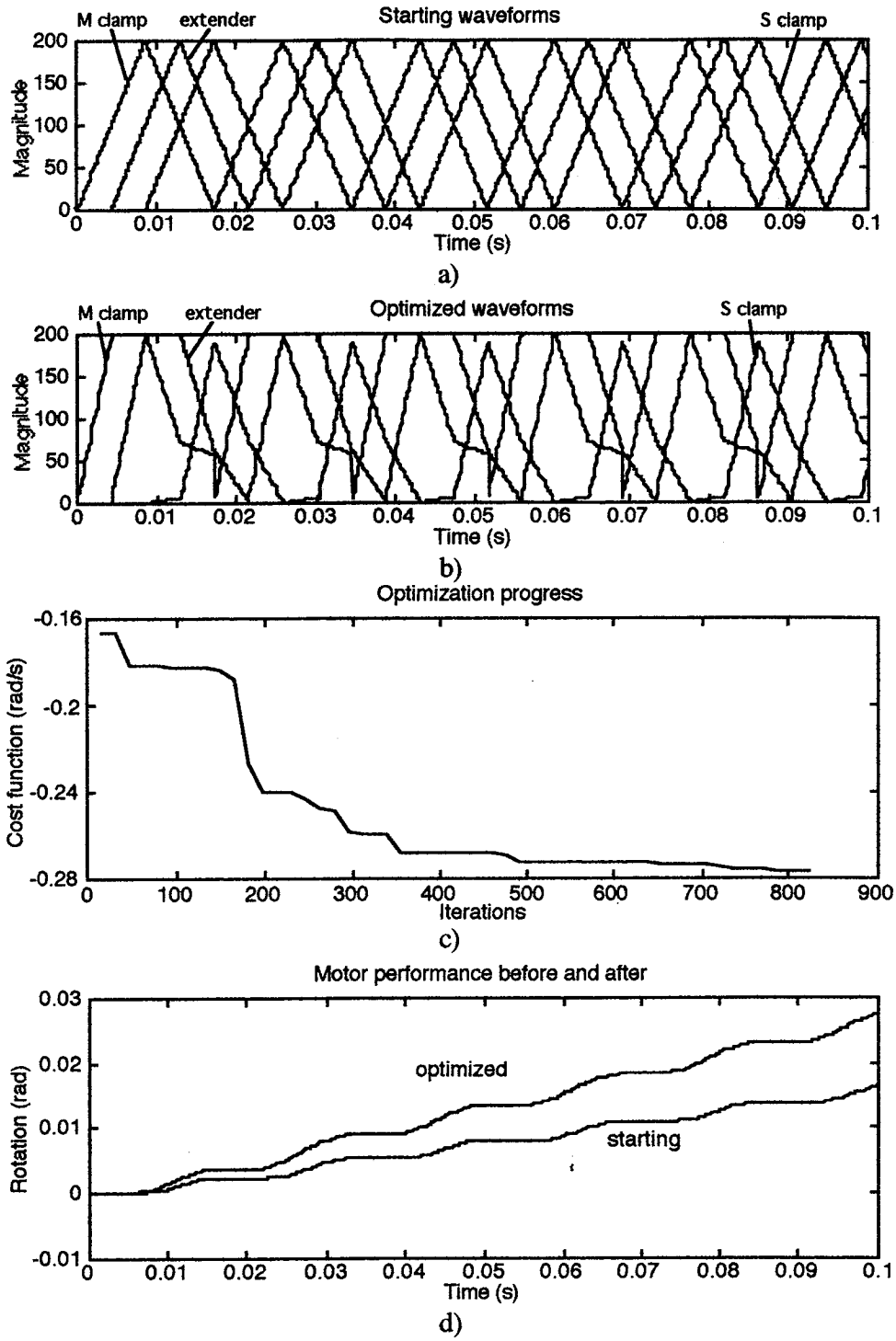

Figure 6.4. Optimization with five partitions: a) starting waveform, b) Optimized waveform, c) Optimization progress, d) Performance before and after optimization.

The optimized waveforms shown in Figure 6.4b is used as the starting location for the optimization with nine partitions. The values of the five partitions are interpolated to obtain nine values for the nine partitions. Figure 6.5 a, b, c, d shows the result from optimizing the motor with nine partitions of each waveform period. As shown in the figure, the increase in the number of partitions from five to nine improves the results (further reducing the cost function). The increase in the number of partitions increases the fidelity of the waveform. This allows the waveform with nine partitions to be able to present a more complex shape which required by the optimization to further reduce the cost function. The tolerances and convergence criterias are kept the same for all cases.

The result from the optimization of the waveform using nine partitions is again interpolated and used as the starting location for the case with seventeen partitions. The optimization results for the seventeen partition case is shown in Figure 6.6 a, b, c, d. As seen from the figure, there is not much improvement when increasing the number of partition from nine to seventeen (twenty seven to fifty one variables total). The number of iterations to reach convergence is 2500. This is approximately over fifty hours of computer CPU time. The improvement from increasing the number of variables is not worth the burden of the increase in executing time. It is important to note that when the number of variables in the optimization increases (introducing more variables into the optimization), the search space is further refined but does not change. The overall shape of the resulted waveform does not change significantly. The increase in the number of variables only enhances the resolution of the waveform and enable it to express a more precise wave shape.

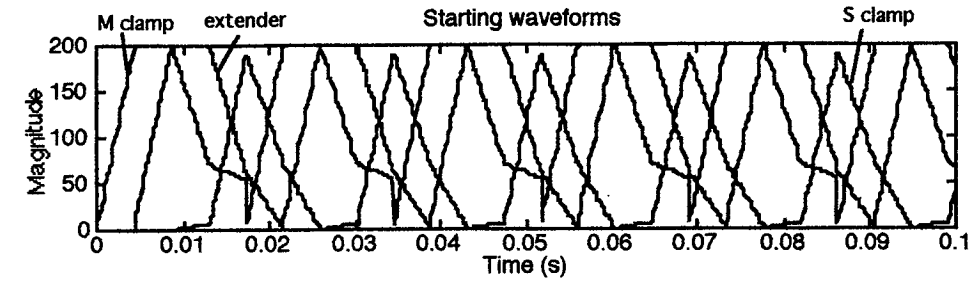

a)

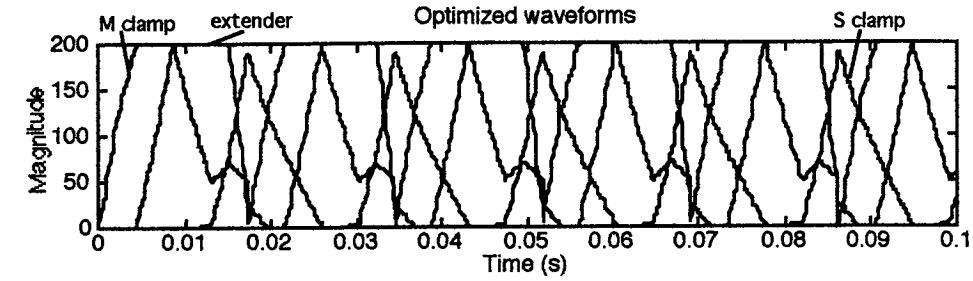

b)

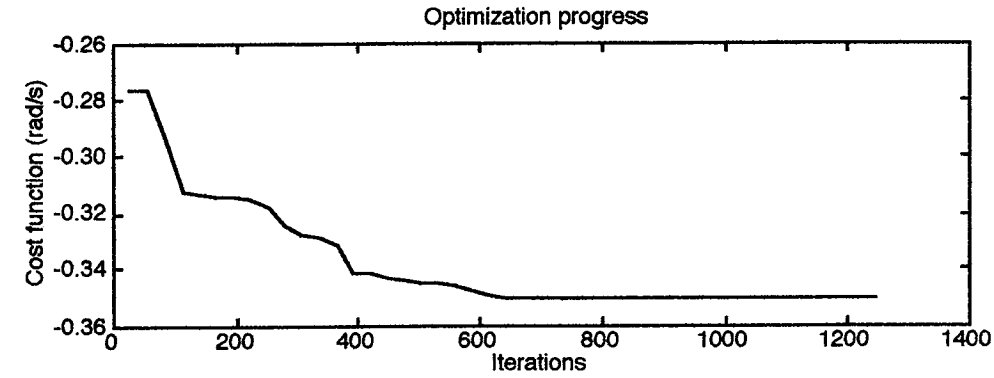

c)

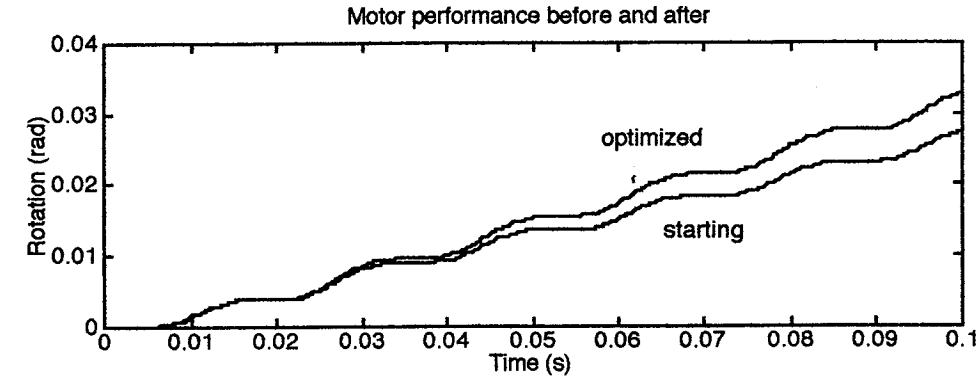

d)

Figure 6.5. Optimization with nine partitions: a) starting waveform, b) Optimized waveform, c) Optimization progress, d) Performance before and after optimization.

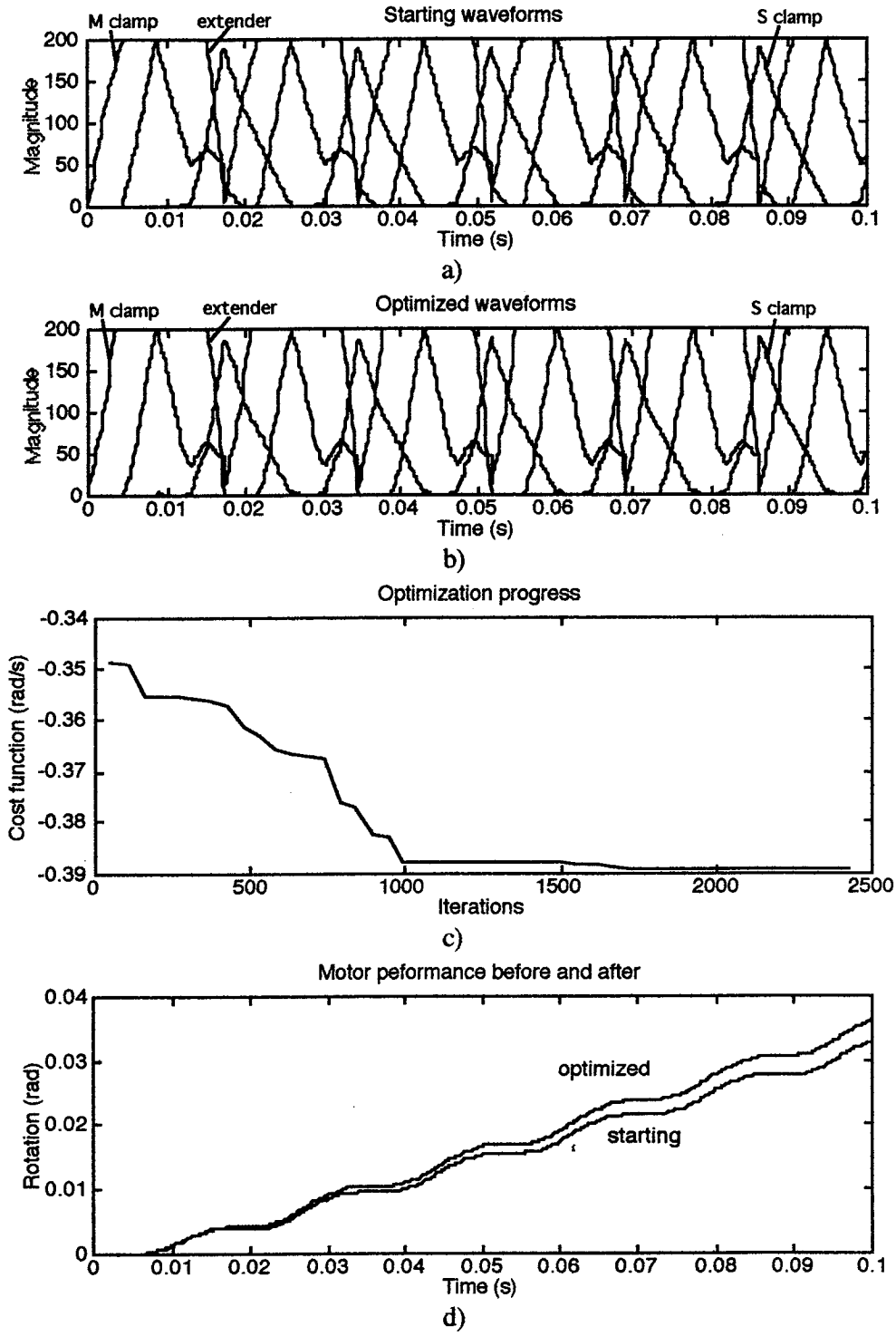

Figure 6.6. Optimization with seventeen partitions: a) starting waveform, b) Optimized waveform, c) Optimization progress, d) Performance before and after optimization.

The optimization was performed using different starting location to test if the cost function converges to approximately the same minimum using five partitions for these different starting waveforms. Figure 6.7 shows the optimization with a randomly generate waveform for the starting location. From the figure, the motor could barely operate in the beginning with the randomly generated waveform. The optimization successfully converged and produced a set of waveform that increases the speed of the motor. Figure 6.8 shows the optimization using a set of square waves as the starting location similar to the driving signal used by Burleigh. It took about half of the running time to successfully converge when compare with the random starting location. This is because the starting square waves is already much closer to the minimum than the random starting waveform. Figure 6.9 shows the optimization with a different set of starting waveforms. This starting set of waveforms utilizes two square waves for the clamping mechanism and a triangle wave for the swinger/extender mechanism. Again, the optimization successfully converged. From the results using different starting locations, although the optimized waveforms are not exactly the same for different starting location, the overall shapes show similarity between the optimized waveforms. These differences are due to the coarse resolution in the waveform (with five partitions). The minimum might not be a deep point but a small flat valley. This is an indication that the optimization successfully converged to approximately the same global minimum from different starting locations.

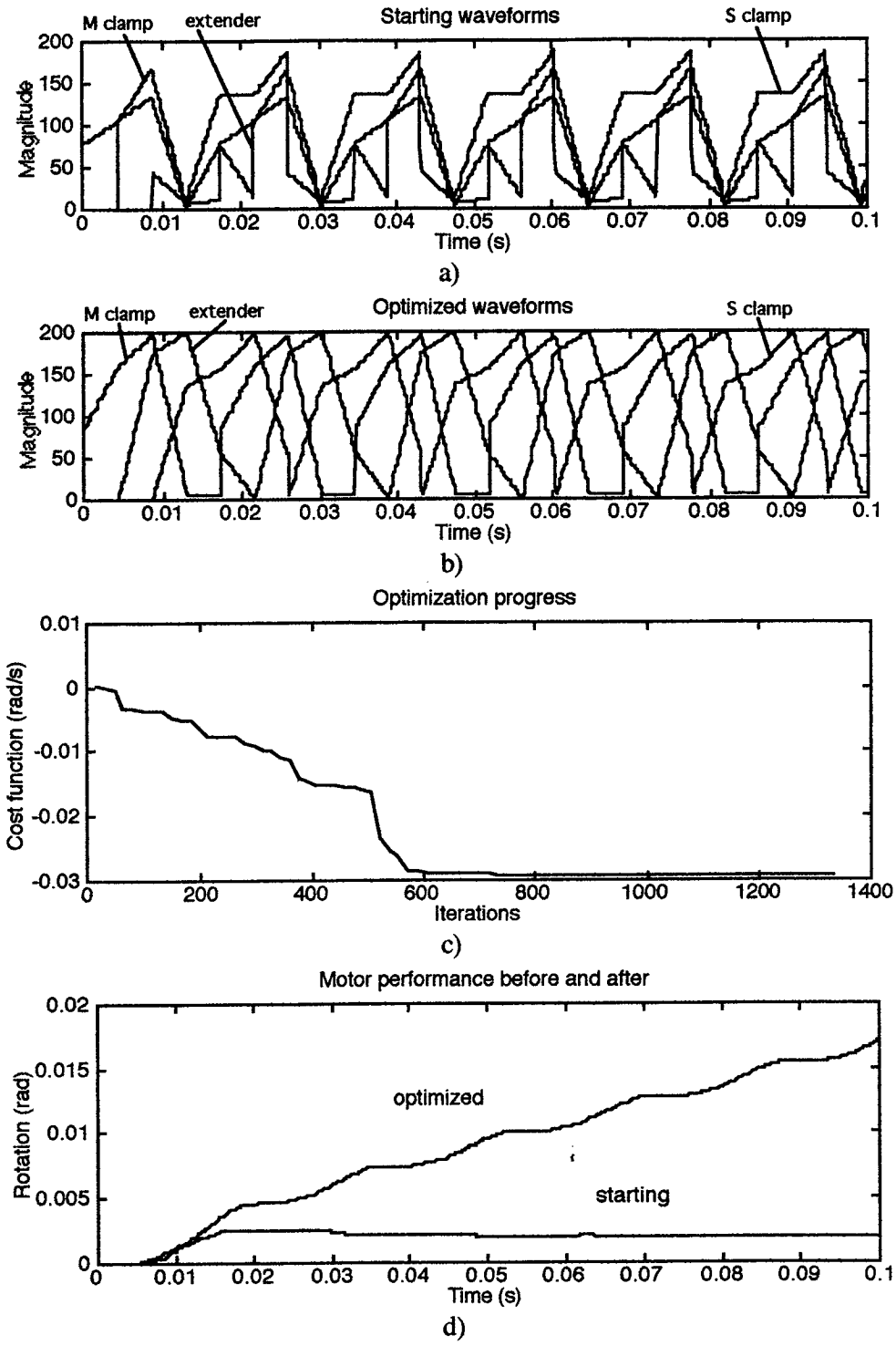

Figure 6.7. Optimization with random starting location: a) starting waveform, b) Optimized waveform, c) Optimization progress, d) Performance before and after optimization.

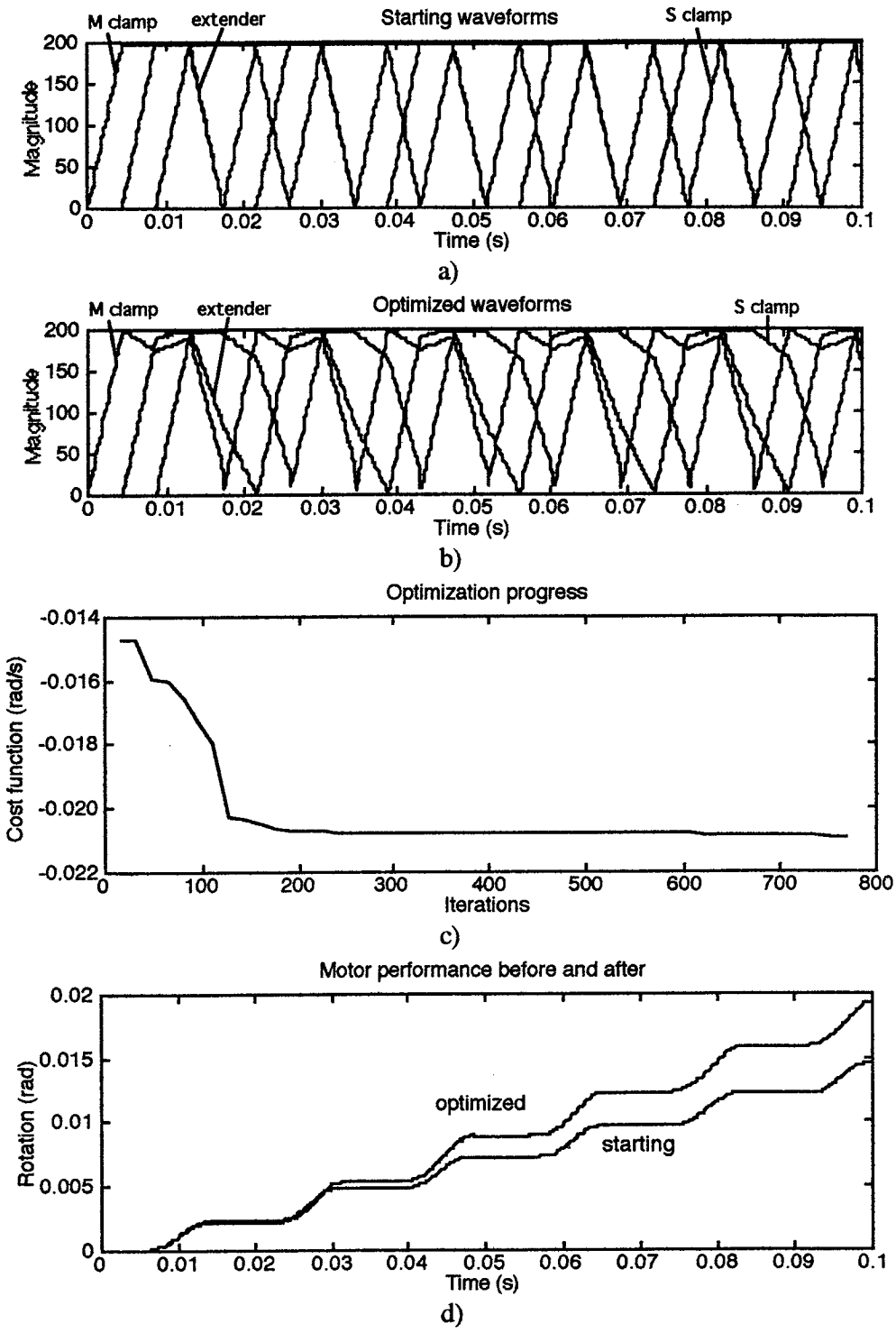

Figure 6.8. Optimization with square wave starting location: a) starting waveform, b) Optimized waveform, c) Optimization progress, d) Performance before and after optimization.

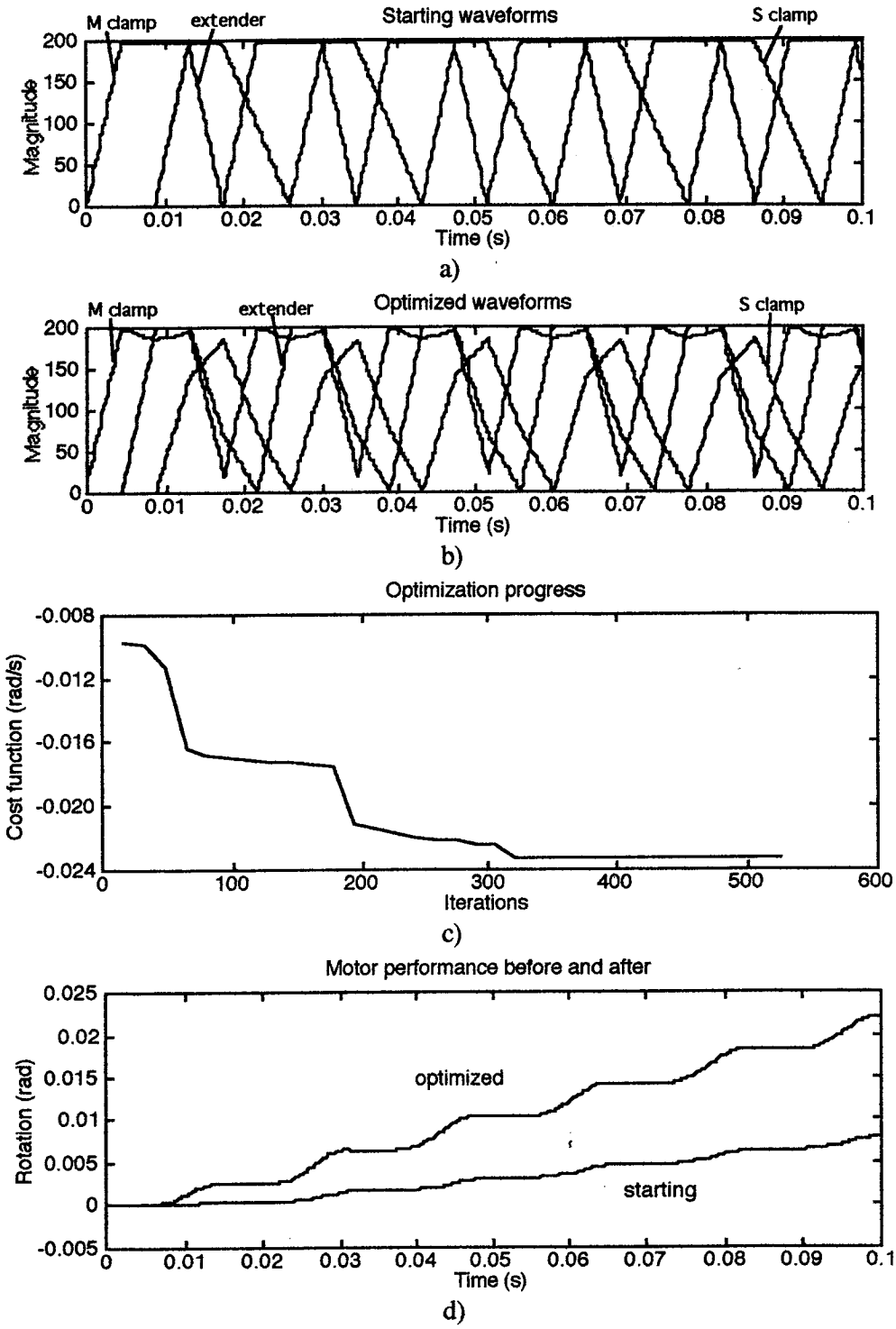

Figure 6.9. Optimization with a different starting location: a) starting waveform, b) Optimized waveform, c) Optimization progress, d) Performance before and after optimization.

The waveform optimization targeted to improve the motor performance at three different frequencies: 30, 60, and 75 Hertz. The 60 Hz frequency was chosen because it is the frequency at which the motor speed peaks out when driving with sinusoidal signals. The 60 Hz frequency is the resonant frequency of the motor. The 30 Hz frequency was chosen because it is half as low than the resonant frequency and is in the quasi-static range. The 75 Hz was chosen instead of 90 Hz because of the power limit in the KEPCO amplifiers which has a roll off frequency at 90 Hz when driving the large capacitive load of the piezoelectric actuators. The optimization at these frequencies was performed using a seven partitions for the initial starting location and then increase to thirteen partitions for a total of thirty nine variables. The optimized waveforms for the noload cases are shown in Figure 6.10-6.12. The optimized waveforms show non-symmetrical shape as compared to sinusoidal or square waves. This non-symmetrical shape compensates for the non-symmetric in the dynamic operation of the motor. The waveforms for the extender at each frequency show a long holding period at the maximum voltage to prevent slippage. Also from these figures, the shapes and phase relation of the optimized waveforms for each targeted frequency are different from each other. The magnitude for the signal of the stationary clamping mechanism is lower than the magnitude for moving clamping mechanism. This is because the moving clamping mechanism needs to exert higher force to push an accelerate the load (rotor) while the stationary clamping mechanism only need to hold it. The lower clamping force also shortens the holding (stand still) period which increases the speed of the motor.

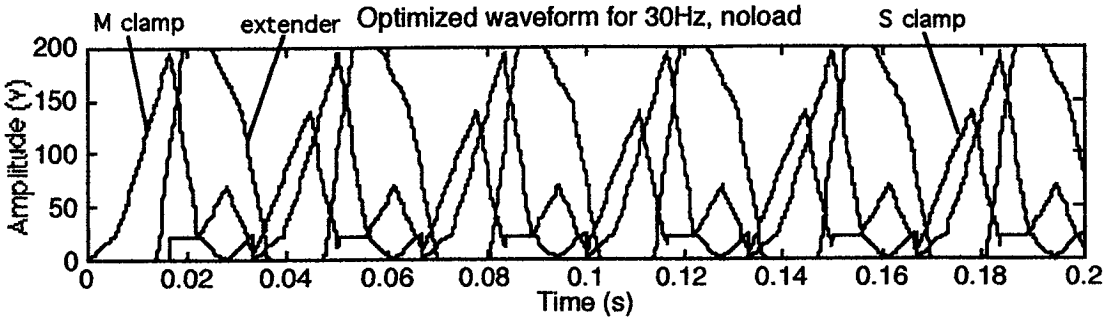

Figure 6.10. Optimized waveform for 30 Hz frequency, noload.

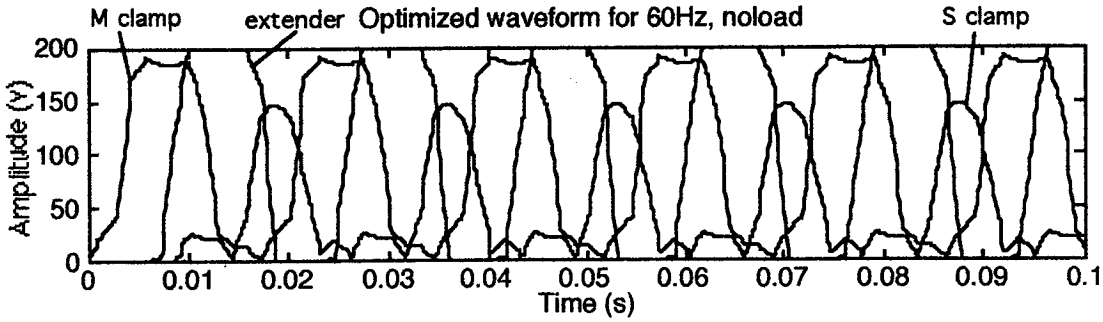

Figure 6.11. Optimized waveform for 60 Hz frequency, noload.

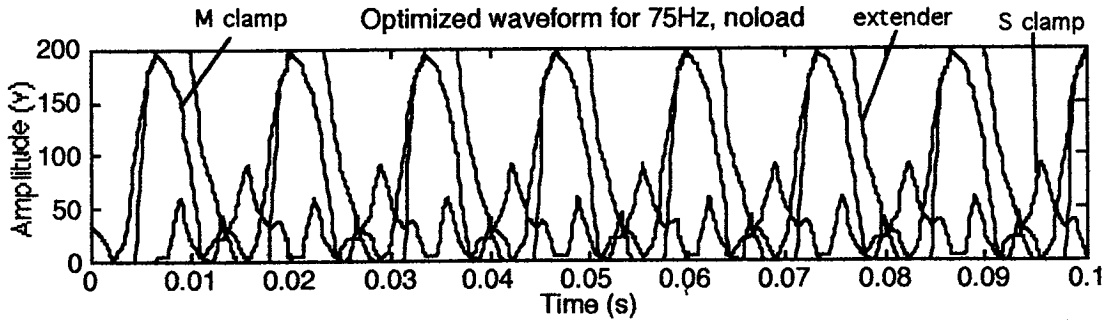

Figure 6.12. Optimized waveform for 75 Hz frequency, noload.

Shown in Figure 6.13 and 6.15 are the optimized waveforms for use when the motor is loaded. For each frequency, the optimized waveform with load is different from the optimized waveform without load. The external load not only exerts torque on the

motor but also adds inertia into the system which changed the dynamic behavior of the motor. The waveform is optimized to compensate for these changes. The magnitude for the stationary clamping mechanism in these figures is higher than with the noload cases. This is because the stationary clamping mechanism needs higher force to keep the motor from slipping under external load. These waveform will be used to drive the motor to verify the optimization results. The experimental verification is covered in Chapter VII.

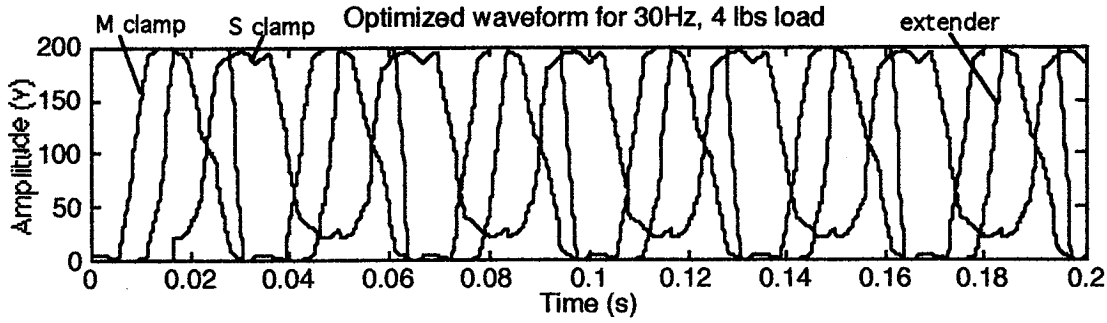

Figure 6.13. Optimized waveform for 30 Hz frequency with 4 lbs load.

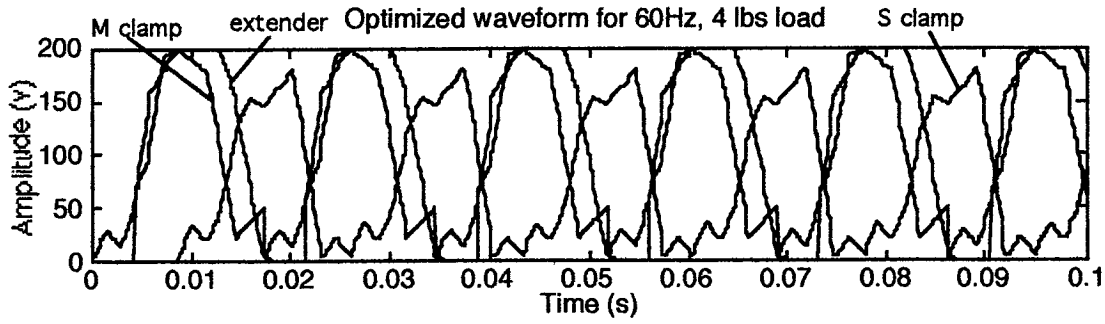

Figure 6.14. Optimized waveform for 60 Hz frequency with 4 lbs load.

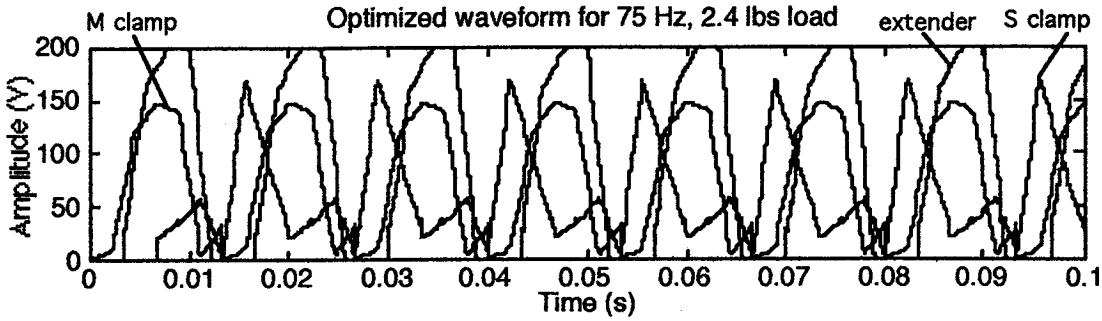

Figure 6.15. Optimized waveform for 75 Hz frequency with 2.4 lbs load.

CHAPTER VII

EXPERIMENTAL VERIFICATION OF WAVEFORM OPTIMIZATION

In this chapter, the results from the waveform optimization are verified experimentally. The optimized waveforms produced from the optimization were used to drive the motor and the performance is compared with the performance when using sine waves as the driving signals. The experiment will verifiy the results predicted by the optimization. The optimized waveforms are generated experimentally by using D-Space Analog-Digital-Analog control system.

Experimental setup

To measure the angular displacement of the motor, the rotor was connected to a one-turn conductive plastic potentiometer. This type of potentiometer was chosen due to its low friction and high resolution characteristics. The potentiometer was calibrated and has an output of 0.0283 V/deg with a 10 V potential across the potentiometer. The arm that connects the rotor and the potentiometer must have low inertia to avoid dynamic interference with the motor operation. It also must be rigid to avoid any unwanted modes to influence with the data recorded. The schematic for the motor test setup is shown in Figure 7.1. The D-Space system is capable of generating four different waveforms simultaneously. This would have been difficult before the advancement in digital signal processing technology and would be almost impossible with analog devices. The optimized waveforms are programmed into the D-Space and generated through its Digital-to-Analog converter. The output signals from D-Space are then fed to three Kepco Bipolar Operational Power Supply and Amplifiers with ±1.0A and ±200V output capability. The output from the potentiometer due to the rotation of the rotor is recorded and stored through the Textronix Digital Oscilloscope TDS420.

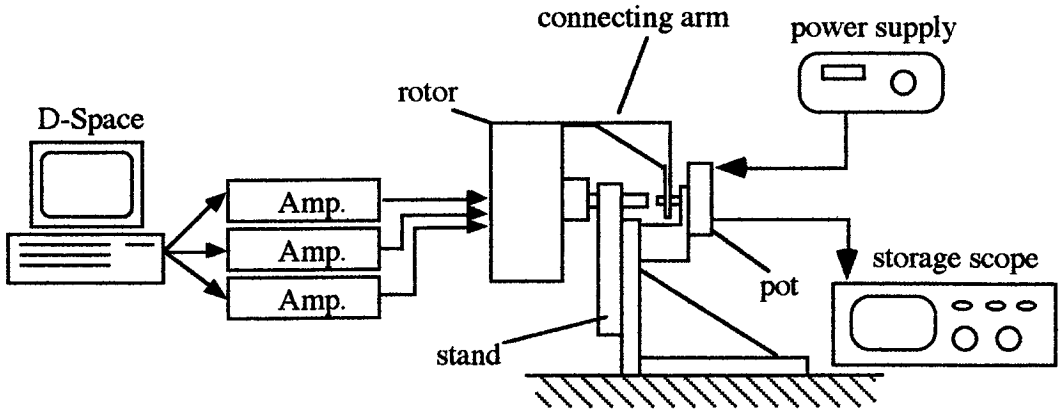

Figure 7.1. Experimental setup.

Experiment verification and discussion

The motor steps were first recorded with sinusoidal signal inputs to establish the base line when compared with the steps produced from driving with the optimized waveforms. These steps were recorded with frequencies ranging from 15-75 Hz, with and without load. Due to the high capacitance of the piezoelectric actuators used in the motor, higher frequency inputs could not be tested because of amplifier saturation. The motor steps recorded experimentally are shown in Figure 7.2--7.9. As seen from these graphs, the motor exhibits the typical stair case step of inchworm motor at low frequencies (15-30 Hz). However, at frequencies above 45 Hz, slippage becomes apparent in the motor step profile. These slippage were explained and disscussed in Chapter IV.

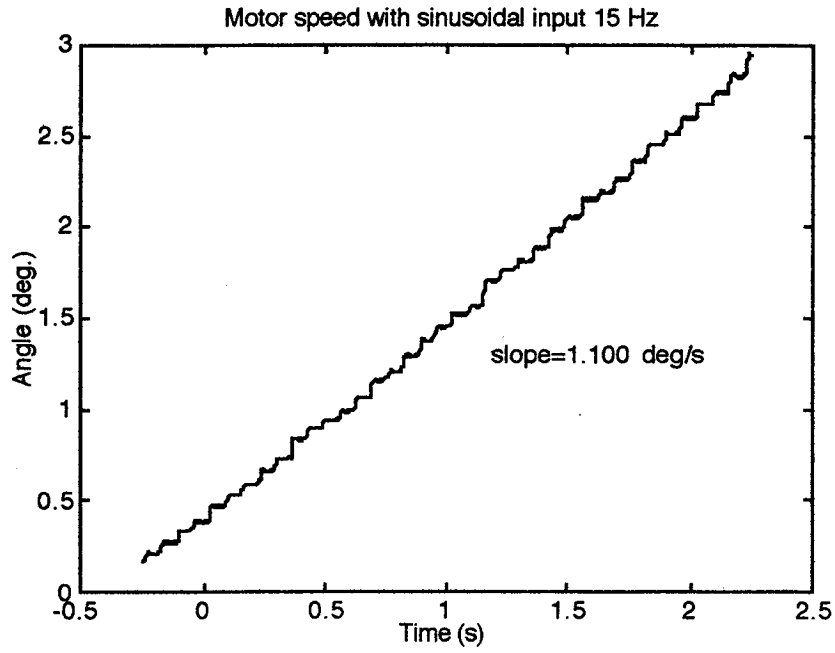

Figure 7.2. Motor steps with sinusoidal input at 15 Hz.

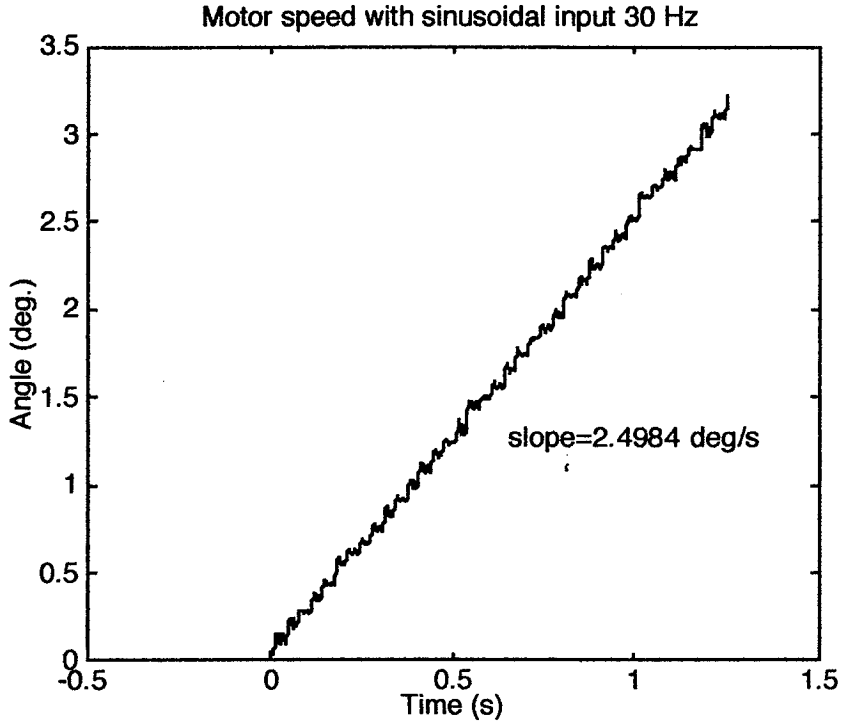

Figure 7.3. Motor steps with sinusoidal input at 30 Hz.

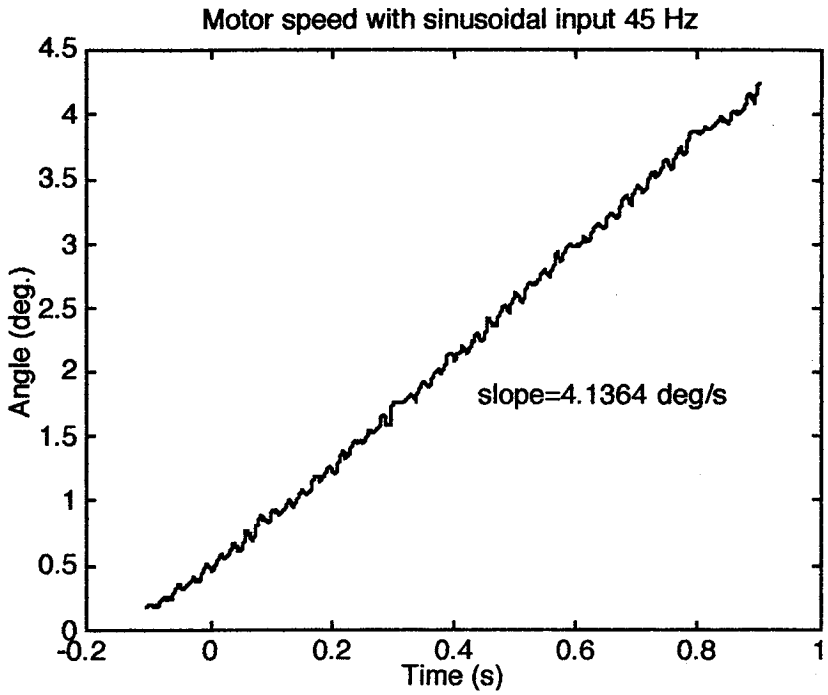

Figure 7.4. Motor steps with sinusoidal input at 45 Hz.

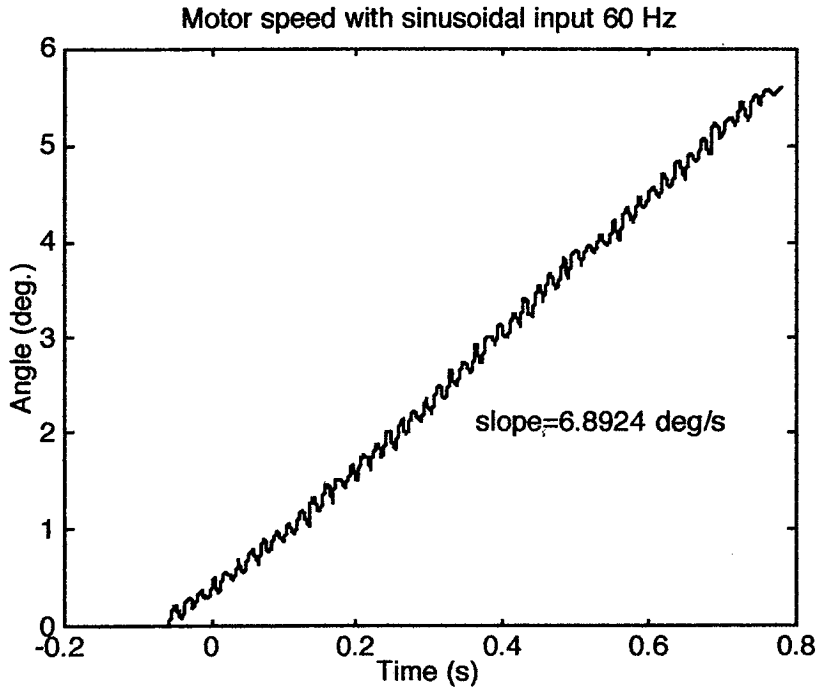

Figure 7.5. Motor steps with sinusoidal input at 60 Hz.

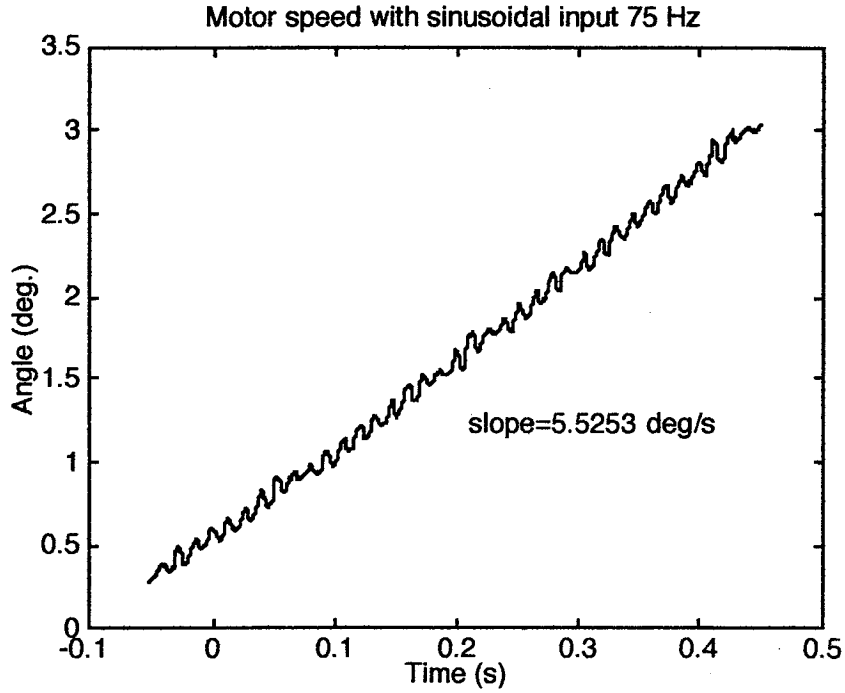

Figure 7.6. Motor steps with sinusoidal input at 75 Hz.

The motor steps were also recorded with the two commonly used input waveforms: square wave and triangle wave. The steps with these inputs are shown in Figure 7.7-7.8. As shown from the figures, the motor speed with the triangle wave input is less than that of a sinusoidal input. This is because the triangle wave contains less energy than the sine wave. However, the square wave input, even with higher energy, produces worse performance. The motor speed with the square wave input is about half when compare to the sinusoidal input at the same frequency. The speed reduction is due mostly to the slippage (stepping backward in the inchworm step). The square wave inputs produced a very high acoutic noise when driving the piezoelectric actuators. It is not desirable to drive the motor with the square wave input for any period of time because the stacks actuators might be easily damaged.

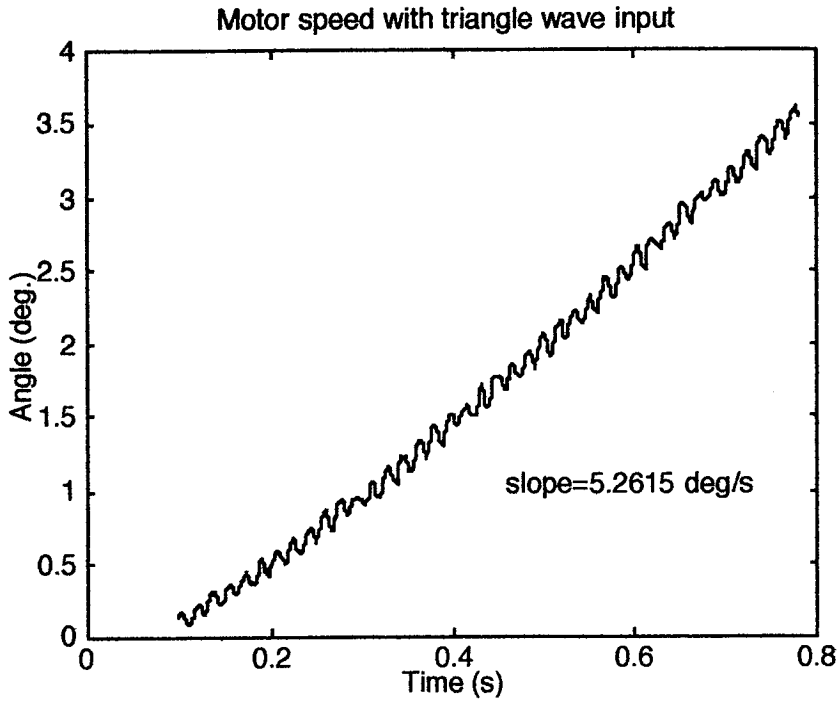

Figure 7.7. Motor steps with triangle wave input at 60 Hz.

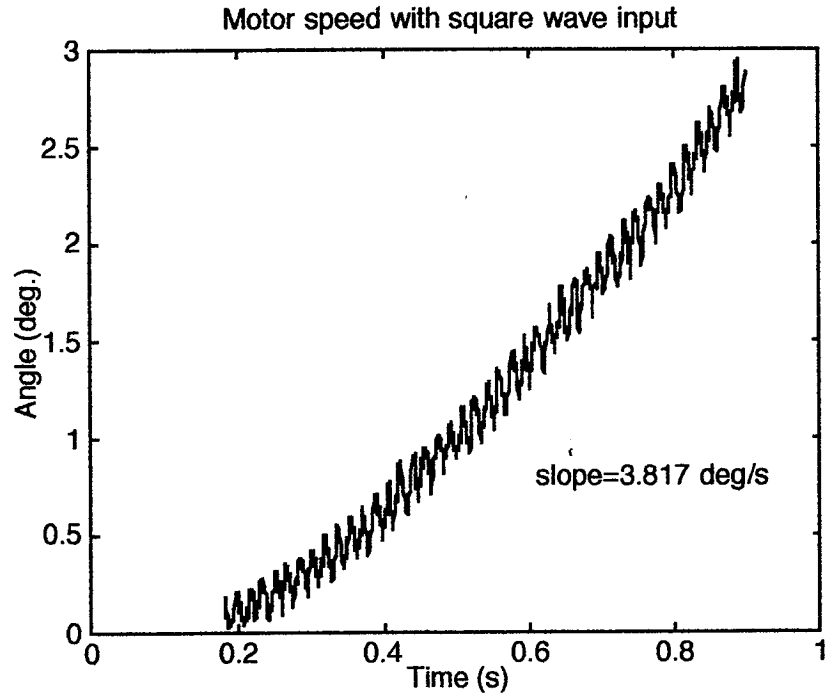

Figure 7.8. Motor steps with square wave input at 60 Hz.

The motor were also tested with external loading condition. The load is applied to the motor by hanging weight as shown previously in Figure 4.7. The motor steps under load are shown in Figure 7.9-7.13. For frequencies under 60 Hz, the hanging weight is 4 lbs. At 75 Hz input, the hanging weight is 2.4 lbs. The motor would not run with a 4 lbs load at this frequency. As expected, the added load and inertia decrease the speed of the motor. Table 7.1 show the percentage of decrease in speed for each frequency tested with the added load.

Table 7.1. Comparision of motor speed with and without load.

Frequency (Hz)	Speed w/o load (deg./s)	Speed with load (deg./s)	% decrease (%)
15 Hz	1.100	0.772	29.8
30 Hz	2.498	2.173	13.0
45 Hz	4.136	2.644	36.1
60 Hz	6.892	1.648	76.1
75 Hz	5.525	4.187 (2.4 lbs)	24.2

From the table, the motor speed is greatest at 60 Hz. This is the resonant frequency of the motor. However, with the added load, the motor also experienced the greatest decrease in speed at 60 Hz under load. The added load and inertia completely change the dynamic of the motor, the motor is no longer operated at its resonant frequency, hence the decrease in speed. At 30 Hz, the motor experienced the least degradation in speed with load. At this frequency, although the added load slows down the motor, the added inertia lower the resonant frequency of the motor. The increase in speed by operating at resonant frequency partially compensates for the decrease caused by load, which results in less overall decrease in speed.

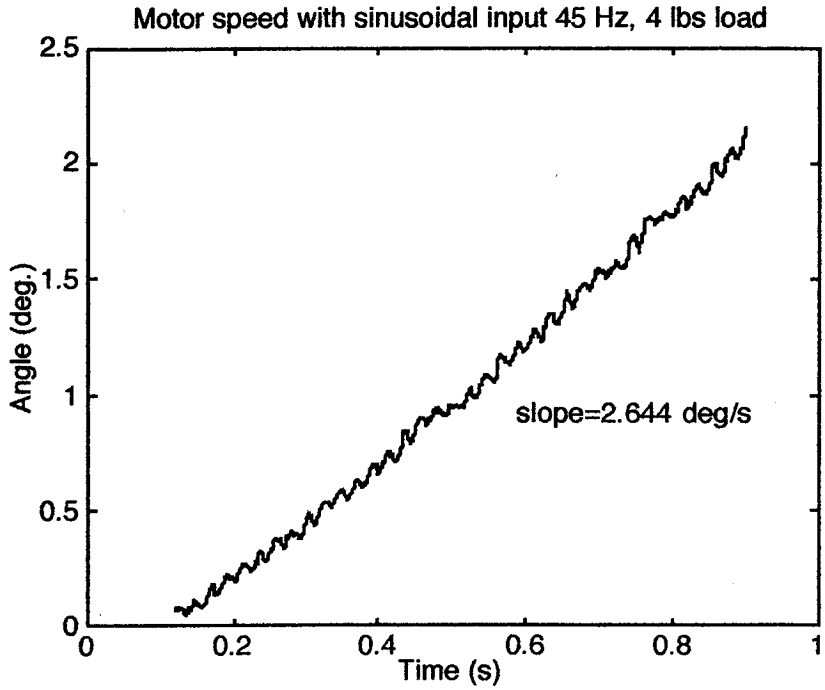

Figure 7.11. Motor speed with sinusoidal input at 45 Hz, 4 lbs load.

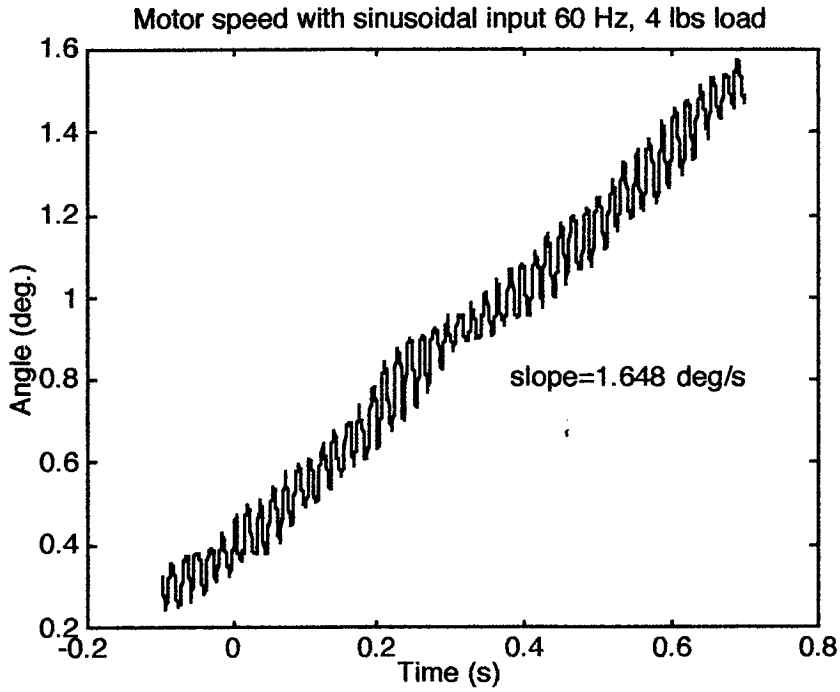

Figure 7.12. Motor speed with sinusoidal input at 60 Hz, 4 lbs load.

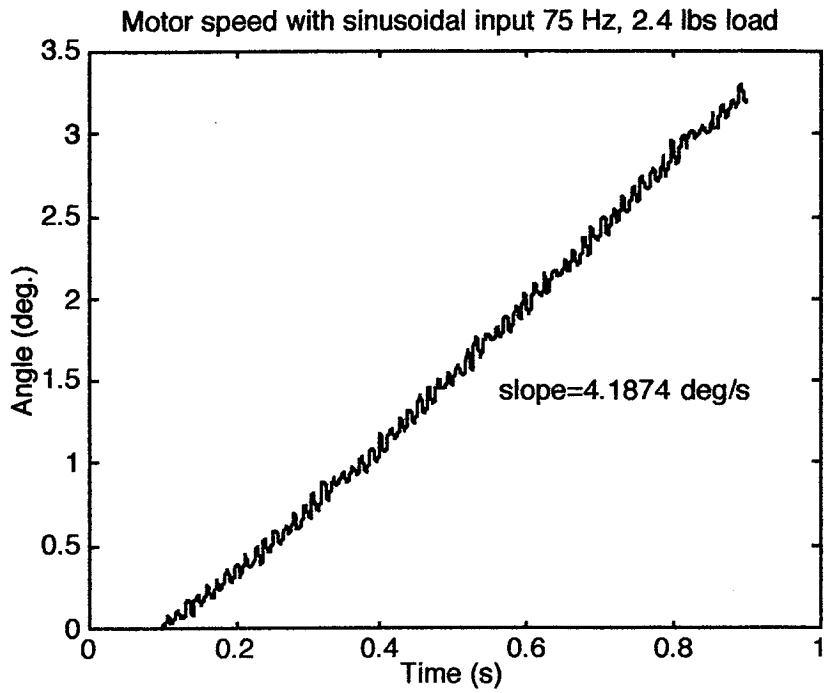

Figure 7.13. Motor speed with sinusoidal input at 75 Hz, 2.4 lbs load.

After the baseline for the performance of the motor was established. The motor is subject to test with the optimized waveforms. The motor speed and step profiles produced by the model when driving with the optimized waveforms at the selected frequencies are shown in Figure 7.14-7.16. When driving with the optimized waveforms shown in Chapter VI, the model predicts vast improvement in the motor speed. The predicted profiles show the reduction in the pausing (flat portion) of the inchworm step at 30 Hz (Figure 7.14) and almost became a straight and continuous displacement at 75 Hz (Figure 7.16). This is the best possible speed that the motor can achieve because there is no pause and backward movement. The step profile indicates that the optimization has found the global minimum.

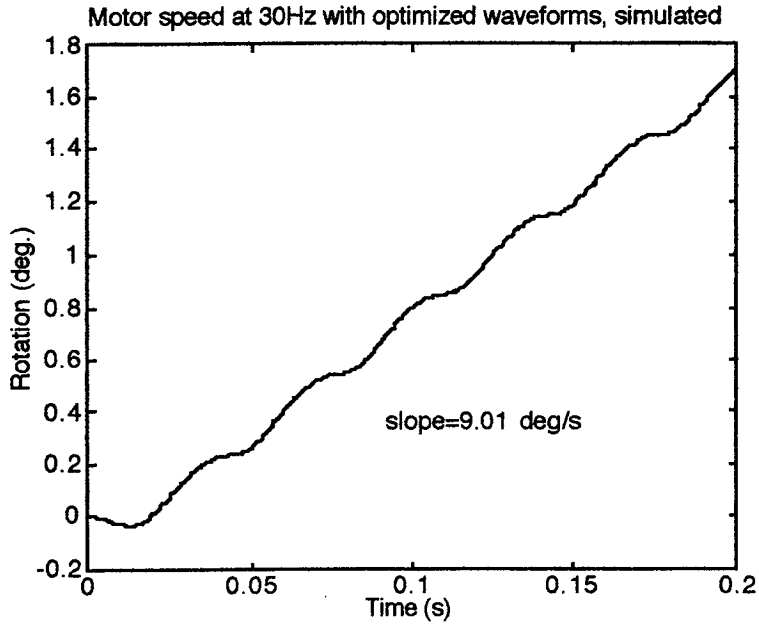

Figure 7.14. Simulated motor speed with optimized waveform at 30 Hz.

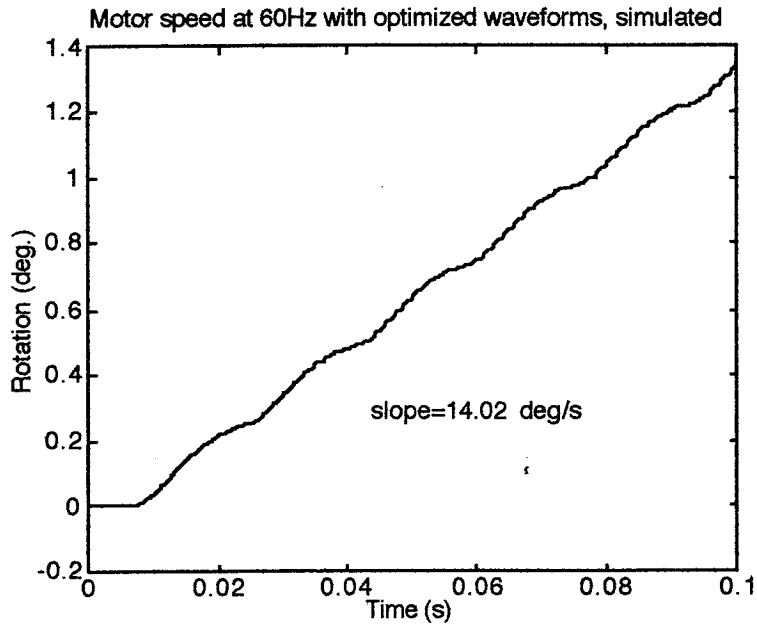

Figure 7.15. Simulated motor speed with optimized waveform at 60 Hz.

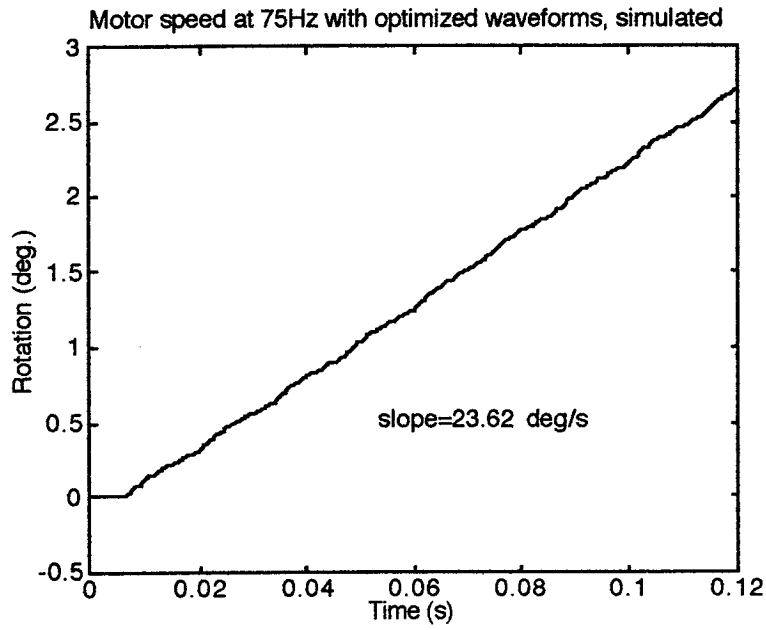

Figure 7.16. Simulated motor speed with optimized waveform at 75 Hz.

The motor is then tested for speed using the optimized waveforms shown in Chapter VI. As predicted by the optimization, the motor speed improve dramatically with and without load. The experimentally captured motor step profiles with optimized inputs are shown in Figure 7.17-7.19. As seen from the figures, the optimized waveform almost completely "straighten" out the stair case step profile of the inchworm motor as predicted. The flat portion of the stair case, which does not contribute to forward motion is almost completely eliminated. The slippage seen at 60 and 75 Hz frequency with sinusoidal inputs is also completely eliminated. By eliminating the slippage and the pausing preiod (flat portion of the inchworm staircase step), the motor achieves the best possible speed, the speed that provided by the capability of the swinger/extender. This is also an indication that the optimization has found the global minimum for each frequency case. Table 7.2 summarized the improvement in speed when running with the optimized waveforms.

Table 7.2. Comparision of motor speed with sinusoidal and optimized waveforms

Frequency (Hz)	Speed with sinusoidal input (deg./s)	Speed with optimized input (deg./s)	Percent increase (%)
30	2.50	10.07	302
60	6.89	15.73	128
75	5.25	22.68	332

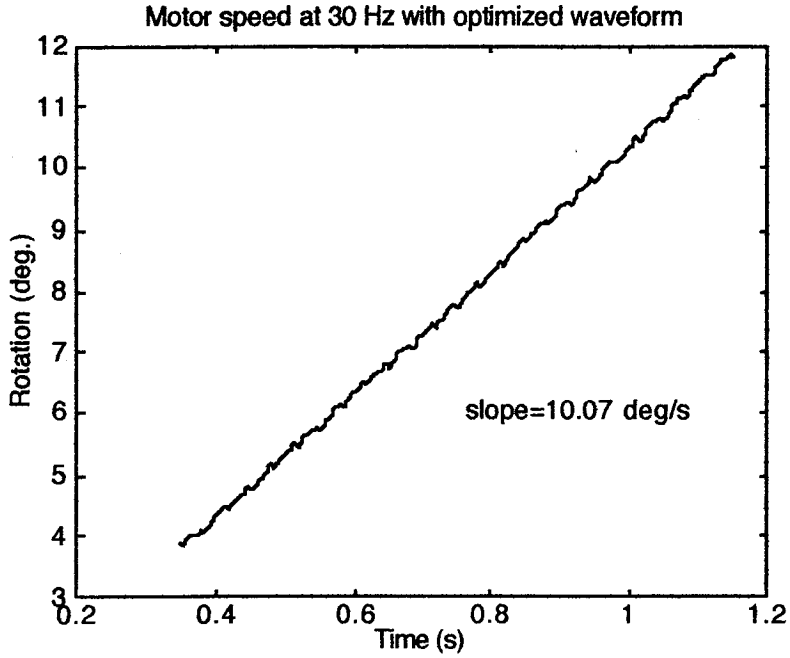

Figure 7.17. Motor speed with optimized waveform input at 30 Hz.

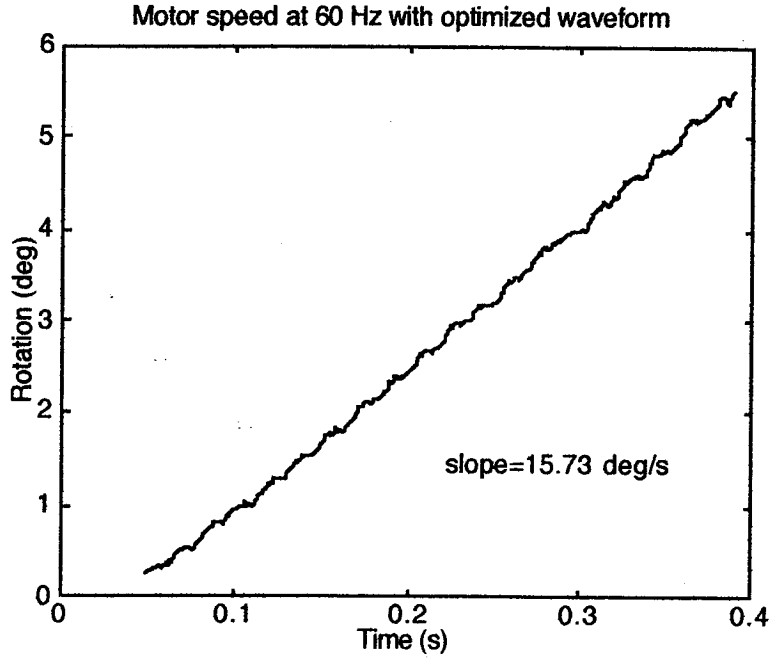

Figure 7.18. Motor speed with optimized waveform input at 60 Hz.

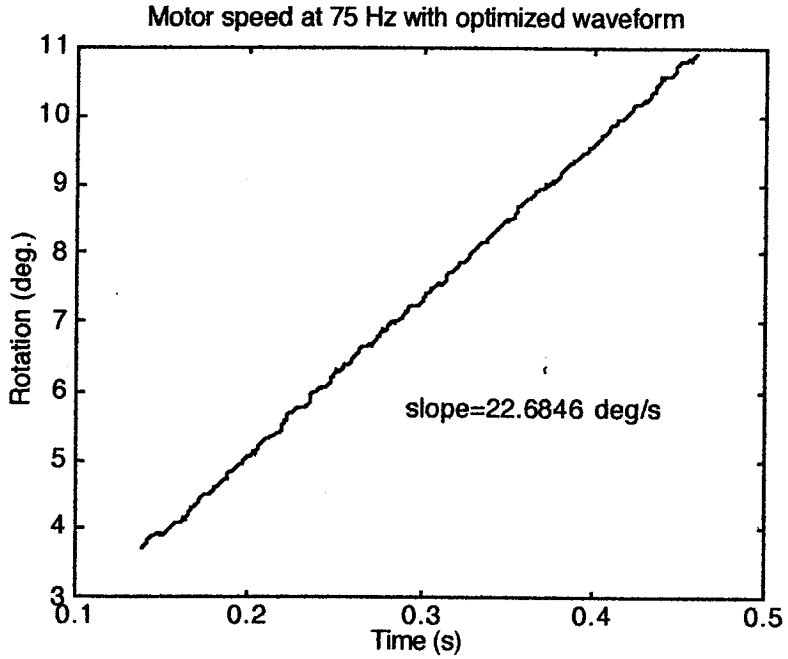

Figure 7.19. Motor speed with optimized waveform input at 75 Hz.

The motor was also tested under loading condition using the waveforms optimized for each specific load cases. The step profiles under load are shown in Figure 7.20 and 7.21. Table 7.3 shows the comparision of motor speed between sinusoidal and optimized waveforms with 4 lbs load

Table 7.3 Comparision of motor speed under 4 lbs load.

Frequency (Hz)	Speed with sinusoidal input (deg./s)	Speed with optimized input (deg./s)	Percent increase (%)
30	2.17	3.56	64
60	1.65	6.02	265
75 (2.4 lbs)	4.19	11.04	163

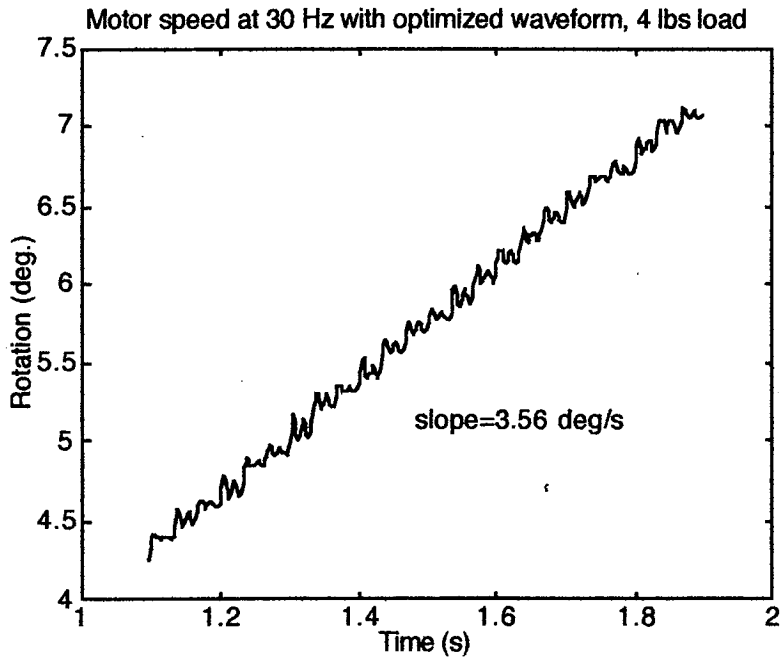

Figure 7.20. Motor speed with optimized waveform at 30 Hz, 4 lbs load.

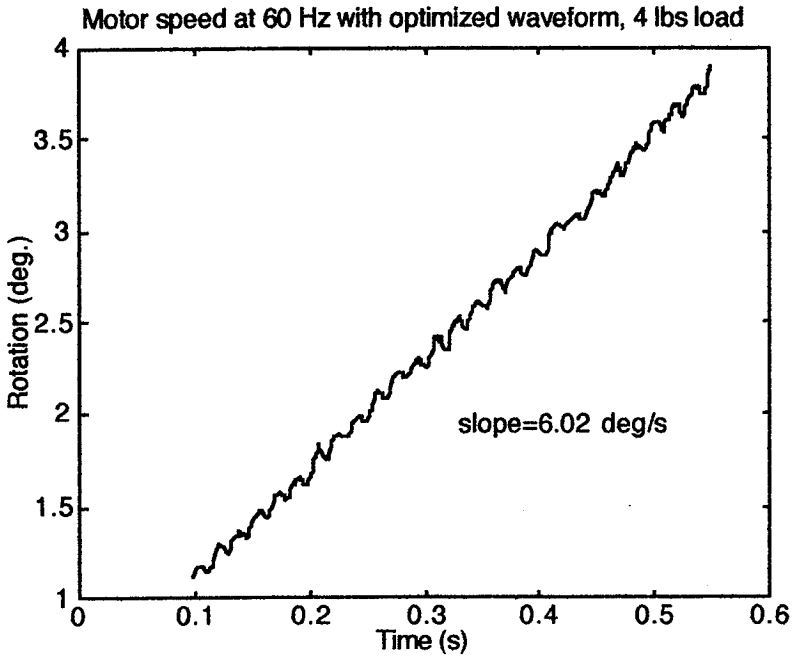

Figure 7.21. Motor speed with optimized waveform input at 60 Hz, 4 lbs.

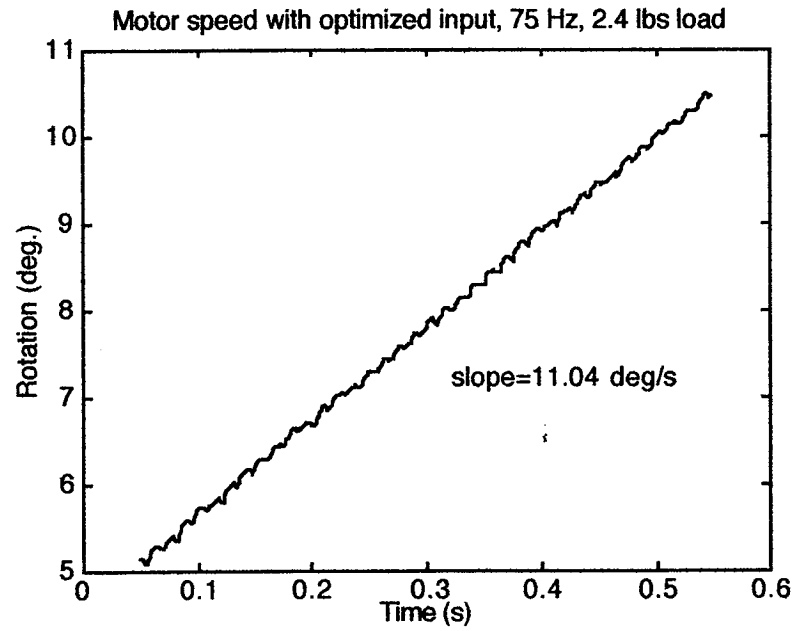

Figure 7.22. Motor speed with optimized waveform input at 75 Hz, 2.4 lbs.

From the above figures and table, it can be seen that the optimized waveforms drastically improved the speed of the motor under load. The improvement is greatest at 60 Hz frequency (265%). The increase in speed is mostly due to the reduction in slippage when driving with the optimized waveform. There is less improvement in speed at 30 Hz frequency when compared to the improvement at 60 Hz, even though 64% improvement is impressive all by itself. The increase in speed at 75 Hz is 163%. The reduction in slippage is mostly responsible for the increase in the speed of the motor at this frequency. The motor when driven with the optimized waveforms is also capable of carying 4 lbs at this frequency with a speed of 2.94 deg/s. The motor stalled with this load when driven with a sinusoidal signal.

Assessment of motor precision

The motor was also tested to assess the precision of its inchworm steps. In this test, the motor was driven to produce fifteen inchworm steps. The motor is stopped after fifteen steps and hold on to its position using both clamping mechanisms. The distance traveled after fifteen steps is recorded. The process is repeated twenty times. This precision test was conducted at three different frequencies using both sinusoidal and optimized driving signals so that comparision can be made about the precision of the motor between driving with sinusoidal and optimized waveforms. Table 7.4 shows the mean and standard deviation for the measurements at each frequency. The distance traveled after fifteen steps is also presented in a scatter plot format. Figure 7.23-7.28 show these scatter plots for different frequencies and driving signals.

Table 7.4. Mean and standard deviation for distance travel after fifteen steps.

	Mean (deg)	Standard deviation (deg)
Sinusoidal, 30 Hz	1.6033	.0256

Sinusoidal, 60 Hz	2.2319	.0043
Sinusoidal, 75 Hz	1.3646	.0239
Optimized, 30 Hz	5.6557	.0942
Optimized, 60 Hz	4.7823	.0028
Optimized, 75 Hz	4.9672	.0740

From Table 7.4, the standard deviation of the motor is smallest when driving with the optimized waveform at 60 Hz frequency. However, the standard deviation does not completely represent the repeatability or precision of the motor. There are many factors that contribute to the error of the measurement such as the fluctuation in voltage of the power supply, noise in the measurement, and the fluctuation in the driving signals themselves. These factors influence the standard deviation. A closer look at the scatter plots would reveal that the variation is large over a large period of time. The variation is much smaller from one data point to the next when the order of measurement is taken into account. In fact, in Figure 7.25, the motor precision is much better in the last ten measurements. The motor was able to repeat the distance traveled almost exactly. The same phenomena can be observed in Figure 7.27. The drifting of the precision is obvious in Figure 7.25. The degradation in the precision in this scatter plot is caused by the noise and drifting of the measuring instruments. Overall, the motor can repeat the distance using the optimized waveform with the precision of about 7 arc-sec. This level of precision can rival some of the angular positioning devicces using optical encoder feedback. Better level of precision can be obtained with the motor if a tighter controlled environment is achieved.

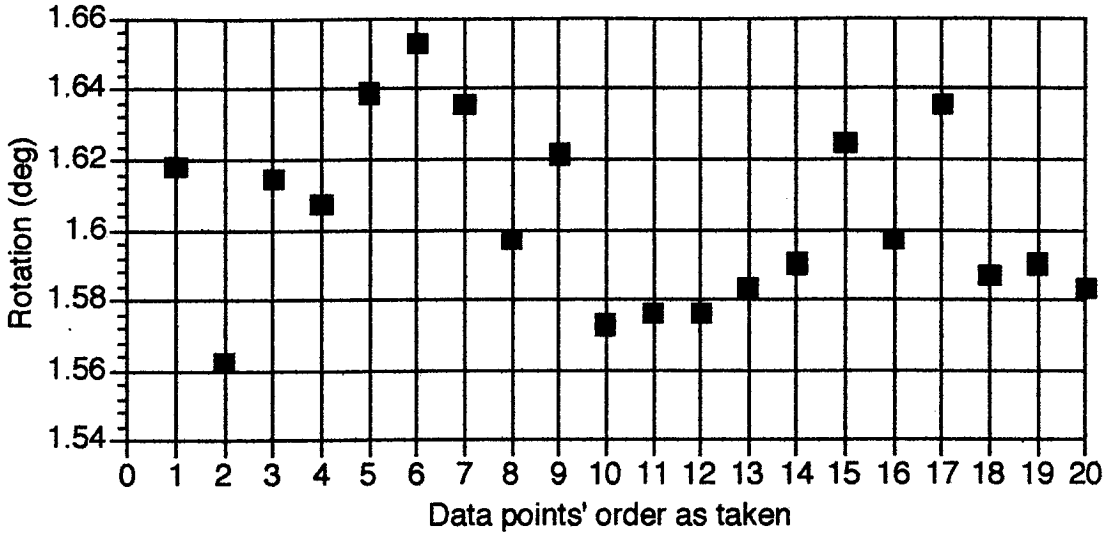

Figure 7.23. Distance traveled after fifteen steps with sinusoidal signals, 30 Hz.

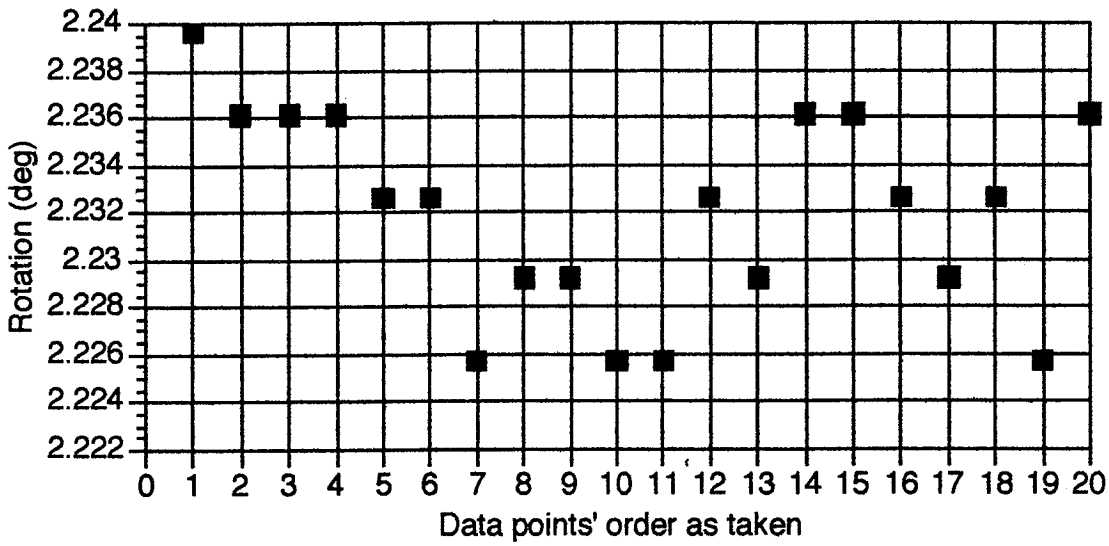

Figure 7.24. Distance traveled after fifteen steps with sinusoidal signals, 60 Hz.

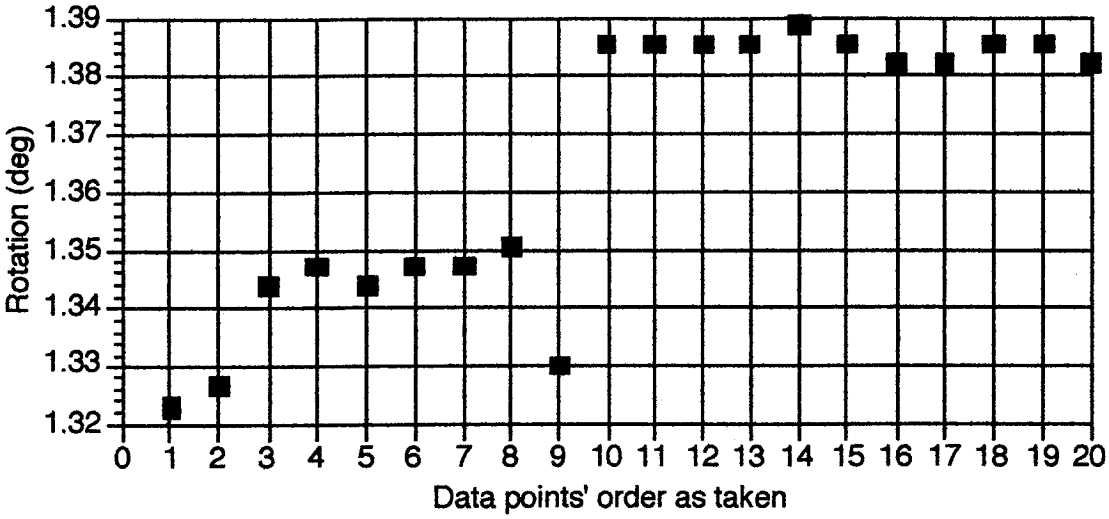

Figure 7.25. Distance traveled after fifteen steps with sinusoidal signals, 75 Hz.

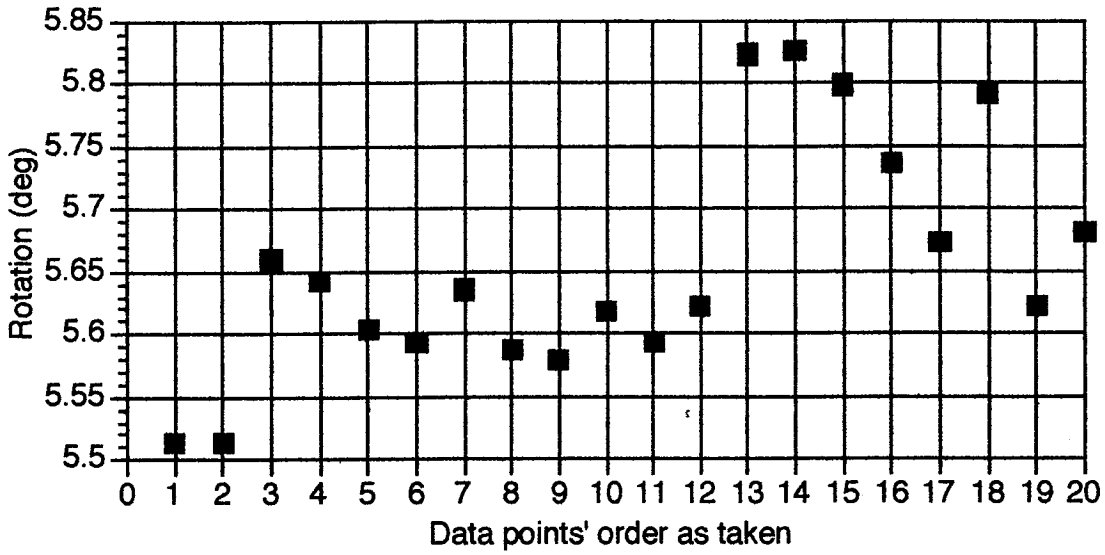

Figure 7.26. Distance traveled after fifteen steps with optimized signals, 30 Hz.

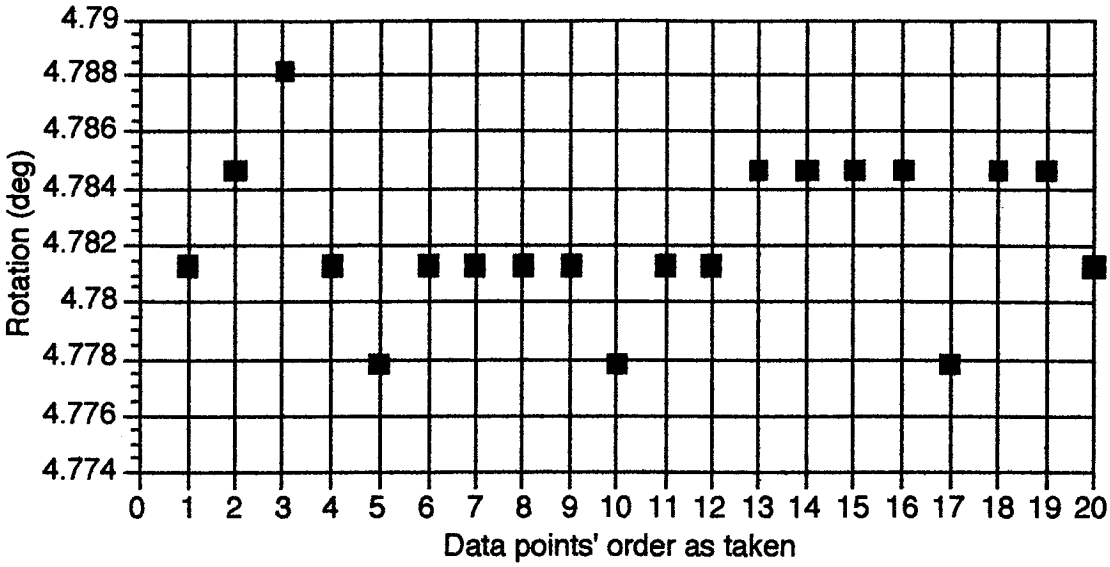

Figure 7.27. Distance traveled after fifteen steps with optimized signals, 60 Hz.

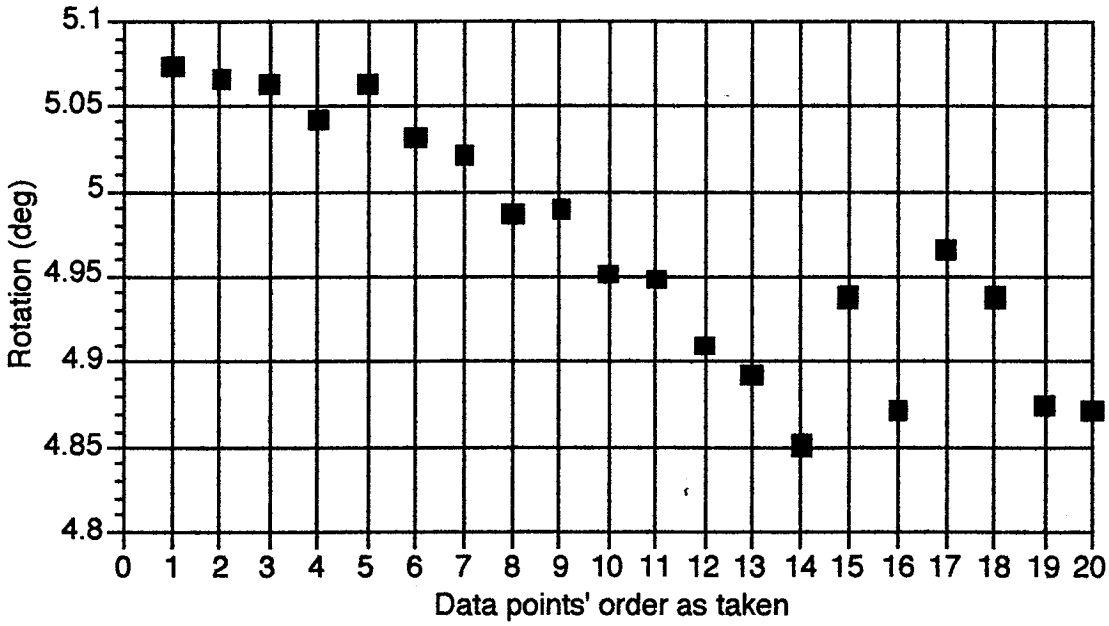

Figure 7.28. Distance traveled after fifteen steps with optimized signals, 75 Hz.

CHAPTER VIII

CONCLUSIONS

A novel rotary motor concept was successfully design, fabricated, and operated. This work has demonstrated a proof of concept for a torsional inchworm type motor. The prototype motor has shown that piezoelectric stack actuators can be used for rotary inchworm motor. The discrete linear motion of piezoelectric stacks can be converted into rotary stepping motion. The stacks with its high force and displacement output are suitable actuators for use in piezoelectric motor. The designed motor is capable of delivering high torque and speed. Critical issues involving the design and operation of piezoelectric motors were studied. The tolerance between the contact shoes and the rotor has proved to be very critical to the performance of the motor. Based on the prototype motor, a waveform optimization scheme was proposed and implemented to improve the performance of the motor. The motor was successfully modeled in MATLAB SIMULINK. The model closely represents the behavior of the prototype motor. Using the motor model, the input waveforms were successfully optimized to improve the performance of the motor in term of speed, torque, power and precision. These optimized waveforms drastically improve the speed of the motor at different frequencies and loading conditions experimentally. The optimized waveforms also increase the level of precision of the motor. The use of the optimized waveform is a break-away from the traditional use of sinusoidal and square waves as the driving signals. This waveform optimization scheme can be applied to any inchworm motors to improve their performance.

The prototype motor in this dissertation as a proof of concept was designed to be robust and large. Future motor can be designed much smaller and more efficient with lessons learned from the prototype motor.

APPENDICES

APPENDIX A: TECHNICAL DRAWINGS OF MOTOR'S COMPONENTS

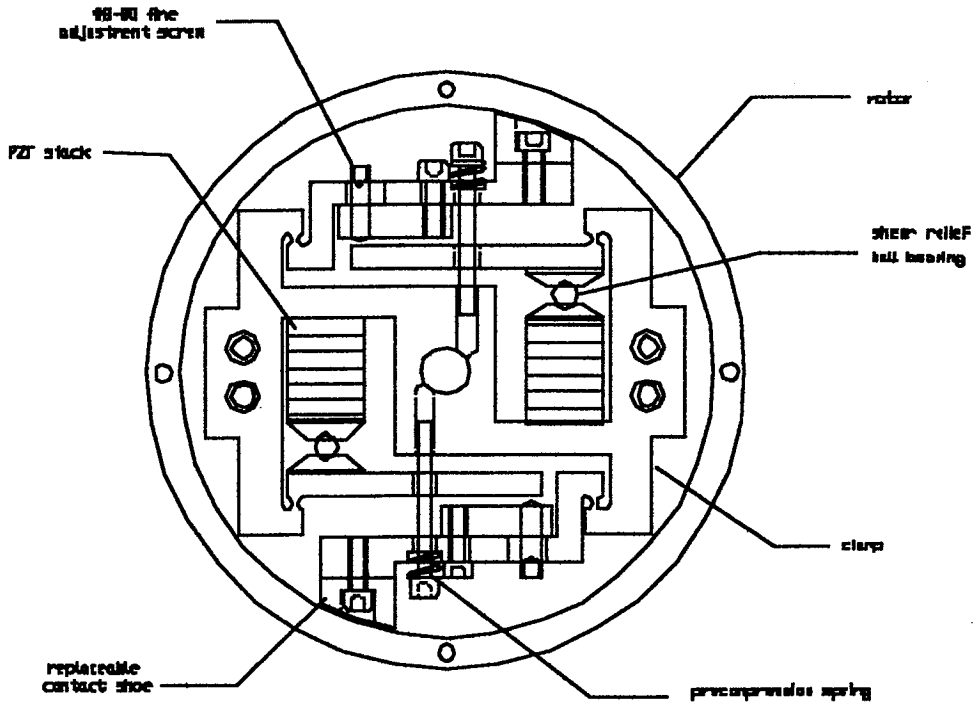

Figure A1. Drawing of motor assembly.

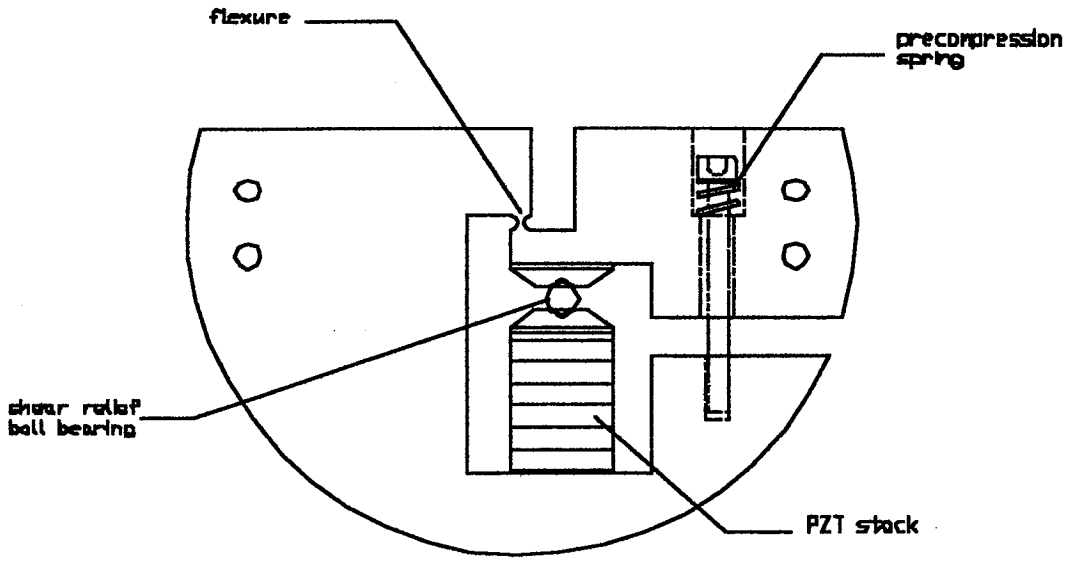

Figure A2. Drawing of swinger/extender assembly.

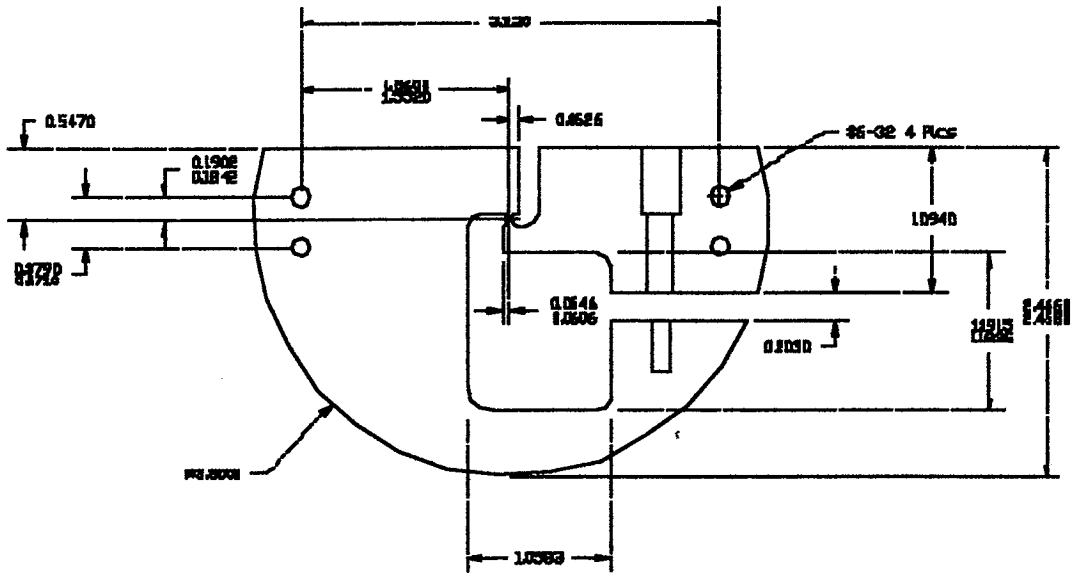

Figure A3. Dimensioned drawing of swinger/extender, front view.

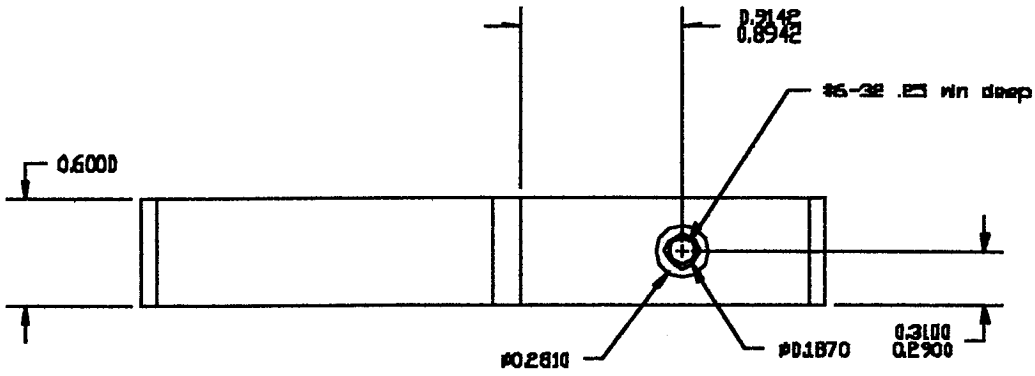

Figure A4. Dimensioned drawing of swinger/extender, top view.

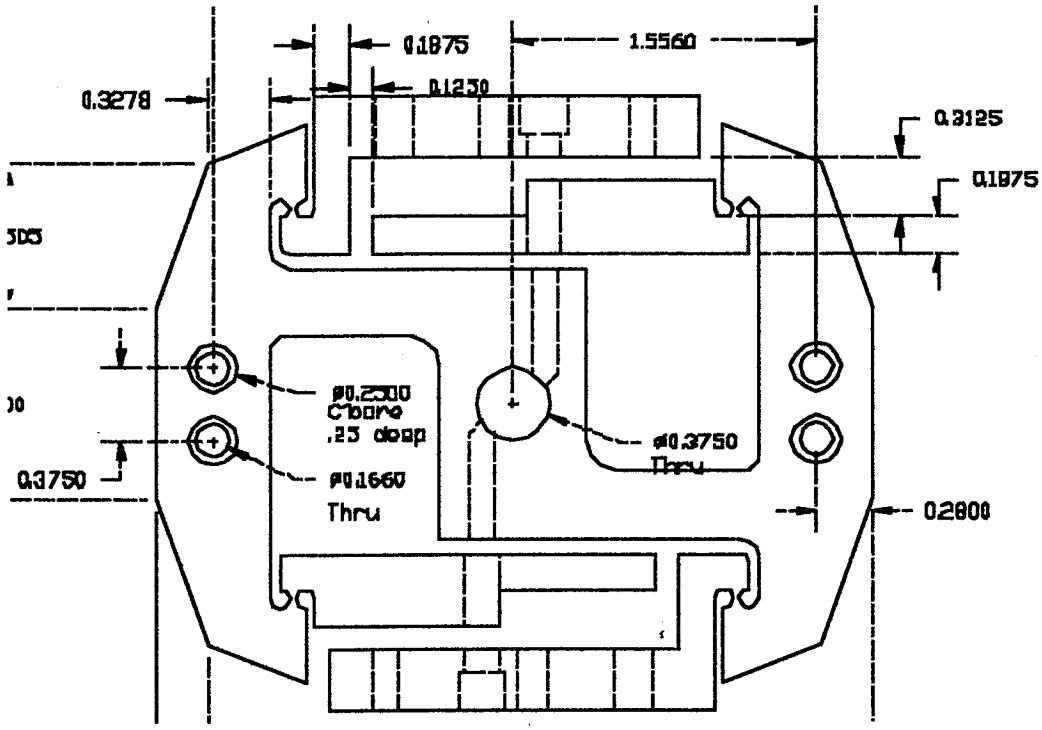

Figure A5. Dimensioned drawing of clamping mechanism, front view.

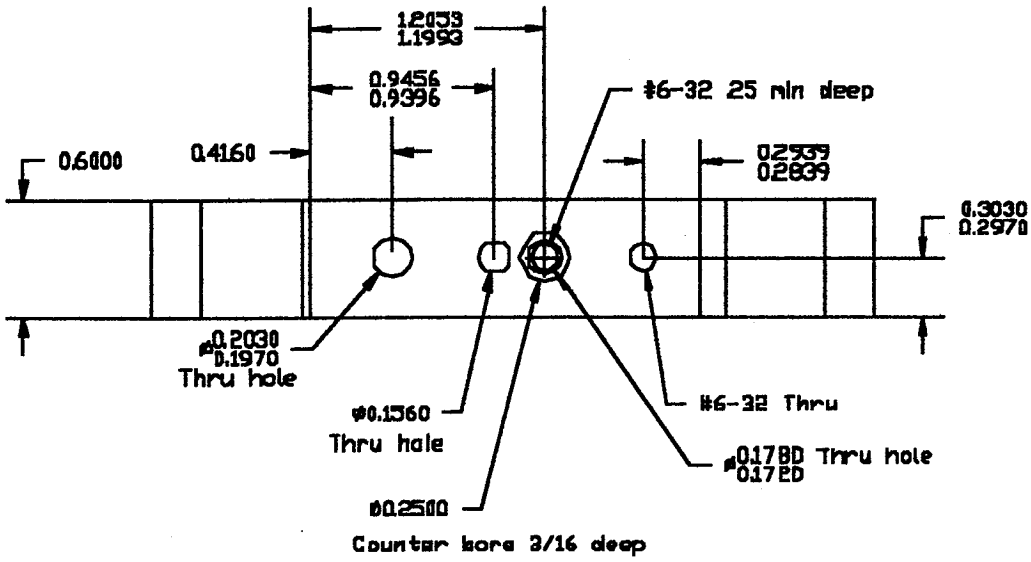

Figure A6. Dimensioned drawing of clamping mechanism, top view.

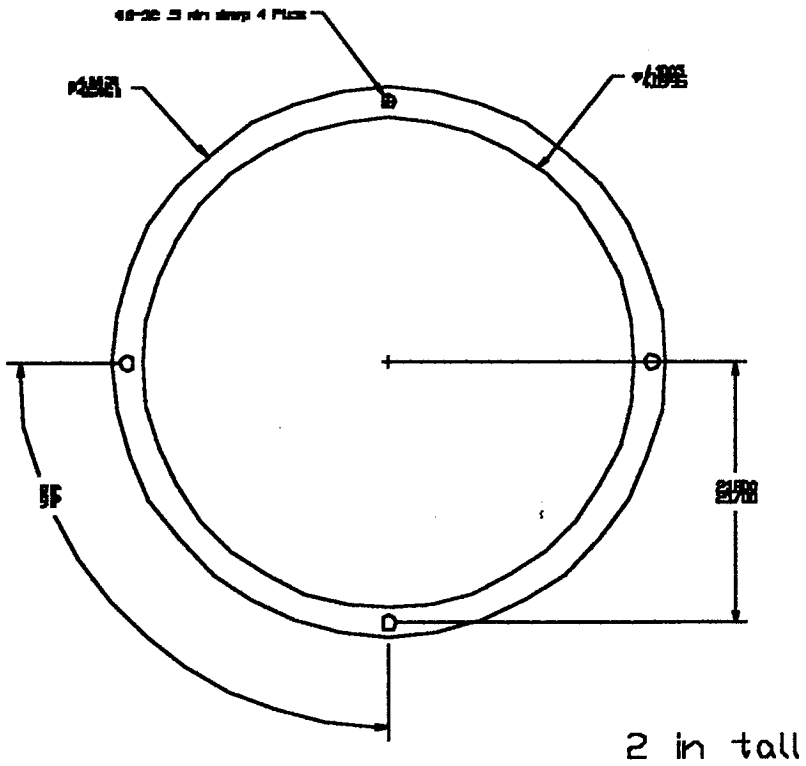

Figure A7. Dimensioned drawing of rotor.

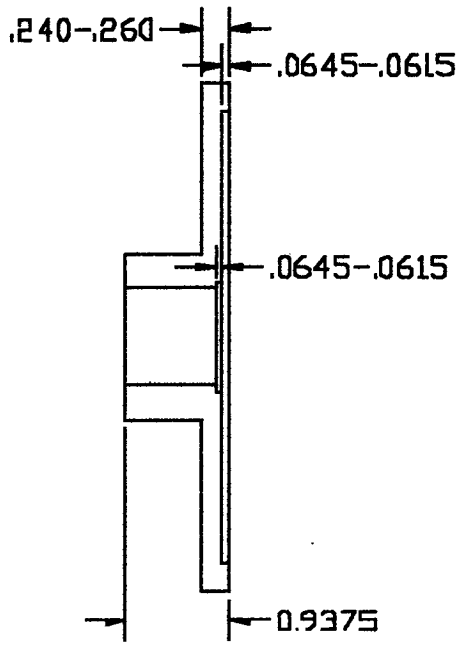

Figure A8. Dimensioned drawing of motor cover, cut-away view.

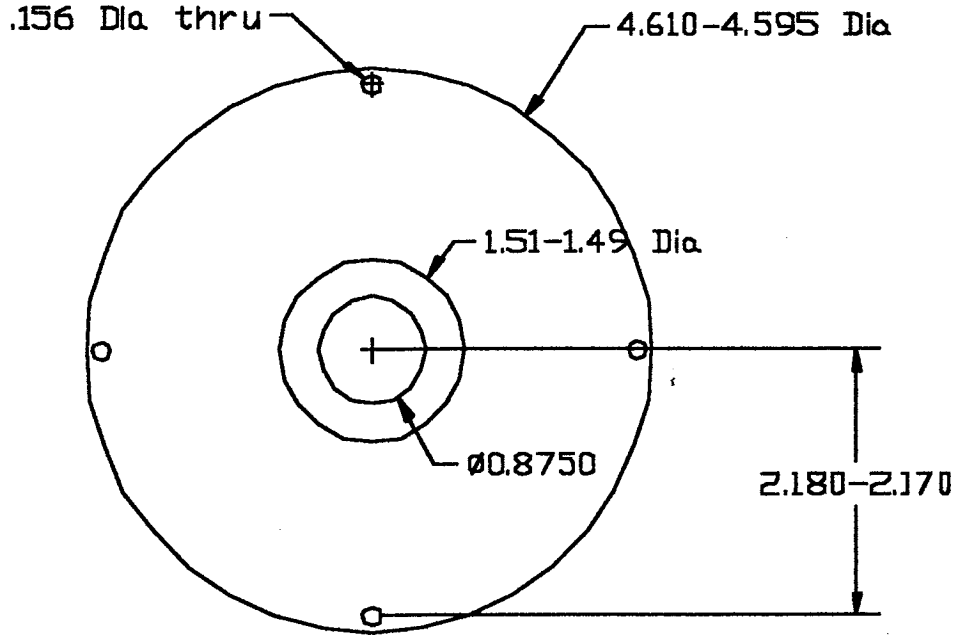

Figure A9. Dimensioned drawing of motor cover, front view.

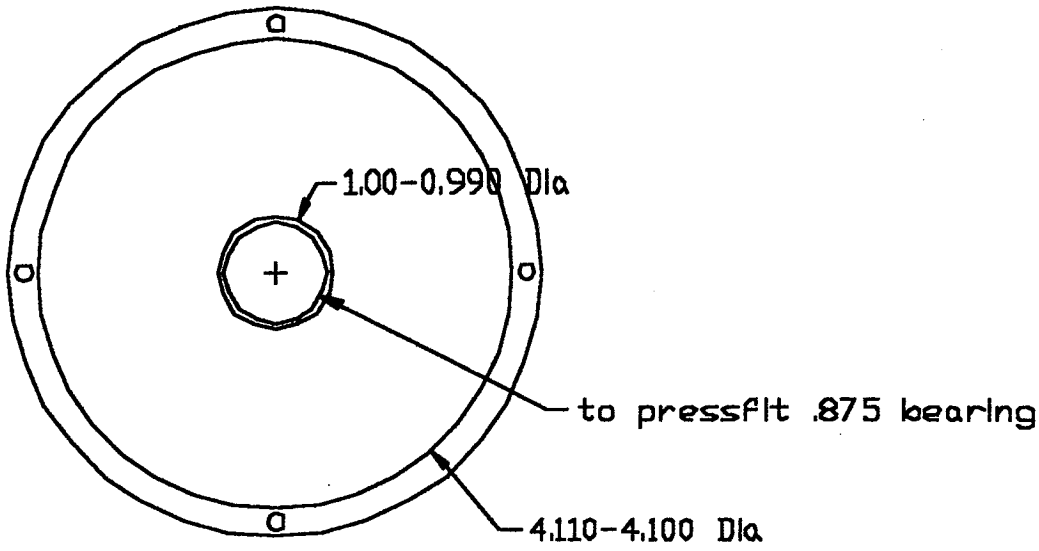

Figure A10. Dimensioned drawing of motor cover, back view.

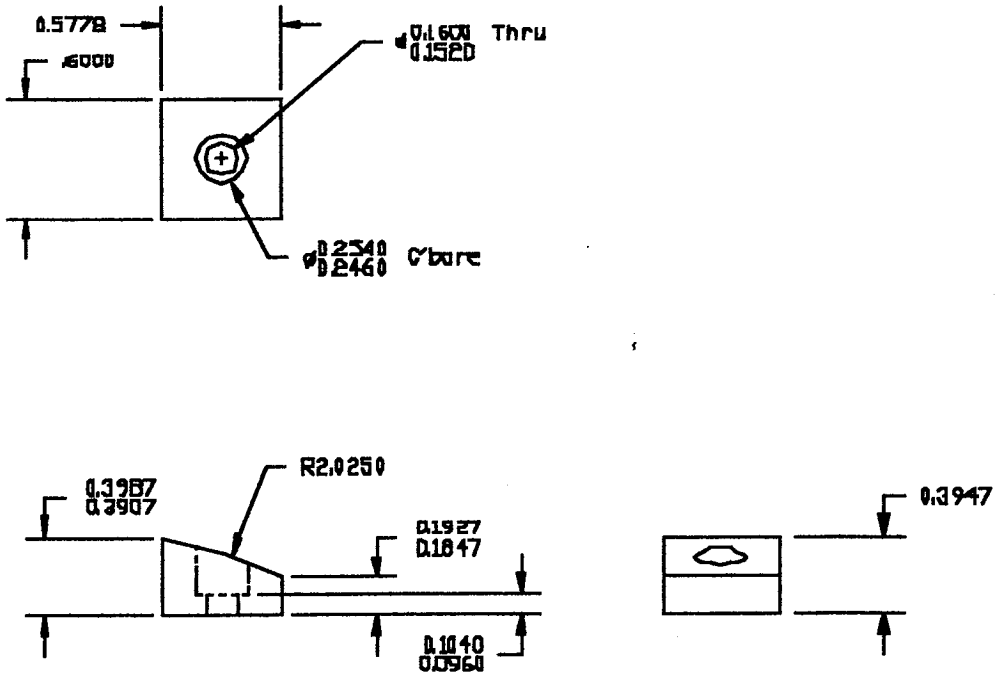

Figure A11. Dimensioned drawing of contact shoe.

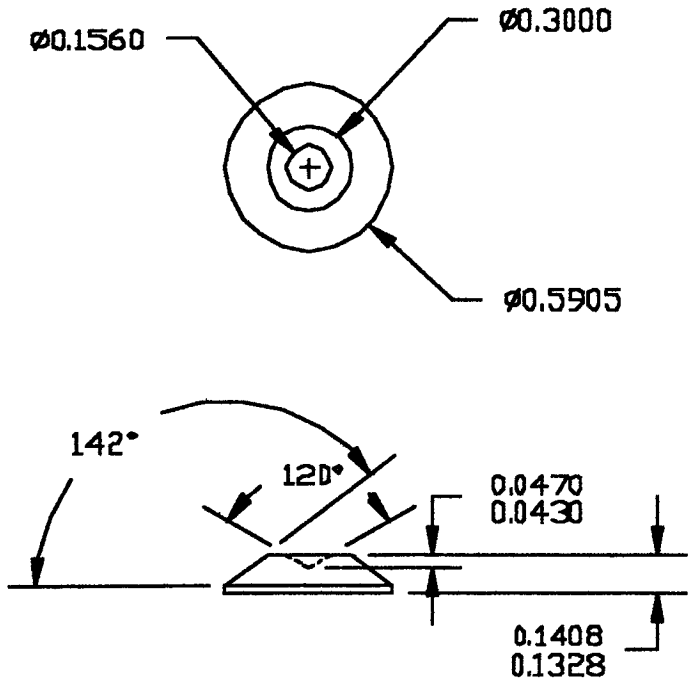

Figure A12. Dimensioned drawing of ball seat.

APPENDIX B: MATLAB SIMULINK FILES OF MOTOR MODEL

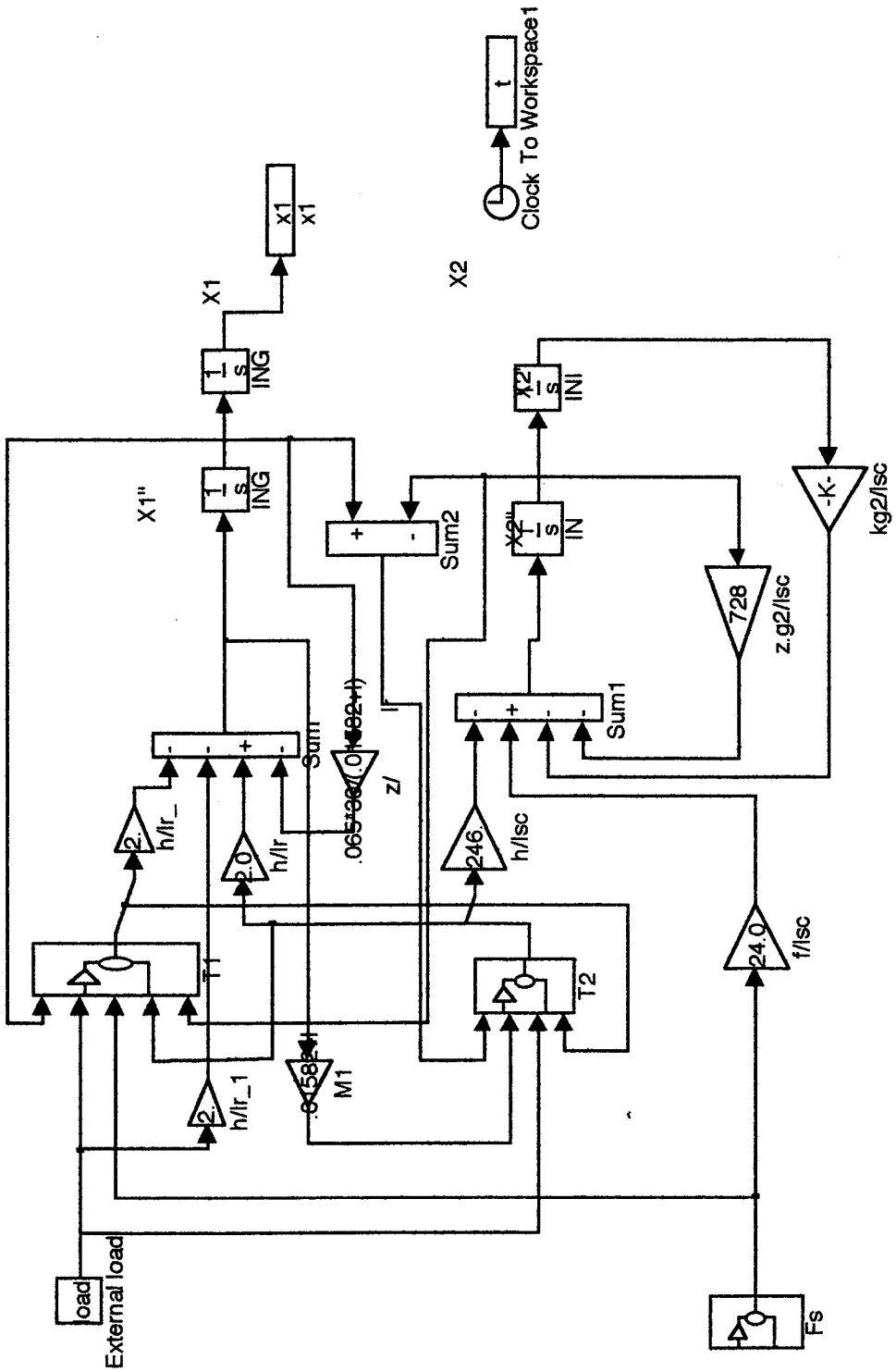

Figure B1. Motor model in Simulink.

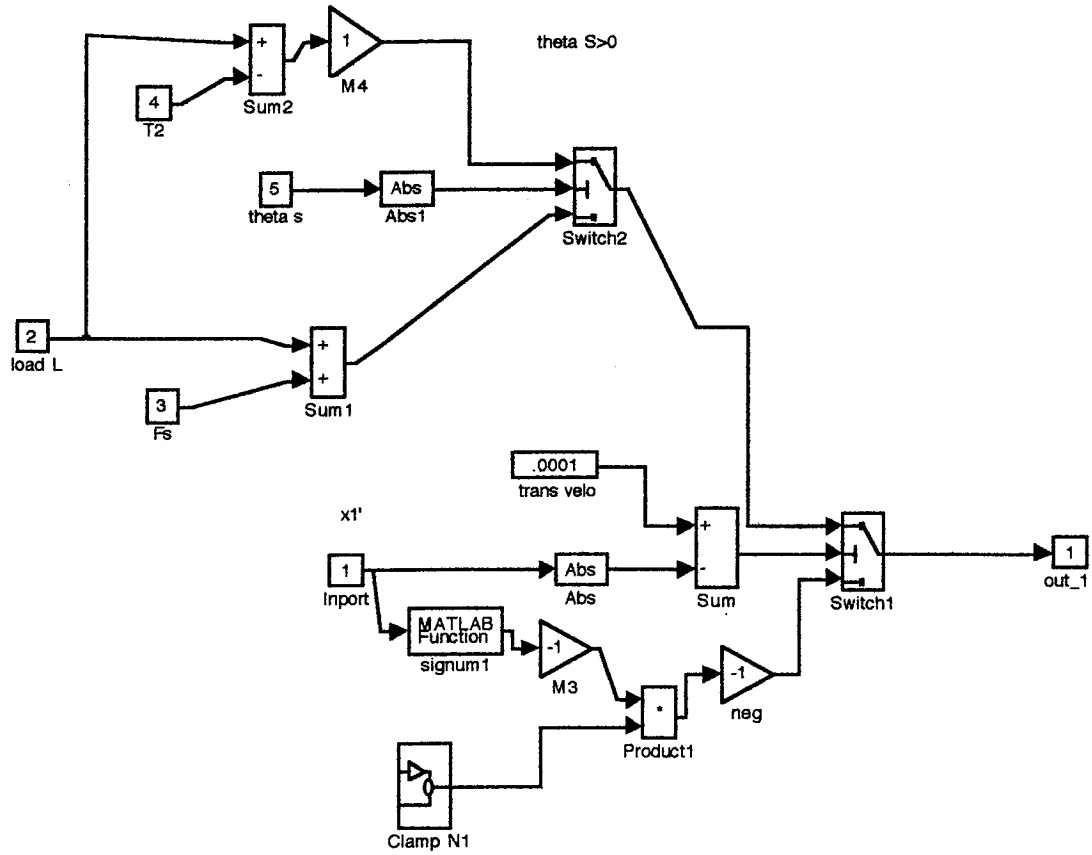

Figure B2. Subsection T1.

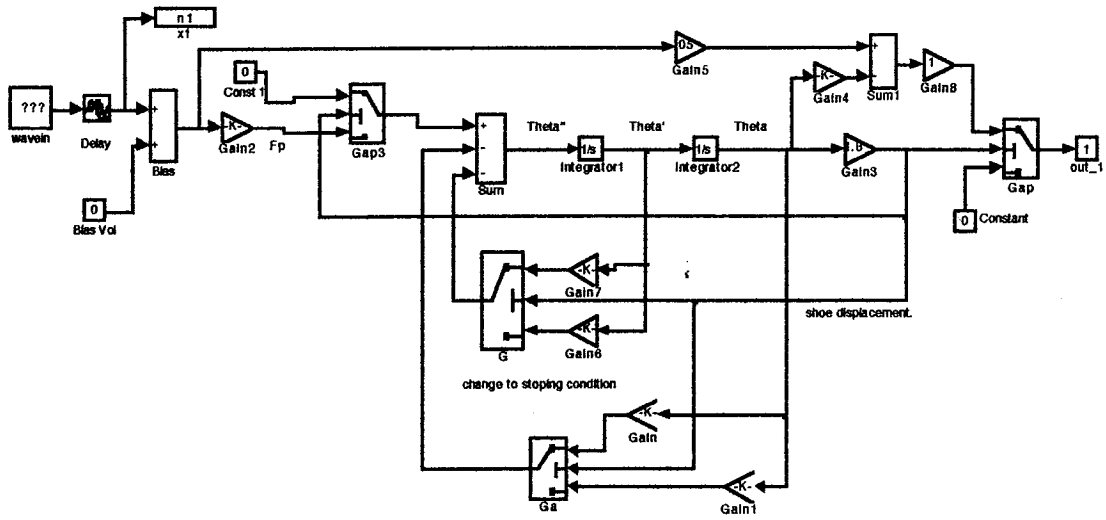

Figure B3. Sub section N1

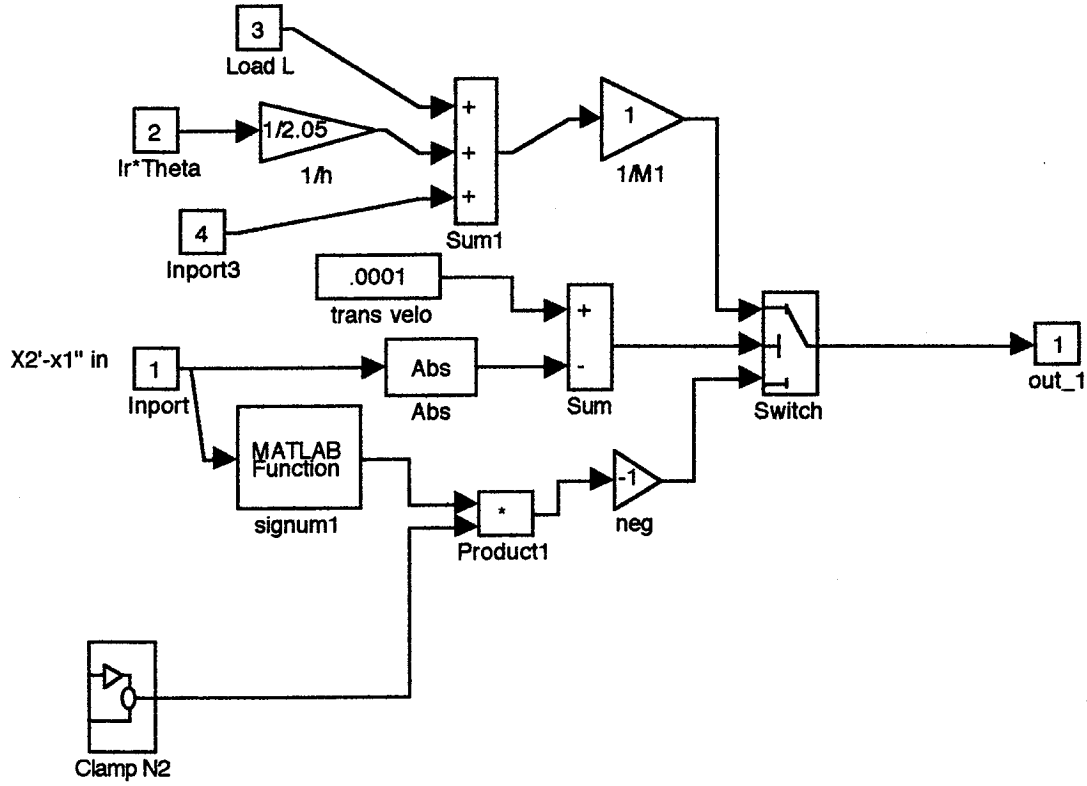

Figure B4. Subsection T2.

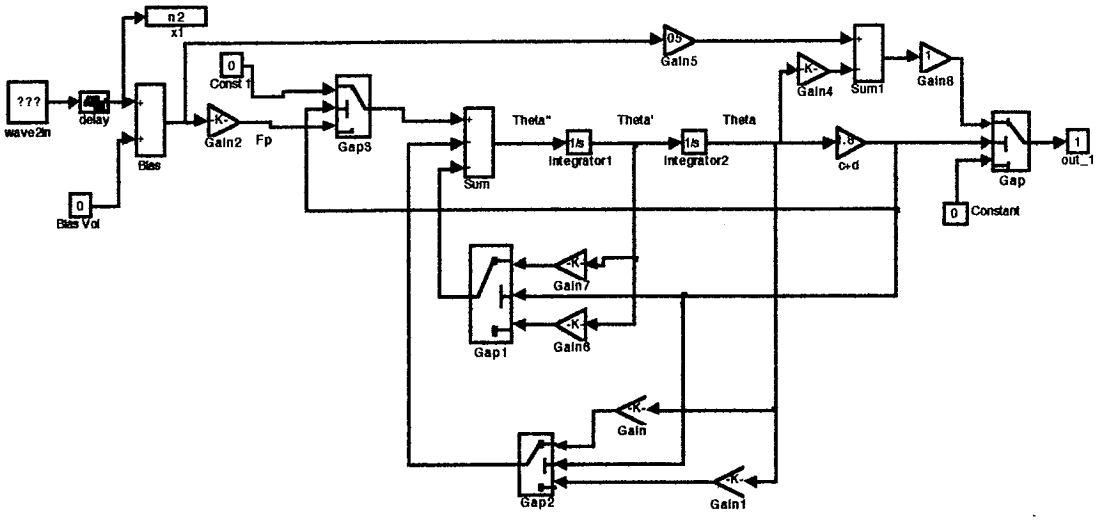

Figure B5. Subsection N2.

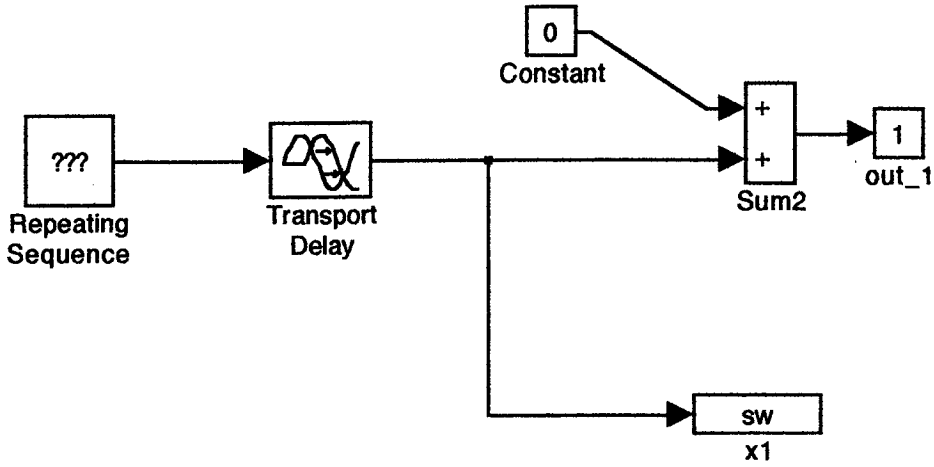

Figure B6. Subsection Fs

BIBLIOGRAPY

1. B. Jaffe, W.R.C. Jr., and H. Jaffe, *Piezoelectric Ceramics*. 1971, Marietta: R. A. N. Publishers.

2. Newton, D. and E. Garcia. *Development of a Linear Piezoelectric Actuator*..in *1994 AIAA/ASME Structural Dynamics $ Materials Conference, Adaptive Structures Forum*. 1994. Hilton Head S.C.

3. Tomikawa, Y., T. Takano, and H. Umeda, *Thin rotary and linear ultrasonic motors using a double-mode piezoelectric vibrator of the first longitudinal and second bending modes*. Japanese Journal of Applied Physics Part 1, 1992. 31(9B): p. 3073-76.

4. Schoner, H.-P., *Piezoelectric motors and their applications*. ETEP, 1992. 2(6): p. 367-371.

5. Cady, W.G., *Piezoelectricity*. 1946, Newyork: McGraw Hill.

6. Kumada, A., *A piezoelectric ultrasonic motor*. Japanese journal of applied physics, 1985. 24: p. 739-741.

7. Sugihara, M., T. Kishi, and R. Inaba. *Quick response in rotation of ultrasonic motor*. in *Proceedings of 10th Symposium on Ultrasonic Electronics*. 1989. Tokyo.

8. Bexell, M., *et al.*, *Characterization of an inchworm prototype motor*. Sensors and Actuators, 1994. 43: p. 322-29.

9. Schaaf, U., *Pushy Motors*. IEE Review, 1995. 41(3): p. 105-108.

10. Hagwood, N. and A. McFarland. *Modelling of a piezoelectric rotary ultrasonic motor*. in *SPIE*. 1994.

11. Zharii, O.Y., *Modeling of a mode conversion ultrasonic motor in the regime of slip*. IEEE Transactions on Ultrasonics, Ferroelectrics, and Frequency Control, 1993. 40(4): p. 411-17.

12. Ueha, S. *Present status of ultrasonic motors*. in *IEEE 1989 Ultrasonics Symposium*. 1989. Montreal.

13. Endo, A. and N. Sasaki, *Linear type ultrasonic motor using two-dimensionally positioned piezoelectric elements*. Ferroelectrics, 1990. 112: p. 165-170.

14. Umeda, M., *et al. Dumbbell-shaped small-sized hybrid ultrasonic motor*. in *Proceedings of 19th Symposium on Ultrasonic Electronics*. 1989. Tokyo.

15. Briot, R., *et al., Generators for piezoelectric motors.* Measurement and Science Technology, 1993. 4: p. 938-46.

16. Tomikawa, Y., *et al. Construction of ultrasonic motors and their application.* in *Proceedings of 8th Symposium on Ultrasonic Electronics.* 1987. Tokyo.

17. Ueha, S. *Present state of the art of ultrasonic motors.* in *Proceedings of 9th Symposium on Ultrasonic Electronics.* 1988. Sendai.

18. Takano, T., *et al., Characteristics and a new control method of a same-phase drive-type ultrasonic motor.* Japanese Journal of Applied Physics, 1991. 30(9B): p. 2277-80.

19. Kamano, T., T. Suzuki, and E. Otoi. *Characteristics and model of ultrasonic motor.* in *8th Symposium on Ultrasonic Electronics.* 1987. Tokyo.

20. Kamano, T., T. Suzuki, and T. Kuzuhara. *Position control system driven by ultrasonic motor.* in *9th Symposium on Ultrasonic Electronics.* 1988. Sendai.

21. Hatsuzawa, T., K. Toyada, and Y. Tanimura, *Speed control characteristics and digital servosystem of a circular traveling wave motor.* Review of Scientific Instruments, 1986. 57(11): p. 2886-90.

22. Aoyagi, M., Y. Tomikawa, and T. Takano, *Ultrasonic motors using longitudinal and bending multimode vibrators with mode coupling by externally additional asymmetry or internal nonlinearity.* Japanese Journal of Applied Physics Part 1, 1992. 31(9B): p. 3077-80.

23. Kurosawa, M., *et al., An ultrasonic motor using bending vibrations of a short cylinder.* IEEE transactions on ultrasonics, ferroelectrics, and frequency control, 1989. 36(5): p. 517-521.

24. Maeno, T., T. Tsukimoto, and A. Miyake, *Finite-element analysis of the rotor/stator contact in a ring-type ultrasonic motor.* IEEE transactions on ultrasonics, ferroelectrics, and frequency control, 1992. 39(9): p. 668-674.

25. Brissaud, M. *Analytical modelling of an ultrasonic motor.* in *Ultrasonic International 93.* 1993. Vienna, Austria.

26. Hagedorn, P. and J. Wallaschek, *Travelling wave ultrasonic motors, part I: working principle and mathematical modelling of the stator.* Journal of Sound and Vibration, 1992. 155(1): p. 31-46.

27. Hirata, H. and S. Ueha. *Revolution speed characteristics of an ultrasonic motor estimated from the pressure distribution of the rotor.* in *Proceedings of 12th Sumposium on Ultrasonic Electronics.* 1991. Tokyo.

28. Hirata, H. and S. Ueha, *Characteristics estimation of a traveling wave type ultrasonic motor.* IEEE Transactions on Ultrasonics, Ferroelectrics, and Frequency Control, 1993. 40(4): p. 402-6.

29. Letty, R.L., *et al., Analysis of an Ultrasonic Piezoelectric Motor using Numerical Modeling.* Journal of material systems and structures, 1993. 4(3): p. 287-434.

30. Suzuki, T., T. Kamano, and T. Kazuhara. *Modeling of progressive wave type ultrasonic motor.* in *Proceedings of 10th Symposium on Ultrasonic Electronics.* 1989. Tokyo.

31. Iijima, T., *et al., Ultrasonic motor using flexural standing wave.* Japanese journal of applied physics, 1987. 26: p. 191-193.

32. Kurosawa, M., H. Yamada, and S. Ueha. *Hybrid transducer type ultrasonic linear motor.* in *9th Symposium on Ultrasonic Electronics.* 1988. Sendai.

33. Kurosawa, M., *et al. Hybrid transducer type ultrasonic linear motor using flexural vibrator.* in *11th Symposium on Ultrasonic Electronics.* 1990. Kyoto.

34. Kurosawa, M. and S. Ueha, *Hybrid transducer type ultrasonic motor.* IEEE transactions on ultrasonics, ferroelectrics, and frequency control, 1991. 38(2): p. 89-92.

35. Ohnishi, O., *et al. Piezoelectric ultrasonic motor using longitudinal-torsional composite vibration of a cylindrical resonator.* in *Proceedings of the IEEE 1989 Ultrasonics Symposium.* 1989. Quebec.

36. Uchino, K., L. Kato, and M. Tohda, *Ultrasonic linear motors using multilayered piezoelectric actuator.* Ferroelectrics, 1988. 87: p. 331-334.

37. Nakamura, K., M. Kurosawa, and S. Ueha, *Characteristics of a hybrid transducer-type ultrasonic motor.* IEEE transactions on ultrasonics, ferroelectrics, and frequency control, 1991. 38(3): p. 188-193.

38. Nakamura, K., M. Kurosawa, and S. Ueha, *Design of a hybrid transducer type ultrasonic motor.* IEEE transactions on ultrasonics, ferroelectrics, and frequency control, 1993. 40(4): p. 395-401.

39. Mori, K., T. Kumagae, and H. Hirai. *Ultrasonic Linear motor for a high precision x-y stage.* in *Ultrasonic Symposium.* 1989. Montreal.

40. Aoyagi, M. and Y. Tomikawa, *Ultrasonic rotary motor using longitudinal and bending multimode vibrator with mode coupling caused by external additional asymmetry.* Japanese Journal of Applied Physics Part 1, 1993. 32(9B): p. 4190-93.

41. Fleischer, M., D. Stein, and H. Meixner, *New type of piezoelectric ultrasonic motor.* IEEE Transactions on Ultrasonics, Ferroelectrics, and Frequency Control, 1989. 36(6): p. 614-19.

42. Fleischer, M., D. Stein, and H. Meixner, *Ultrasonic piezomotor with longitudinally oscillating amplitude-transforming resonator.* IEEE Transactions on Ultrasonics, Ferroelectrics, and Frequency Control, 1989. 36(6): p. 607-613.

43. Fleischer, M., D. Stein, and H. Meixner, *Novel ultrasonic motors with mono- and bimodal drives*. Sensors and Actuators, 1990. A21-A23: p. 357-61.

44. Snitka, V. *Stepping ultrasonic motors for precision positioning*. in *IEEE 1993 Ultrasonics Symposium*. 1993. Baltimore.

45. Takano, T. and Y. Tomikawa. *Linearly moving ultrasonic motor using a multi-mode vibrator*. in *IEEE 1993 Ultrasonics Symposium*. 1988. Baltimore.

46. Kosawada, T., K. Suzuki, and T. Tomikawa, *A card sending linear ultrasonic motor using multi-beam piezoelectric vibrators*. International Journal of Applied Electromagnetics in Materials, 1992. 2: p. 285-290.

47. Iwao, N., M. Yamaguchi, and S. Yamada, *An ultrasonic motor using a shear and bending mode of a disk resonator*. Japanese journal of applied physics, 1990. 29: p. 185-187.

48. Iijima, T., Y. Nakagawa, and h. Ito, *Ultrasonic flat motor using coupling of longitudinal and flexural vibration modes*. Jpn. J. appl. Phys., 1992. 31(8): p. 2598-2605.

49. Tomikawa, Y., *et al. Fundamental considerations of excitation of a flexural progressive wave and its application*. in *Proceedings of 7th Symposium on Ultrasonic Electronics*. 1986. Kyoto.

50. Tomikawa, Y., *et al., Some constructions and characteristics of rod-type piezoelectric ultrasonic motors using longitudinal and torsional vibrations*. IEEE Transactions on Ultrasonics, Ferroelectrics, and Frequency Control, 1992. 39(5): p. 600-607.

51. Tomikawa, Y., *et al. An ultrasonic motor using non-axisymmetric vibration modes of a piezo-ceramic annular plate*. in *Proceedings of 9th Symposium on Ultrasonic Electronics*. 1988. Sendai.

52. Tomikawa, Y., *et al. Ultrasonic motors using longitudinal and torsional modes of a rod vibrator*. in *Proceedings of 10th Symposium on Ultrasonic Electronics*. 1989. Tokyo.

53. Tomikawa, Y., *et al. Excitation of an asymmetric displacement without residual vibration and its application to construct a piezoelectric actuator*. in *Proceedings of 12th Sumposium on Ultrasonic Electronics*. 1991. Tokyo.

54. Micro Pulse Systems, I., . 1986: Santa Barbara, CA 93110.

55. Burleigh, *Piezoelectric electromechanical translation apparatus*, . 1975, Burleigh Instruments, Inc.: United States.

56. Zhang, B. and Z.Q. Zhu. *Design of an inchworm-type linear piezomotor*. in *SPIE*. 1994.

57. Ohnishi, K., *et al.*, *Rotary Inchworm-Type Piezoelectric Actuator*. Electrical Engineering in Japan, 1990. 110(3): p. 107-114.

58. Shimizu, N., *et al.*, *An ultrahigh vacuum scanning tunneling microscope with a new inchworm mechanism*. Journal of Vacuum Science and Technology, 1990. 8(1): p. 333-35.

59. Meisner, J.E. and J.P. Teter. *Piezoelectric/magnetostrictive resonant inchworm motor*. in *SPIE*. 1994.

60. Pandell, T., *design of a piezoelectric caterpillar motor*, in *Department of Mechanical Engineering*. 1996, Vanderbilt University: Nashville. p. 63.

61. Gui, Z., *et al.*, *Investigation on piezoelectric ceramics with high d_{33}, d_{31} for a new type of rotational stepper motor*. IEEE International Symposium on Applications of Ferroelectric, 1995: p. 387-389.

62. Dong, S., *et al.*, *A new type of linear piezolectric stepper motor*. IEEE Transactions on Components, Packaging, and Manufacturing Technology, 1995. 18(2): p. 257-260.

63. Woodburn, C.N., *et al.*, *A one-dimensional piezoelectric-driven inertial micropositioner with vertical capabilities*. Meas. Sci. Technol., 1992. 4: p. 535-537.

64. Howald, L., H. Rudin, and H.-J. Guntherodt, *Piezoelectric inertial stepping motor with spherical rotor*. Review of Scientific Instruments, 1992. 63(8): p. 3909-12.

65. Niedermann, P., R. Ench, and P. Descouts, *Simple piezoelectric translation device*. Review of Scientific Instruments, 1988. 59(2): p. 368-69.

66. Agrait, N., *Vertical inertial piezoelectric translation device for a scanning tunneling microscope*. Review of Scientific Instruments, 1992. 63(1): p. 263-4.

67. Judy, J., D. Polla, and W. Robbins, *A linear piezoelectric stepper motor with submicrometer step size and centimeter travel range*. IEEE Transactions on Ultrasonics, Ferroelectrics, and Frequency Control, 1990. 37(5): p. 428-37.

68. Hayashi, I., *et al.*, *Development of a piezoelectric cycloid motor*. Mechatronics, 1992. 2(5): p. 433-44.

69. Hamaguti, J. *A proposal of a new motor using piezoelectric actuators*. in *Proceedings of the Japan Society of Electrical Engineers*. 1989.

70. King, T.G. and W. Xu, *Piezomotors using flexure hinged displacement amplifier*. Colloquium Digest-IEE, 1995(170): p. 11/1-11/5.

71. Kurosawa, M., M. Takahashi, and T. Higuchi, *Friction drive surface acoustic wave motor*. Ultrasonics, 1996. 34: p. 243-246.

72. Tojo, T., K. Sugihara, and S. Saito, *Piezoelectric-driven turntable with high positioning accuracy (2nd report).* Bulletin of Japanese Society of Precision Engineering, 1990. 24(2): p. 87-93.

73. Tojo, T. and K. Sugihara, *Piezoelectric-driven Turntable with High Positioning Accuracy (1st Report)-Operating Principle and Basic Performance.* japanese Journal of Applied Physics, 1989. 23(1): p. 65-71.

74. Anderson, E.H., D.M. Morroe, and J.L. Fanson, *Development of an active truss element for control of precision structures.* Optical Engineering, 1990. 29(11).

75. Marlow, W.C., *Power dissipation in electromechanical actuator.* Optical Engineering, 1994. 33(9): p. 2936-2941.

76. al., K.U.e., *High precision rotary stage using piezoelectric actuators*, in *Handbook of novel actuators for precise control.* 1994, Fuji Techno Systems: Tokyo. p. 705-719.

77. Brochure, B.M.S., . 1993.

78. Duong, K. and E. Garcia, *Design and performance of a rotary motor driven by piezoelectric stack actuators.* Jpn. J. Appl. Phys., 1996. 35(12A): p. 6334-6341.

79. Goto, H. and T. Sasaoka, *Vertical micro positioning system using PZT actuators.* Bulletin fo the Japan Society of Precision Engineering, 1988. 22(4): p. 277-282.

80. Vanderplaats, G., *Numerical optimization techniques for engineering design.* 1984: McGraw-Hill.

81. Grace, A., *Optimization Toolbox User's Guide.* 1990, Natick, MA: The Mathworks, Inc.

82. Gill, P.E., W. Murray, and M.H. Wright, *Practical Optimization.* 1981, London: Academic Press. 176-180.

83. Powell, M.J.D., *A fast algorithm for nonlineary constrained optimization calculations.* Lecture notes in mathematic, ed. G.A. Watson. Vol. 630. 1978: Springer Varleg.

84. Powell, M.J.D., *The convergence of variable metric methods for nonlinearly constrained optimization calculations.* Nonlinear programming 3, ed. O.L. Mangasarian, R.R. Meyer, and S.M. Robinson. 1978: Academic Press.

85. Han, S.P., *A globally conversion method for nonlinear programming.* Journal of optimization theory and applications, 1977. 22: p. 297.